

Theory of yellow and green excitons in cuprous oxide with emphasis on correction terms and external fields

Von der Fakultät Mathematik und Physik der Universität Stuttgart
zur Erlangung der Würde eines Doktors der Naturwissenschaften
(Dr. rer. nat.) genehmigte Abhandlung

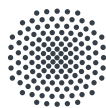
Vorgelegt von

Patric Sebastian Rommel

aus Kirchheim unter Teck

Hauptberichter:	Prof. Dr. Jörg Main
Mitberichterin:	Prof. Dr. Maria Daghofer

Tag der mündlichen Prüfung: 12. Juli 2022



Universität Stuttgart

1. Institut für Theoretische Physik

2022



Inhaltsangabe

Kupferoxydul spielt eine zentrale Rolle in der Geschichte der Exzitonphysik, unter anderem da es der erste Halbleiter ist, in welchem Exzitonen experimentell entdeckt worden sind. Exzitonen, die aus einem Elektron aus seinem niedrigsten Leitungsband und einem Loch aus seinem höchsten Valenzband bestehen, gehören zur gelben Exzitonserie. Vor Kurzem haben optische Absorptionsexperimente diese Serie bis zu einer Hauptquantenzahl von $n = 25$ verfolgt [T. Kazimierczuk *et al.*, *Nature* **514**, 343 (2014)]. Das eröffnet die Möglichkeit neuartiger Anwendungen, welche die speziellen Eigenschaften hoch angeregter Rydbergssysteme ausnutzen, zum Beispiel im Bereich der Quanteninformatonsverarbeitung. Für deren Umsetzung ist ein gründliches Verständnis der Eigenschaften von Exzitonen notwendig. In dieser Doktorarbeit streben wir an, das theoretische Wissen um die gelbe und grüne Serie in Kupferoxydul voranzubringen. Wir verwenden numerische Simulation und analytische Methoden zur detaillierten Untersuchung der Austauschwechselwirkung der S Zustände, der Feinstrukturaufspaltung der D Zustände, von Spektren in äußeren magnetischen Feldern in Faraday und Voigt Konfiguration, von Frequenzverdopplung in verbotenen Richtungen, und der Autoionisationsspektren in äußeren elektrischen und parallelen elektrischen und magnetischen Feldern. Für Letzteres wenden wir die Methode der komplexen Koordinatenrotation an, welche wir weiterhin dazu benutzen, um die grünen Exzitonresonanzen im gelben Kontinuum zu berechnen. Wir präsentieren Absorptionsspektren für Übergänge aus dem Grundzustand des Kristalls und für Interserienübergänge aus der gelben in die grüne Serie.



Abstract

Cuprous oxide has played a central role in the history of exciton physics, being the semiconductor where excitons were first experimentally discovered. Excitons formed from an electron in its lowest conduction band and a hole from its the highest valence band belong to the yellow exciton series. Recently, optical absorption experiments have followed this series up to principal quantum number $n = 25$ [T. Kazimierczuk *et al.*, Nature **514**, 343 (2014)]. This opens up possibilities for novel applications using the particular attributes of highly excited Rydberg system, for example in quantum information processing. For this, the properties of the excitons have to be understood thoroughly. In this thesis, we aim to advance the theoretical knowledge of the yellow and green exciton series in cuprous oxide. We use numerical simulation and analytical methods to investigate in detail the exchange splitting of the S states, the fine structure splitting of the D excitons, spectra in external magnetic fields in Faraday and Voigt configuration, second harmonic generation in forbidden directions, and autoionizing spectra in external electric and parallel magnetic and electric fields. For the latter, we apply the complex-coordinate-rotation method, which we then further use to calculate the green exciton resonances lying in the yellow continuum. We present absorption spectra for transitions from the crystal ground state and for interseries transitions from the yellow to the green series.



Contents

Inhaltsangabe	3
Abstract	5
1. Introduction	13
2. Theoretical background	17
2.1. Cuprous oxide and the octahedral group	17
2.2. Hamiltonian including the complex valence band structure	21
2.3. Central-cell corrections	23
2.3.1. Corrections to the dielectric constant	23
2.3.2. Exchange interaction	24
2.4. Application of external electric and magnetic fields	25
2.5. Center-of-mass transformation	25
2.6. Resonances and complex energies	26
2.7. Complex-coordinate-rotation method	28
2.8. Numerical diagonalization	29
2.8.1. Generalized eigenvalue problem	29
2.8.2. Oscillator strengths	31
3. The exchange interaction in the yellow series	33
3.1. The exchange interaction	34
3.2. Source of experimental data	36
3.3. Reversal of yellow 2S ortho- and paraexcitons	38
3.4. Dependence of the exchange splitting on the principal quantum number .	40
3.5. Splitting of yellow 1S state vs green 1S state	42

4. Analysis of the fine structure of the D-exciton shell	45
4.1. Experimentally observed structure of the n -multiplets	46
4.2. Separating the Hamiltonian according to symmetry	47
4.3. Coupling to the green series	50
4.4. Extension to principal quantum number $n \geq 6$	52
5. Magneto-Stark effect of yellow excitons	55
5.1. Faraday and Voigt configuration, magneto-Stark effect	56
5.2. Source of experimental data	57
5.3. Comparison of experimental and numerical data	58
5.3.1. Influence of the magneto-Stark effect	62
6. Second harmonic generation in magnetic fields	65
6.1. Second Harmonic Generation	67
6.1.1. Calculation of SHG intensities	68
6.1.2. Dipole emission process	69
6.1.3. Linewidths	70
6.1.4. Relative strength of dipole and quadrupole emission processes	71
6.2. Discussion of selection rules	73
6.2.1. Quadrupole and electric-field induced dipole emission	74
6.2.2. Separating magneto-Stark effect and Zeeman effect in forbidden directions	75
6.2.3. Symmetry reduction by the magnetic field	76
6.2.4. Additional consideration of the Γ_4^- states	78
6.3. Source of experimental data	80
6.4. Presentation of spectra	80
7. Rydberg excitons in electric and magnetic fields	83
7.1. Application of an external electric field	84
7.2. Discussion of spectra	85
7.2.1. Electric fields in [001] direction	85
7.2.2. Parallel electric and magnetic fields	87
8. The green exciton series in cuprous oxide	91
8.1. The green excitons	92
8.2. The spectrum of odd-parity green excitons	95
8.3. The spectrum of even-parity green excitons	98
8.3.1. Classification of the even parity states of the green series	99
8.3.2. Two-photon absorption spectra of green excitons	100
8.3.3. Exchange splitting of the even exciton states	103

9. Interseries dipole transitions from yellow to green excitons	105
9.1. Dipole transitions between excitonic states	107
9.1.1. Operator identity between kinetic momentum and derivatives of the band Hamiltonian	107
9.1.2. Numerical evaluation of the matrix elements $\langle \Pi' \pi_z \Pi \rangle$	111
9.2. Non-Hermitian generalized eigenvalue problem	112
9.3. Numerically calculated interseries transition strengths	113
9.3.1. Interseries absorption spectra	113
9.3.2. Phonon-induced linewidths	114
9.3.3. Dipole transitions from odd-parity yellow exciton states to even- parity green states	114
9.3.4. Dipole transitions from even-parity yellow states to odd-parity green states	118
 10. Conclusion	 121
A. Material constants	127
B. Assignment of quantum numbers for the green series	129
 Bibliography	 135
Zusammenfassung in deutscher Sprache	149
Curriculum Vitae	155
Danksagung	159



List of abbreviations

c	conduction band
c.p.	cyclic permutation
CCC	central-cell corrections
cf.	compare
cont	continuum
D	dipole
e	electron
e.g.	for example
eff	effective
et al.	and others
exc	exciton
exch	exchange (interaction)
exp	experimental
Fig.	figure
g	green (exciton series), also: gap
H	Haken
h	hole

List of abbreviations

Hyd	hydrogen
i.e.	that is
LO	longitudinal optical
MSE	magneto-Stark effect
OPA	one-photon absorption
PB	Pollmann-Büttner
ph	photon
phn	phonon
Q	quadrupole
Ref.	reference
rel	relative
Sec.	section
SHG	second harmonic generation
so	spin-orbit
t	total
TP	two-photon
uc	unit cell
v, vb	valence band
viz.	namely
y	yellow (exciton series)

1

Introduction

When an electron in a semiconductor or insulator is lifted from a valence band into a conduction band, a positively charged hole is left behind. The negatively charged electron and the hole can then interact via the Coulomb force, forming a composite quasiparticle called an exciton. This conception of an excitation in condensed matter systems involving an electron-hole pair was first developed in the 1930s [1–5]. Twenty years later, excitons were experimentally discovered by Hayashi [6, 7] and by Gross [8, 9].

One differentiates between Frenkel and Wannier-Mott excitons [10, 11]. The former are characterized by large binding energies of the order of 1 eV and small distances between electron and hole, leading in effect to a localized excitation at a given lattice point. Wannier excitons on the other hand are more weakly bound with binding energies up to three orders of magnitude smaller than in Frenkel excitons, resulting in a much more delocalized system covering many unit cells of the solid. They can therefore typically be modeled quite well as a hydrogenlike system with modified material parameters. The research field of excitons covers a wide range of subjects, ranging from biexcitons [12–16], trions [17], polyexcitons [18], bound exciton complexes [19] over polariton lasers [20–23] and excitons in reduced dimensionality [24] to possible realizations of Bose-Einstein condensates [25–29]. In this thesis, we will treat Wannier excitons, more specifically excitons in the semiconductor cuprous oxide.

In 2014, Kazimierczuk *et al.* performed a seminal study of the yellow exciton series in cuprous oxide, observing absorption lines with principal quantum numbers up to $n = 25$ [30], and creating the basis for a large number of further experimental and theoretical inquiries [31–40]. This was a major stepping stone for the field of excitonic Rydberg systems.

Hydrogenlike systems with high principal quantum numbers like Rydberg atoms and Rydberg excitons are of great experimental and theoretical interest. Due to typical scaling laws in Rydberg systems, Rydberg atoms have a large dipole moment, giving them great sensitivity to external fields [41]. Recently, a lot of research has been done seeking to exploit their special properties [42], for example for usage in quantum information

processing applications. Their strong mutual interactions open up many possibilities for the implementation of quantum logical gates [43–46]. A central feature of many proposals is the so called Rydberg blockade effect, which prevents the excitation of multiple Rydberg atoms, if they are too close to each other. In Ref. [30], signs for a Rydberg blockade in the yellow excitons were found, and the possibility of an excitonic Rydberg blockade lead to proposals for the enhancement of optical nonlinearities [47, 48] and construction of single-photon sources [49, 50]. In general, Rydberg excitons prove to be a promising research field for applications known from atomic Rydberg systems.

Cuprous oxide is the material where excitons were first experimentally observed, and generally has a central role in excitonic research. Its large binding energy of about 86 meV [34] leads to well-separated lines for different principal quantum numbers, aiding in the observation of detailed features of the spectrum.

In the 1950s and 60s, experimental work by Nikitine [51, 52], Gross [9, 53, 54], Ueta [55], and McLean [56] helped to refine the Wannier model [57, 58]. More and more corrections to the description [11, 24, 59, 60] were developed over time.

The Wannier description typically assumes a band structure with a single conduction band and a single valence band. In cuprous oxide, the uppermost valence bands are degenerate, necessitating an approach going beyond this condition. The appropriate framework was devised by Luttinger and Kohn [61], leading to the Suzuki-Hensel Hamiltonian [62], which was first developed for Germanium. In this thesis, we will use a model of excitons in cuprous oxide which is based on the application of this framework to cuprous oxide.

In Chapter 2, we begin by laying out the theoretical framework describing the yellow and green exciton series in cuprous oxide. We will use the Suzuki-Hensel Hamiltonian for modeling the valence band structure. We then give an overview of the central-cell corrections, which are additional terms that become important for small electron-hole distances. They mainly affect the even parity states, like the S and D excitons. We discuss how external fields can be added to the description. Since an electric field can lead to autoionization, we then present the method of complex-coordinate rotation for the modeling of resonances with finite lifetimes. Afterwards, we outline our approach of numerical diagonalization of the Hamiltonian, and how energies and spectra can be obtained from it.

The exchange interaction forms a part of the central-cell corrections. It leads to a characteristic splitting between spin-singlet and spin-triplet S states. A straightforward application of this to the yellow exciton series would lead to the expectation that the optically accessible ortho-excitons are lifted to higher energies than the spin-flip forbidden para-excitons, also called dark excitons. Recently, experimental investigations into the dark exciton series confirmed that this expectation is contradicted for the case of the yellow 2S exciton [63], a result predicted by earlier numerical calculations [38]. In Chapter 3, we investigate this effect in detail. We show how the coupling to the green exciton series is responsible for the reversed positions of the 2S ortho-para pair. By varying the strength of the spin-orbit coupling in our numerical calculation, we reveal an avoided

crossing between the 2S yellow orthoexciton and one of the green 1S excitons, showing that the influence of the green exciton series is responsible for the reversed positions of the 2S ortho-para pair. We additionally present results on the scaling behavior of the exchange splitting as a function of the principal quantum number and investigate the difference in size of the splitting in the yellow and green 1S states.

The exchange interaction plays an important part in the understanding of the fine structure observed in the yellow exciton series. It affects all states with a nonvanishing wave function at zero electron-hole separation. Since the cubic symmetry of the crystal leads to a mixing of angular momenta with the same parity, the exchange interaction causes a splitting not only of the S states, but also of the D states. In fact, an especially strong splitting is experimentally observed for a certain D exciton with symmetry Γ_5^+ , lifting it to the highest energy in a given multiplet with the same principal quantum number. The calculations in Ref. [38] point to the influence of the mixing with the green 1S state as a possible explanation. In Chapter 4, we take a close look at the fine structure of the D excitons of the yellow exciton series in cuprous oxide. We compare numerical and experimental data, allowing us to improve upon previous assignments of quantum numbers. Our study shows that the level-repulsion effect from the green 1S state plays a crucial role in causing the observed level structure.

The difference between the exciton and an atomic system manifests itself not only in the fine structure splitting in the field free case, but also in the interaction with external magnetic fields. We distinguish between two experimental configurations: the Faraday geometry, where the magnetic field is applied in parallel to the exciting laser, and the Voigt geometry, where it is applied orthogonally. In Chapter 5 we present experimental and numerical data showing that the spectra of magnetoexcitons differ depending on the configuration. We mainly attribute this to the appearance of an additional effective electric field due to the magneto-Stark effect in the Voigt geometry. This constitutes a significant difference to atomic spectra, where the magneto-Stark effect is suppressed due to the much larger total mass.

Second harmonic generation (SHG) is a process where two incoming photons are coherently combined to one outgoing photon with the doubled energy. This process was recently experimentally probed for the yellow series in cuprous oxide [64]. The associated selection rules in systems with cubic symmetry forbid SHG processes along certain axes of the crystal. Application of external fields can reduce the symmetry, breaking these selection rules. In Chapter 6, we present simulated SHG spectra in forbidden directions, comparing numerical data with experimental results and exploring the mechanisms by which the selection rules are lifted.

F. Schweiner *et al.* presented a complete theoretical description of the yellow excitons in cuprous oxide subjected to an external magnetic field [65]. In Chapter 7, we present results which extend this description by the additional application of an external electric field. The investigated electric fields are significantly larger than the effective electric field due to the magneto-Stark effect in the previous chapters, and we thus enter the regime where autoionization takes place. The description of the excitons as bound states thus

becomes inadequate, and we instead need to conceptualize them as quasibound resonance states with finite lifetime. To properly treat them, we augment our numerical method by the complex-coordinate-rotation method. We investigate the effect of different field strengths on the complex energies and oscillator strengths of the autoionizing resonances.

Most studies of bulk excitons in cuprous oxide focus on the yellow excitons, which form when an electron is lifted from the uppermost valence band to the lowest conduction band. If an electron is instead lifted from the second-highest valence bands, a green exciton is created. Most green exciton states lie energetically within the continuum of the yellow series. Since the band structure terms of the Hamiltonian lead to a coupling of the yellow and green lines, the latter are thus quasibound resonances with a finite lifetime. For their study in Chapter 8, we therefore also use the complex-coordinate-rotation method. We present absorption spectra and explore scaling laws of the binding energy, linewidth, etc. as a function of the principal quantum number.

Recently, Krüger *et al.* investigated interseries transitions between the yellow and green exciton series in a hydrogenlike model [66]. In Chapter 9, we extend these calculations by the inclusion of the complex valence band structure. We present dipole interseries transition spectra for different polarization combinations of the pump and probe laser. To this end, we use the results on the green excitons obtained in Chapter 8 and modify the calculation scheme of absorption spectra of transitions starting from the crystal ground state used in the previous chapters, to now handle the case of interseries transitions instead.

We finally conclude with a summary and outlook in Chapter 10.

2

Theoretical background

In this chapter, we outline the general theory of excitons in cuprous oxide, which will provide the foundation of the investigations presented afterwards. We begin with a short introduction of the semiconductor cuprous oxide. We then present our model Hamiltonian for the description of the yellow and green exciton series. We discuss the transformation to center-of-mass coordinates, the application of external fields, and the use of the complex-coordinate-rotation method for the calculation of resonances. We finish by stating our method of numerical diagonalization and calculation of spectra.

2.1

Cuprous oxide and the octahedral group

Cuprous oxide or copper(I) oxide is a red-coloured crystal material with chemical formula Cu_2O . We show a picture of a natural crystal and a cut slab in Fig. 2.1 on the left. The copper and oxygen cores are arranged in a cubical lattice structure as depicted in Fig. 2.1 on the right. It is a direct semiconductor with a band structure at the Γ -point as presented on the left-hand side of Fig. 2.2. If an external excitation lifts an electron from one of the valence bands across the band gap $E_g \approx 2.17\text{ eV}$ into one of the conduction bands, the resulting electron-hole pair interacts via the Coulomb interaction and forms a bound or quasibound system called an exciton. In the simplest cases, these quasiparticles are well-described by a hydrogenlike model.

The properties of the excitons differ depending on the involved bands, leading to different exciton series as marked in Fig. 2.2. Most research focuses on the yellow series with the electron in the lowest Γ_6^+ conduction band and the hole in the highest Γ_7^+ valence band. Due to the material parameters of cuprous oxide, especially the effective masses of electron m_e and hole m_h and the dielectric constant ε (see Table A.1), the

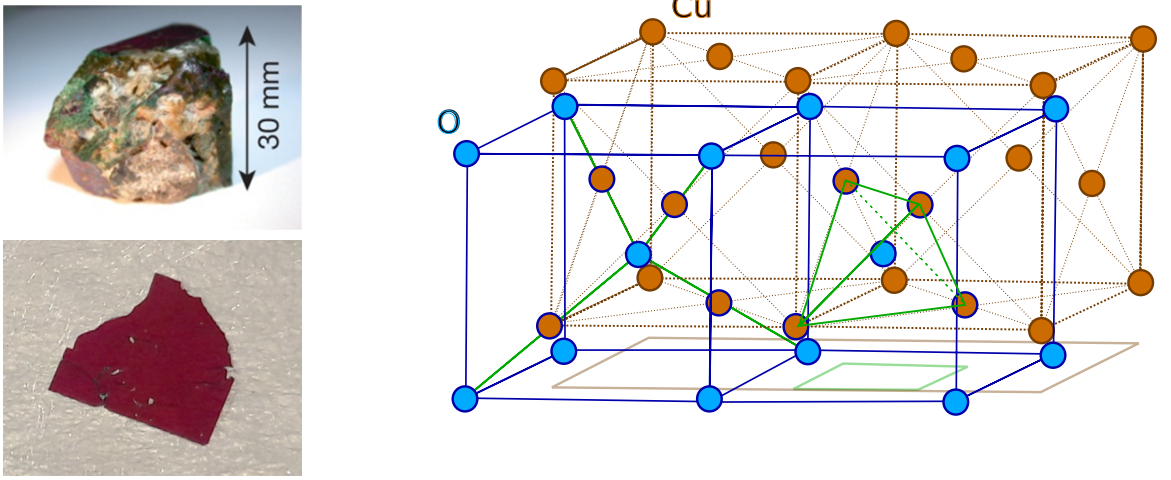


Figure 2.1.: *Top left*: Natural Cu_2O crystal. Adapted from [30]. *Bottom left*: Cu_2O crystal slab. Adapted from [67]. *Right*: Crystal lattice structure of cuprous oxide, made up of a face-centered cubic lattice of copper cores and a body-centered cubic lattice of oxygen cores, with a lattice constant given by $a_g \approx 0.43 \text{ nm}$ [68]. Taken from [69].

exciton Rydberg energy of the yellow series is approximately $E_{\text{Ryd}} \approx 90 \text{ meV}$ [30], leading to an easily observable Rydberg series in absorption spectra even up to high principal quantum numbers. Corrections to the hydrogenlike description manifest themselves as an additional fine-structure splitting [33].

When the electron is in the same Γ_6^+ conduction band, but the hole is instead in the second uppermost Γ_8^+ valence bands, the exciton belongs to the green series. The yellow and green series are separated by the spin-orbit splitting $\Delta \approx 130 \text{ meV}$ and the spectral lines associated with them are thus energetically arranged as shown in Fig. 2.2 on the right.

In this thesis, we will focus mostly on the yellow excitons in Chapters 3 - 7. But even there, the interaction between the two series will play an important role. We show results concerning the green series specifically in Chapter 8 and 9. As suggested by Fig. 2.2, additional series like the blue and violet series exist, but they are not further discussed in this work.

The crystal environment leads to several effects playing a role in exciton physics, for example by modifying the dielectric constant and the effective masses. Scattering processes, most prominently with phonons, lead to a broadening of lines beyond those given by radiative decay [70–74]. Another important effect is the reduction of the symmetry to the crystal point group. The hydrogen atom has the symmetry $O(4)$ with the conservation of the Runge-Lenz vector, leading to the degeneracy of all levels with the

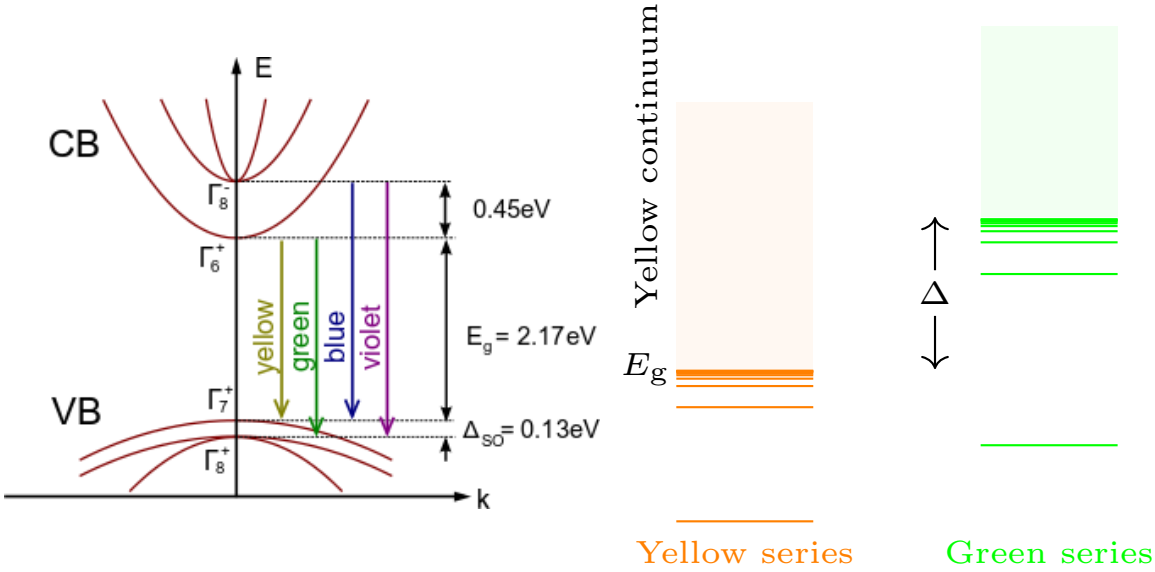


Figure 2.2.: *Left*: Band structure of cuprous oxide near the band gap. The lowest Γ_6^+ conduction band is formed from Cu 4S orbitals, the highest Γ_7^+ and Γ_8^+ valence bands from Cu 3D orbitals [30]. Figure taken from Ref. [30]. *Right*: Schematic of the energetic placement of yellow and green exciton states. The two series are split by the energy Δ . Most of the green lines lie inside the yellow continuum, except for the 1S states. They are thus quasibound resonances, as we will discuss in Chapter 8.

same principal quantum number n . Corrections invariant under rotations will generally reduce the symmetry group to $O(3)$, splitting the n -multiplets into levels with the same angular momentum. In a group theoretical context, these degenerate levels can be understood as invariant subspaces of the symmetry group operations. For example, states with vanishing angular momentum, i.e., S states, remain completely invariant under rotations, whereas P states transform like the functions x , y , and z . This classification into invariant subspaces with different transformation behaviors is the classification of states according to the *irreducible representations* of the symmetry group. For the rotational group $O(3)$, the division of states into irreducible representations is simply given by the assignment of the angular momentum quantum number L [75]. In our notation, D_L^\pm is the representation belonging to angular momentum L , where + or - additionally gives the behavior under the parity operation. For the consideration of spins and half-integer angular momenta, the symmetry group has to be extended to the special unitary group $SU(2)$.

In cuprous oxide, the point group is the octahedral group O_h [30]. For the exciton states, the total angular momentum \mathbf{F}_t is thus not conserved and the \mathbf{F}_t -multiplets split. The splitting pattern is given by the reduction of the irreducible representations

2. Theoretical background

of the full rotation group to those of O_h . This reduction is presented in Table 2.1. The irreducible representations are denoted by Γ_i^\pm ; more details on their properties can be found in Ref. [76]. With the information given in the table, we can for example deduce that multiplets with total angular momentum $F_t = 1$ remain degenerate, whereas multiplets with total angular momentum $F_t = 2$ will in general split into two levels, one with irreducible representation Γ_3^\pm and one with Γ_5^\pm . This kind of symmetry-associated splitting is the reason for the fine-structure splitting of the F states observed in Ref. [33]. This kind of analysis using group theoretical methods [77] will play a central role in our investigation of exciton systems in the crystal environment with reduced symmetry.

One thing to keep in mind in the context of the level splitting and mixing due to the crystal environment is the fact that in cuprous oxide, the parity remains a good quantum number. Basic properties of exciton states can often be tied directly or indirectly to the parity. For example, only odd-parity states can be excited in one-photon dipole experiments, while quadrupole and two-photon absorption only affects the even-parity states. Still, the more nuanced understanding using the irreducible representations gives valuable additional information. To illustrate, not all odd-parity states are dipole-allowed, but only those of symmetry Γ_4^- .

Building a Hamiltonian for the description of the spectrum which includes these details requires going beyond a simple hydrogenlike model. The situation of electron and hole in the semiconductor lattice structure has to be properly taken account for. In the next section, we introduce the Hamiltonian used in the rest of the thesis, which fulfills this condition. We will see that the reduced cubic symmetry is introduced into the model by the complex valence band structure via the kinetic energy of the hole.

Table 2.1.: Reduction of the irreducible representations of the spherical group to the irreducible representations of the octahedral group [76].

integer angular momentum		half-integer angular momentum	
D_0^\pm	Γ_1^\pm	$D_{1/2}^\pm$	Γ_6^\pm
D_1^\pm	Γ_4^\pm	$D_{3/2}^\pm$	Γ_8^\pm
D_2^\pm	$\Gamma_3^\pm + \Gamma_5^\pm$	$D_{5/2}^\pm$	$\Gamma_7^\pm + \Gamma_8^\pm$
D_3^\pm	$\Gamma_2^\pm + \Gamma_4^\pm + \Gamma_5^\pm$	$D_{7/2}^\pm$	$\Gamma_6^\pm + \Gamma_7^\pm + \Gamma_8^\pm$
D_4^\pm	$\Gamma_1^\pm + \Gamma_3^\pm + \Gamma_4^\pm + \Gamma_5^\pm$	$D_{9/2}^\pm$	$\Gamma_6^\pm + 2\Gamma_8^\pm$
D_5^\pm	$\Gamma_3^\pm + 2\Gamma_4^\pm + \Gamma_5^\pm$	$D_{11/2}^\pm$	$\Gamma_6^\pm + \Gamma_7^\pm + 2\Gamma_8^\pm$
D_6^\pm	$\Gamma_1^\pm + \Gamma_2^\pm + \Gamma_3^\pm + \Gamma_4^\pm + 2\Gamma_5^\pm$	$D_{13/2}^\pm$	$\Gamma_6^\pm + 2\Gamma_7^\pm + 2\Gamma_8^\pm$

2.2 Hamiltonian including the complex valence band structure

We are working in the general framework in which excitons are described as hydrogenlike excitations of the crystal, where an electron is lifted from one of the valence bands to the conduction band, leaving behind a hole. To properly treat the effects of the cubically-symmetric band structure, we need to find an appropriate Hamiltonian description for the kinetic energies of the electron and hole in the warped bands.

The irreducible representations marking the bands in Fig. 2.2 denote the transformation behavior of the electron Bloch functions at the Γ point when the spin is included. For the lowest conduction band, the given representation is Γ_6^+ . This result from the combination of the transformation behavior of the 4S orbital, Γ_1^+ , and of the electron spin, Γ_6^+ [76]. Due to the spin degree of freedom, the conduction band is twofold degenerate.

The situation is more complicated for the highest valence bands. Here, the 3D orbitals split into Γ_3^+ and Γ_5^+ (see Table 2.1). The latter is then split by the spin-orbit coupling into the uppermost Γ_7^+ valence band and the Γ_8^+ band below it [34]. The Bloch functions in coordinate space belonging to these bands transform like the functions yz , zx and xy of Γ_5^+ . Let ψ_{yz} , ψ_{xz} and ψ_{xy} denote the corresponding Bloch functions. We first form the linear combinations

$$\psi_{+1} = -(\psi_{yz} + i\psi_{xz})/\sqrt{2}, \quad \psi_0 = \psi_{xy}, \quad \psi_{-1} = (\psi_{yz} - i\psi_{xz})/\sqrt{2}. \quad (2.1)$$

In the three-dimensional Hilbert space spanned by these three functions, we introduce an operator I_z such that the $I_z\psi_i = i\psi_i$ for $i = +1, 0, -1$, i.e. an operator whose eigenvalues are just the assigned labels. These eigenvalues are in many ways analogous to the eigenvalues of the z -component of an angular momentum of unity. We can complete the set by constructing operators I_x and I_y to form the *quasispin* vector \mathbf{I} . This quasispin effectively acts like an additional spin degree of freedom, keeping in mind that the eigenfunctions belong to Γ_5^+ and not Γ_4^+ . On top of this, the hole also has the usual hole spin \mathbf{S}_h . Combined this leads to a sixfold degeneracy, which is in turn lifted by the spin-orbit coupling, resulting in the twofold degenerate Γ_7^+ and the fourfold degenerate Γ_8^+ bands as depicted in Fig. 2.2.

In cuprous oxide, the Γ_6^+ conduction band is very well approximated by a parabola. Because of this, the electron kinetic energy is only altered by the introduction of a modified effective electron mass m_e . The kinetic energy of the hole, on the other hand, receives nontrivial corrections. The proper framework for the treatment of degenerate valence bands as discussed here was developed by Luttinger and Kohn [61]. They used a perturbation theoretical approach for removing the interband coupling terms from the description of the kinetic energy. This results in an effective Hamiltonian living only in

the low-dimensional space of the bands of interest. The mixing with the other bands is included by a renormalization of the coupling terms between the studied bands. Taking into account the symmetry of the crystal, the relatively simple Suzuki-Hensel Hamilton operator [62] remains, with only a small number of free parameters. These are called the *Luttinger parameters*. For cuprous oxide, they can be determined by fitting the Suzuki-Hensel Hamiltonian to spin-DFT calculations [34, 78]. The model for the kinetic energy of the hole used in this thesis is this Suzuki-Hensel Hamiltonian with the fitted parameters.

In the following sections, we introduce the basic theoretical description on which the rest of the thesis is based. We begin by presenting the Hamiltonian for excitons in cuprous oxide, which gives the band structure corrections to the simple hydrogenlike description. In addition, central-cell corrections are required for a detailed analysis of the even parity states and especially the ortho and para S states. Further details of derivations can be found in the literature [11, 35, 38, 60, 69, 79, 80].

The yellow and green exciton series in cuprous oxide belong to the Γ_7^+ and Γ_8^+ valence band, respectively. A unified description of both series can be obtained by using the Hamiltonian [35]

$$H = E_g + H_e(\mathbf{p}_e) + H_h(\mathbf{p}_h) + V(\mathbf{r}_e - \mathbf{r}_h) + V_{\text{CCC}}(\mathbf{r}) . \quad (2.2)$$

Here E_g is the band gap between the uppermost Γ_7^+ valence band and the lowermost Γ_6^+ conduction band. The kinetic energies of electron and hole are given by

$$\begin{aligned} H_e(\mathbf{p}_e) &= \frac{\mathbf{p}_e^2}{2m_e} , \quad (2.3) \\ H_h(\mathbf{p}_h) &= H_{\text{SO}} + \frac{1}{2\hbar^2 m_0} \{ \hbar^2(\gamma_1 + 4\gamma_2)\mathbf{p}_h^2 + 2(\eta_1 + 2\eta_2)\mathbf{p}_h^2(\mathbf{I} \cdot \mathbf{S}_h) \\ &\quad - 6\gamma_2(p_{h1}^2 \mathbf{I}_1^2 + \text{c.p.}) - 12\eta_2(p_{h1}^2 \mathbf{I}_1 \mathbf{S}_{h1} + \text{c.p.}) - 12\gamma_3(\{p_{h1}, p_{h2}\}\{\mathbf{I}_1, \mathbf{I}_2\} + \text{c.p.}) \\ &\quad - 12\eta_3(\{p_{h1}, p_{h2}\}(\mathbf{I}_1 \mathbf{S}_{h2} + \mathbf{I}_2 \mathbf{S}_{h1}) + \text{c.p.}) \} . \quad (2.4) \end{aligned}$$

We use the electron mass in the crystal m_e and in vacuum m_0 , the Luttinger parameters γ_i , η_i , the spin \mathbf{S}_h and quasispin \mathbf{I}_i of the hole, and the momenta \mathbf{p}_e and \mathbf{p}_h of the electron and hole, respectively. The indices $i = 1, 2, 3$ for the momenta, positions, quasispin and hole spin denote the Cartesian x , y , and z -components, “c.p.” denotes cyclic permutation. The spin-orbit coupling term reads

$$H_{\text{SO}} = \frac{2}{3}\Delta \left(1 + \frac{1}{\hbar^2} \mathbf{I} \cdot \mathbf{S}_h \right) . \quad (2.5)$$

It is diagonal in the effective hole spin $\mathbf{J} = \mathbf{I} + \mathbf{S}_h$, leading to the yellow ($J = 1/2$) and green ($J = 3/2$) series. The band structure and energetic arrangement of the yellow and green lines are depicted in Fig. 2.2. The focus of this work is mainly on the yellow

excitons. As we will see in Chapters 3 and 4 a detailed study of the two series must take into account their mutual coupling by several parts of the Hamiltonian, most prominently the cubic band structure terms and the exchange interaction. We directly investigate the green excitons in Chapter 8; and in Chapter 9 we look at dipole transitions between the yellow and green series.

Electron and hole interact via the screened Coulomb potential

$$V(\mathbf{r}_e - \mathbf{r}_h) = -\frac{e^2}{4\pi\epsilon_0\epsilon|\mathbf{r}_e - \mathbf{r}_h|}, \quad (2.6)$$

with the positions of the electron \mathbf{r}_e and hole \mathbf{r}_h and the dielectric constant $\epsilon = \epsilon_{s1}$ in the low-frequency regime.

The material parameters used in our calculations are listed in Table A.1 in Appendix A.

2.3 | Central-cell corrections

The central-cell corrections are additional terms in the exciton Hamiltonian necessary for the correct modelling of excitons with small spatial extensions. This primarily concerns the states with principal quantum number $n \leq 2$.

2.3.1 Corrections to the dielectric constant

The electron and hole forming an exciton interact via the Coulomb interaction due to their opposite charges. This interaction is modified by the crystal environment, leading to the screened dielectric constant ϵ_s when the relative motion between electron and hole is slow as compared to the motion of the ionic cores of the crystal. For small principal quantum numbers, this condition is not fulfilled and the dielectric constant needs to be modified. If the motion of the electron and hole is much faster than the ionic cores, the electronic dielectric constant ϵ_b has to be used instead. The transition between these regimes takes place at the frequency of a given optical phonon branch, which controls the relevant motion of the crystal cores. In cuprous oxide, there are two relevant LO branches affecting the excitons of the yellow and green series. For a correct description, we need to model the behavior of the dielectric constant in the transition regions.

The basic potential resulting from the Fröhlich interaction with one phonon branch was derived and discussed by Haken [81–83]. Schweiner *et al.* [38] propose the following phenomenological generalization for two phonon branches,

$$V^H(r) = -\frac{e^2}{4\pi\epsilon_0 r} \left[\frac{1}{\epsilon_{s1}} + \frac{1}{2\epsilon_1^*} \left(e^{-r/\rho_{h1}} + e^{-r/\rho_{e1}} \right) + \frac{1}{2\epsilon_2^*} \left(e^{-r/\rho_{h2}} + e^{-r/\rho_{e2}} \right) \right].$$

The polaron radii

$$\rho_{e/hi} = \sqrt{\frac{\hbar}{2m_{e/h}\omega_{LOi}}} \quad (2.7)$$

are determined by the effective masses of the electron m_e and hole m_h , whereas the values of ϵ_i^* are given by

$$\frac{1}{\epsilon_i^*} = \frac{1}{\epsilon_{bi}} - \frac{1}{\epsilon_{si}}. \quad (2.8)$$

Here, $i = 1, 2$ denotes the two relevant LO phonon branches with the associated energies $\hbar\omega_{LOi}$. A more refined approach for the modelling of the dielectric constant in the transition regime is given by the Pollmann-Büttner potential [84]. The phenomenological extension to the case of two branches is given by

$$V^{\text{PB}}(r) = -\frac{e^2}{4\pi\epsilon_0 r} \left[\frac{1}{\epsilon_{s1}} + \frac{1}{\epsilon_1^*} \left(\frac{m_h}{m_h - m_e} e^{-r/\rho_{h1}} - \frac{m_e}{m_h - m_e} e^{-r/\rho_{e1}} \right) + \frac{1}{\epsilon_2^*} \left(\frac{m_h}{m_h - m_e} e^{-r/\rho_{h2}} - \frac{m_e}{m_h - m_e} e^{-r/\rho_{e2}} \right) \right]. \quad (2.9)$$

For small exciton extensions, the momentum dependence of the dielectric constant has to be accounted for. As outlined in [38] based on Ref. [85], this can be incorporated by a contact potential of the form

$$V_d = -V_0 V_{\text{uc}} \delta(\mathbf{r}). \quad (2.10)$$

Here, $V_{\text{uc}} = a_g^3$ denotes the volume of the unit cell. In Ref. [38], the value of V_0 is used as a fit parameter to account for additional small deviations between theory and experiment.

2.3.2 Exchange interaction

The exchange interaction is given in Ref. [38] and reads

$$H_{\text{exch}} = J_0 \left(\frac{1}{4} - \frac{1}{\hbar^2} \mathbf{S}_e \cdot \mathbf{S}_h \right) V_{\text{uc}} \delta(\mathbf{r}) = J_0 \left(1 - \frac{1}{2\hbar^2} \mathbf{S}^2 \right) V_{\text{uc}} \delta(\mathbf{r}), \quad (2.11)$$

where we use the total spin $\mathbf{S} = \mathbf{S}_e + \mathbf{S}_h$ in the last part of the equation. It leads to a splitting of states with S admixture depending on the relative alignment of the electron and hole spin. We discuss it in detail in Chapter 3.

With these abbreviations and depending on the choice between the Haken and the Pollmann-Büttner potential, the central-cell corrections can thus be written as

$$V_{\text{CCC}}^{\text{H/PB}} = V^{\text{H/PB}} + V_d + H_{\text{exch}}. \quad (2.12)$$

Most of the time, we will be using the simpler expression given by the Haken potential.

2.4 Application of external electric and magnetic fields

In many circumstances, the addition of external fields can be a valuable experimental tool for the modification and extraction of additional information from the spectrum. External fields reduce the symmetry of the system, lift selection rules and thus make additional lines visible. A prominent example of this is the electric field breaking the parity symmetry, and thus allowing for a mixture of the dipole-allowed odd-parity P states with the even parity states, like S and D states. To introduce an external electric field \mathcal{F} into our description of the system, we add the term [11]

$$H_{\mathcal{F}} = -e\mathcal{F} \cdot (\mathbf{r}_e - \mathbf{r}_h) \quad (2.13)$$

to the Hamiltonian (2.2).

The addition of an external magnetic field leads to more complicated expressions in the Hamiltonian. We perform the minimal coupling $\mathbf{p}_e \rightarrow \mathbf{p}_e + e\mathbf{A}(\mathbf{r}_e)$ and $\mathbf{p}_h \rightarrow \mathbf{p}_h - e\mathbf{A}(\mathbf{r}_h)$ with the vector potential for a homogeneous field $\mathbf{A}(\mathbf{r}_{e,h}) = (\mathbf{B} \times \mathbf{r}_{e,h})/2$. When considering a field with magnitude B along a particular direction, we can rearrange the resulting Hamiltonian as

$$H(B) = H(B=0) + eBH_1 + (eB)^2H_2 \quad (2.14)$$

The lengthy expressions for H_1 and H_2 in center-of-mass coordinates using the irreducible tensor formalism can be found in Ref. [65] for external magnetic fields pointed along the [001], [110], and [111] axes.

On top of these, we have to include the interaction of the spins and the magnetic field [65, 86]

$$H_B = \mu_B [g_c \mathbf{S}_e + (3\kappa + g_s/2) \mathbf{I} - g_s \mathbf{S}_h] \cdot \mathbf{B}/\hbar, \quad (2.15)$$

with the Bohr magneton μ_B , the g -factor of the electron g_c and the hole $g_s \approx 2$, and the fourth Luttinger parameter κ .

2.5 Center-of-mass transformation

The Hamiltonian (2.2) only depends on the coordinate difference $\mathbf{r}_e - \mathbf{r}_h$ and not on the coordinates of electron and hole individually. Because of this, the system has a translation symmetry and thus, the center-of-mass momentum is a good quantum number. We can exploit this to simplify our description by introducing center-of-mass coordinates,

using the following transformation [87, 88], which depends on a parameter α ,

$$\begin{aligned}\mathbf{r} &= \mathbf{r}_e - \mathbf{r}_h, & \mathbf{R} &= \alpha\mathbf{r}_e + (1 - \alpha)\mathbf{r}_h, \\ \mathbf{k} &= (1 - \alpha)\mathbf{p}_h - \alpha\mathbf{p}_e, & \mathbf{K} &= \mathbf{p}_e + \mathbf{p}_h.\end{aligned}\tag{2.16}$$

This means that we have to perform the following substitutions in the Hamiltonian (2.2),

$$\begin{aligned}\mathbf{r}_h &= \mathbf{R} - \alpha\mathbf{r}, & \mathbf{r}_e &= \mathbf{R} + (1 - \alpha)\mathbf{r}, \\ \mathbf{p}_h &= \mathbf{k} + \alpha\mathbf{K}, & \mathbf{p}_e &= -\mathbf{k} + (1 - \alpha)\mathbf{K}.\end{aligned}\tag{2.17}$$

In general α and $1 - \alpha = \gamma$ can also be tensor-valued. In Ref. [89], this transformation is used with $\alpha = m_e/(m_e + m_h)$, leading to

$$\begin{aligned}\mathbf{r} &= \mathbf{r}_e - \mathbf{r}_h, & \mathbf{R} &= \frac{m_h\mathbf{r}_h + m_e\mathbf{r}_e}{m_h + m_e}, \\ \mathbf{P} &= \hbar\mathbf{K} + \frac{e}{2}\mathbf{B} \times \mathbf{r} = \mathbf{p}_e + \mathbf{p}_h, & \mathbf{p} &= \frac{m_h\mathbf{p}_e - m_e\mathbf{p}_h}{m_h + m_e}.\end{aligned}\tag{2.18}$$

Here m_h is the hole mass, \mathbf{r} denotes the relative coordinate and \mathbf{R} the position of the center of mass. The corresponding momenta are given by \mathbf{p} and \mathbf{P} . The pseudomomentum \mathbf{K} is a constant of motion related to the center-of-mass momentum [88]. Unless stated otherwise, we assume vanishing center-of-mass pseudomomentum $\mathbf{K} = 0$.

In a hydrogenlike system without the band structure terms, this transformation leads to a Hamiltonian where the center-of-mass motion is not coupled to the relative motion. In our system, the resulting Hamiltonian has the form

$$H(\alpha = m_e/(m_e + m_h)) = H_0 + \hbar K H_1 + \hbar^2 K^2 H_2,\tag{2.19}$$

where the expressions for H_0 , H_1 and H_2 can be found in Ref. [89] for various directions of \mathbf{K} .

In general, polariton effects have to be considered when the center of mass momentum \mathbf{K} is nonzero. The experimental results in Refs. [90–92] on the other hand show, that the polariton effects for the $1S$ state are of the order of $10 \mu\text{eV}$ and thus small in comparison with the effects considered in this work. Furthermore, a recent discussion by Stolz *et al.* [74] concluded that polariton effects should only be observable in transmission experiments for $n \geq 28$. Hence, we will not include them in our discussion.

2.6 Resonances and complex energies

In textbook Hermitian quantum mechanics, the Hamiltonian, being a Hermitian operator is diagonalized to obtain the real energy eigenvalues. The associated square-integrable eigenstates represent bound states with infinite lifetimes. Together with the continuum

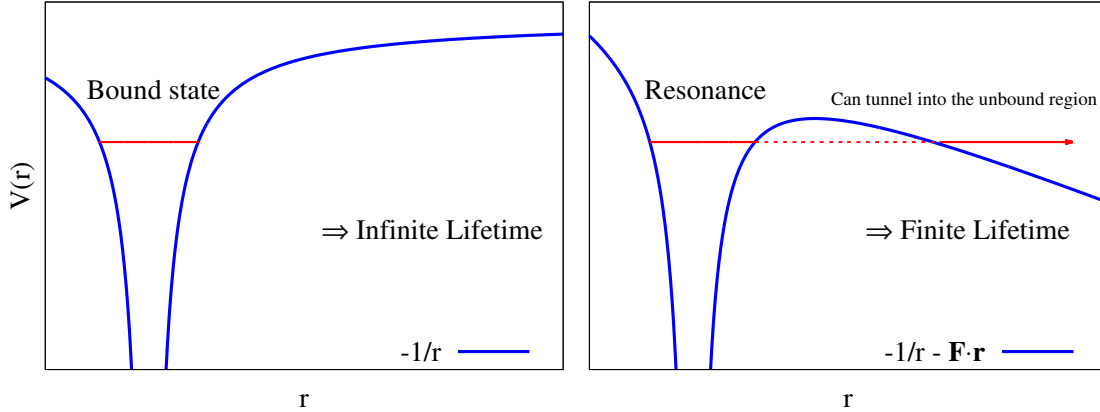


Figure 2.3.: The application of an external electric field can transform bound states into resonant states with finite lifetimes. As illustrated for the example of the Coulomb potential, this can be understood as a modification of the potential allowing the system to tunnel into the unbound region.

part of the spectrum, this formalism can in principle be used to handle all kinds of bound systems and scattering problems. Nevertheless, its most immediate application is to closed systems, where bound states have infinite lifetimes and it is less suited to the handling of metastable systems, like for example unstable particles subject to radioactive decay. For the latter's description, we instead move away from the Hermitian formalism.

Metastable states, or resonant states, have a finite decay rate Γ . We introduce a complex energy $E - i\hbar\Gamma/2$. Plugging this into the time evolution of the state, we obtain

$$|\psi(t)\rangle = \exp\left[-\frac{i}{\hbar}\left(E - i\hbar\frac{\Gamma}{2}\right)t\right] |\psi(0)\rangle. \quad (2.20)$$

For the modulus-square of the amplitude, this results in

$$|\psi(t)|^2 = \langle\psi(t)|\psi(t)\rangle = \exp(-\Gamma t) |\psi(0)|^2. \quad (2.21)$$

We thus see that the probability of finding the system in the metastable state decays exponentially with the decay rate Γ , as intended.

Since the introduced energies $E - i\hbar\Gamma/2$ are complex, they cannot be calculated as the eigenvalues of a Hermitian Hamiltonian in a straightforward way. But they can be the eigenvalues of a non-Hermitian operator. When discussing quasibound resonances, we use the complex-coordinate-rotation method to modify the Hamiltonian of the system, making it non-Hermitian. We then calculate the resonant states and associated complex energies by diagonalizing the rotated Hamiltonian. This also allows for the calculation of absorption spectra. Due to the finite imaginary part of the energy and the complex oscillator strengths, resonances in general appear as asymmetric Lorentz profiles instead of sharp delta peaks. Scattering processes with phonons are the most prominent cause

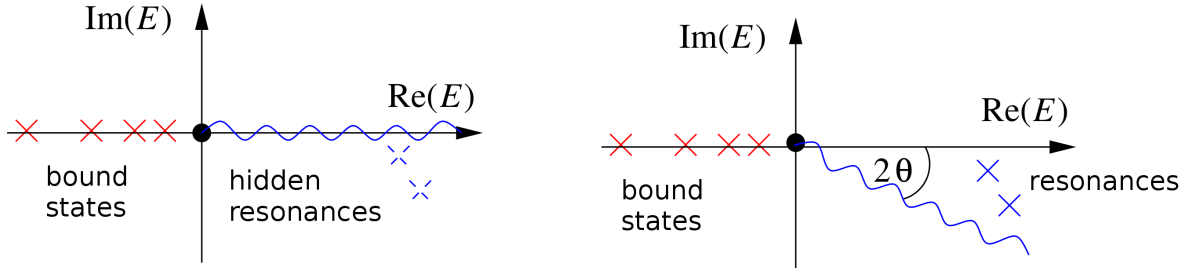


Figure 2.4.: Scheme of the complex-coordinate-rotation method. Resonances in the complex energy plane are hidden in Hermitian quantum mechanics but can be revealed by the complex-coordinate-rotation method. States representing the continuum are rotated into the complex plane by the angle 2θ around the respective threshold. Adapted from Ref. [93].

of line broadening for the excitons in cuprous oxide. The appropriate theory was developed in the 1950s and 60s by Toyozawa [70–72] and was recently used to calculate the linewidths to reasonable agreement with experiment [73, 74]. In our discussion of excitons, we will not focus on these effects. In this work, we instead encounter resonances mostly in two contexts. Firstly, resonant states appear in the spectrum when an external electric field is applied, as depicted in Fig. 2.3. Secondly, the green exciton states lie above the band gap of the yellow series and are coupled to the yellow continuum. Hence, they form quasi-bound resonances rather than bound states, even without considering external fields and the coupling to the phonons.

2.7 | Complex-coordinate-rotation method

To compute the complex eigenenergies, we perform the complex-coordinate rotation $\mathbf{r} \rightarrow \mathbf{r}e^{i\theta}$ [94–96]. It is important to note that, under the complex-coordinate rotation, the Hamiltonian (2.2) becomes a non-Hermitian operator, and thus allows for complex-valued eigenenergies, as schematically illustrated in Fig. 2.4. Continuum states are rotated into the lower complex energy plane, revealing the resonances, which are *hidden* in a Hermitian eigenvalue problem. If the rotation angle θ is chosen appropriately, the resonance states become square integrable.

In the Hermitian formalism, the wave functions ψ associated with resonances are not normalizable and thus are not part of the Hilbert space. They fulfill the Schrödinger equation

$$H\psi = E\psi \quad (2.22)$$

with a complex energy E . We introduce the complex scaling operation S_θ with

$$S_\theta\psi(\mathbf{r}) = \psi(\mathbf{r}e^{i\theta}). \quad (2.23)$$

Note that formally the operator S_θ can be applied to a state $|\psi\rangle$ in arbitrary representation, however, Eq. (2.23) is only valid in coordinate representation as used throughout this work. For sufficiently large θ , $S_\theta\psi$ becomes square integrable [94]. The rotated Schrödinger equation is given by

$$S_\theta H S_\theta^{-1} S_\theta \psi = E S_\theta \psi. \quad (2.24)$$

We thus want to find eigenvalues and normalizable eigenfunctions of the rotated Hamiltonian

$$H' = S_\theta H S_\theta^{-1}. \quad (2.25)$$

The energies of the bound states are unaffected by the rotation, whereas the continuum is rotated into the lower complex plane by the angle 2θ and the positions of the quasibound resonance states are revealed. For sufficiently large angles, these are independent of the value of θ . Expressing $S_\theta\psi$ in a basis $\{\phi_i\}$, we obtain

$$S_\theta|\psi\rangle = \sum_i c_i |\phi_i\rangle \quad (2.26)$$

and

$$\sum_i \langle S_\theta^{-1} \phi_j | H | S_\theta^{-1} \phi_i \rangle c_i = E \sum_i \langle S_\theta^{-1} \phi_j | S_\theta^{-1} \phi_i \rangle c_i. \quad (2.27)$$

The solution can thus be obtained by using the rotated basis set $\{|S_\theta^{-1}\phi_i\rangle\}$ with the unchanged Hamiltonian H .

2.8 Numerical diagonalization

In this section, we outline the numerical procedure for the calculation of eigenvalues and eigenstates used in this thesis. Using a complete basis set, we transform the Schrödinger equation into a generalized eigenvalue problem, which is then solved numerically.

2.8.1 Generalized eigenvalue problem

To numerically calculate the eigenvalues and eigenstates of the exciton problem, we first express the stationary Schrödinger equation in a complete basis. For the orbital angular part, we utilize the spherical harmonics with quantum numbers L and M . Additional quantum numbers have to be introduced to treat the quasispin \mathbf{I} as well as the electron and hole spins \mathbf{S}_e and \mathbf{S}_h . For our basis, we first couple the hole spin and the quasispin to the effective hole spin $\mathbf{J} = \mathbf{I} + \mathbf{S}_h$. Next we introduce the angular momentum $\mathbf{F} = \mathbf{J} + \mathbf{L}$ and finally add the electron spin \mathbf{S}_e to get the total angular momentum $\mathbf{F}_t = \mathbf{F} + \mathbf{S}_e$. Note that the basis functions belonging to the quasispin \mathbf{I} transform

2. Theoretical background

according to the irreducible representation Γ_5^+ in Cu_2O instead of the usual Γ_4^+ for a spin of unity. However, since $\Gamma_5^+ = \Gamma_4^+ \otimes \Gamma_2^+$, we can perform the standard coupling of angular momenta and, to obtain the appropriate symmetry of the total state, multiply with Γ_2^+ at the end. For the radial part we use the Coulomb-Sturmian functions [35, 97, 98]

$$U_{N,L} = N_{N,L,\alpha} \left(\frac{2r}{\alpha}\right)^L e^{-\frac{r}{\alpha}} L_N^{2L+1} \left(\frac{2r}{\alpha}\right) \quad (2.28)$$

with the associated Laguerre polynomials $L_n^m(x)$ and a normalization factor $N_{N,L,\alpha}$. Here, N is the radial instead of the principal quantum number. The parameter α can in principle be freely chosen, but influences the convergence of the matrix diagonalization. It can also be used for the implementation of the complex scaling operation, allowing for the calculation of complex resonance states. To this end, a complex-valued $\alpha = |\alpha|e^{i\theta}$ is chosen, resulting in the complex rotation with angle θ . In total we thus get the basis states

$$|\Pi\rangle = |N, L; (I, S_h), J; F, S_e; F_t, M_{F_t}\rangle, \quad (2.29)$$

where we use $\Pi = \{N, L; (I, S_h), J; F, S_e; F_t, M_{F_t}\}$ as an abbreviation for the set of used quantum numbers. This basis has the advantage of being complete without the inclusion of the hydrogen continuum, but it is not orthogonal with respect to the standard scalar product.

Following Refs. [35, 65], we express the Hamiltonian in spherical tensor notation. We will investigate spectra with $\mathbf{B} \parallel [001]$, $[110]$ and $[111]$. In each case, we will choose the quantization axis to be along the magnetic field and perform an according rotation on the Hamiltonian. The expressions obtained for the Hamilton operator are found in Ref. [65]. Using the ansatz

$$|\Psi\rangle = \sum_{\Pi} c_{\Pi} |\Pi\rangle \quad (2.30)$$

for the exciton wave function $|\Psi\rangle$, the Schrödinger equation gets the form of a generalized eigenvalue problem,

$$\mathbf{H}\mathbf{c} = E\mathbf{M}\mathbf{c}, \quad (2.31)$$

with the Hamiltonian matrix \mathbf{H} and the overlap matrix \mathbf{M} . To obtain finite matrices and vectors, we introduce cut-offs to the quantum numbers $N + L + 1 \leq n_{\max}$ and $F \leq F_{\max}$. These parameters, together with $|\alpha|$ and, if the complex rotation is performed, the rotation angle θ have to be chosen appropriately to ensure properly converged results. Good convergence is reached when variations of the parameters do not lead to significant changes in the calculated spectra. The solution is obtained by using a suitable LAPACK or ARPACK routine [99, 100] and we thus get the eigenvalues E and the vector of coefficients \mathbf{c} in the basis expression (2.30). When delta-terms are included in the Hamiltonian, we first diagonalize it without them. We then set up a second eigenvalue problem including the delta terms using only the converged eigenstates obtained in the first diagonalization.

2.8.2 Oscillator strengths

The extraction of the dipole oscillator strengths is performed analogously to the calculation presented in Ref. [65]. If the quantization axis is chosen along the [001]-axis, we obtain them as follows. For the relative dipole oscillator strengths we use

$$f_{\text{rel},D} \sim \left| \lim_{r \rightarrow 0} \frac{\partial}{\partial r} \langle \pi_i | \Psi(\mathbf{r}) \rangle \right|^2 \quad (2.32)$$

for light linearly polarized in x -, y -, or z -direction. The states $|\pi_i\rangle$ are given by

$$|\pi_x\rangle = \frac{i}{\sqrt{2}} [|2, -1\rangle_D + |2, 1\rangle_D], \quad (2.33a)$$

$$|\pi_y\rangle = \frac{1}{\sqrt{2}} [|2, -1\rangle_D - |2, 1\rangle_D], \quad (2.33b)$$

$$|\pi_z\rangle = \frac{i}{\sqrt{2}} [|2, -2\rangle_D - |2, 2\rangle_D], \quad (2.33c)$$

where $|F_t, M_{F_t}\rangle_D$ is an abbreviation [65] for

$$\begin{aligned} & |(S_e, S_h) S, I; I + S, L; F_t, M_{F_t}\rangle \\ = & |(1/2, 1/2) 0, 1; 1, 1; F_t, M_{F_t}\rangle. \end{aligned} \quad (2.34)$$

In this state, the electron and hole spin S_e and S_h are coupled to the total spin S . This is combined first with the quasispin I and then with the orbital angular momentum L to obtain the total angular momentum F_t . M_{F_t} is the projection onto the axis of quantization.

Similarly, for the relative quadrupole oscillator strength, we calculate the overlaps

$$f_{\text{rel},Q} \sim \left| \lim_{r \rightarrow 0} \langle \pi_i^Q | \Psi(\mathbf{r}) \rangle \right|^2 \quad (2.35)$$

with the states [89]:

$$\begin{aligned} |\pi_{yz}^Q\rangle &= \frac{1}{\sqrt{2}} (|1, -1\rangle_Q - |1, 1\rangle_Q), \\ |\pi_{xz}^Q\rangle &= \frac{i}{\sqrt{2}} (|1, -1\rangle_Q + |1, 1\rangle_Q), \\ |\pi_{xy}^Q\rangle &= |1, 0\rangle_Q, \end{aligned} \quad (2.36)$$

with the different abbreviation

$$\begin{aligned} |F_t, M_{F_t}\rangle_Q &= |S, I; I + S, L; F_t, M_{F_t}\rangle \\ &= |0, 1; 1, 0; 1, M_{F_t}\rangle. \end{aligned} \quad (2.37)$$

2. Theoretical background

We give the formulas for other quantization axes in Sec. 6.1.

Generally, only exciton states with irreducible representation Γ_4^- can couple to the dipole operator, and only those can therefore be accessed in one-photon absorption experiments in dipole approximation. In cuprous oxide, these are predominantly the odd-parity P excitons; due to the mixing of angular momentum F states receive a dipole oscillator strength as well. Similar reasoning holds for the quadrupole transitions, which primarily affect Γ_5^+ S excitons with even parity, and D excitons due to admixtures. A comprehensive list of yellow exciton states in cuprous oxide with assigned irreducible representations up to principal quantum number $n = 5$ is given in Ref. [38]. We present similar data for the green series in Appendix B.

3

The exchange interaction in the yellow series

In this chapter, we investigate the exchange interaction of the yellow excitons in cuprous oxide, which was introduced in Chapter 2 as one of the central-cell corrections necessary for the accurate description of the even-parity states. By varying the material parameters in the numerical calculations, we can interpret experimental findings and understand their origin in the complex band structure and central-cell corrections. In particular, we discuss the experimental observation of the reversal of the ortho- and paraexciton for the 2S yellow exciton, and explain this phenomenon by an avoided crossing with the green 1S orthoexciton in a detailed numerical analysis. Furthermore, we discuss the exchange splitting as a function of the principal quantum number n and its deviation from the n^{-3} behavior expected from a hydrogenlike model. We also explain why the observed exchange splitting of the green 1S exciton is more than twice the splitting of the yellow 1S state. The results of this chapter are the subject of Ref. [101].

The yellow exciton series in cuprous oxide has been shown to closely match a hydrogenlike system in many respects [30]. Still, there are a number of characteristic effects of the complex band structure. For example, a fine structure splitting between P and F states can be observed [102]. In the case of small radii, additional central-cell corrections to the valence band Hamiltonian have to be added to achieve a satisfactory description [38]. Due to the cubic symmetry of the crystal, the angular momentum is not a good quantum number anymore, and thus the S states with small extension are also coupled to other angular momenta, such as the D states. This is especially important when considering the green 1S state, which lies in between the yellow spectrum. Because of this coupling, the central-cell corrections also affect the energetically higher lying states of the yellow series.

The exchange interaction, which is part of the central-cell corrections, causes a characteristic splitting between states depending on the relative alignment of the electron and hole spins, i.e., between the spin-singlet and spin-triplet states. The spin-triplet dark exciton states have been proposed for use in quantum computational applications and for the possible realization of a Bose-Einstein condensate [103–105]. The dark paraexci-

ton series in cuprous oxide is not accessible by electric dipole and quadrupole absorption experiments, because the paraexcitons have no spin-singlet component and are therefore spin-flip forbidden to all orders in electric transitions. This selection rule can be circumvented using stress [106] or by application of an external magnetic field which leads to a mixing between spin-singlet and triplet states [107, 108]. The experimental group of M. Bayer at TU Dortmund University used magnetic-field-induced Second Harmonic Generation (SHG) spectroscopy for the measurements of the paraexcitons, extrapolating their magnetic-field dependent energies to zero field strength.

A naive treatment of the exchange interaction leads to the expectation that the orthoexciton is shifted to higher energies than the paraexciton, a result in line with Hund's rule. Numerical calculations have shown that this expectation is contradicted in the case of the yellow 2S exciton state in cuprous oxide [38]. This has now been confirmed in experiments by Farenbruch *et al.* [63]. They explain this by appealing to the influence of the green 1S state. In this chapter, we discuss and confirm this explanation in greater detail, using the possibility of changing the material parameters in the numerical simulations to study the spectrum in experimentally inaccessible ways. Going beyond the discussion in Ref. [63], we present the precise mechanism responsible for the reversed energies of the 2S ortho- and paraexcitons. We then study the exchange splitting as a function of the principal quantum number n . Based on a hydrogenlike calculation, the splitting is expected to decrease with n^{-3} . For the yellow excitons in cuprous oxide, there are deviations from this. We numerically investigate the origin of these deviations. We finally study why the exchange splitting of the green 1S state is more than twice the exchange splitting of the yellow 1S state. To the best of our knowledge, this represents the first detailed discussion of these features of the dark exciton series in cuprous oxide.

We outline the theoretical and experimental background of the presented data in Secs. 3.1 and 3.2. We then discuss the reversal between the 2S ortho- and paraexcitons in Sec. 3.3, the exchange splitting as a function of the principal quantum number in Sec. 3.4 and the splitting of the yellow 1S state versus the green 1S state in Sec. 3.5.

3.1 | The exchange interaction

We study the yellow series with the addition of the green 1S state as described by the field-free Hamiltonian (2.2),

$$H = E_g + H_e(\mathbf{p}_e) + H_h(\mathbf{p}_h) + V(\mathbf{r}_e - \mathbf{r}_h) + V_{\text{CCC}}^{\text{H}}(\mathbf{r}) , \quad (3.1)$$

with the central-cell corrections using the Haken potential. Our emphasis will be on the exchange interaction,

$$H_{\text{exch}} = J_0 \left(1 - \frac{1}{2\hbar^2} \mathbf{S}^2 \right) V_{\text{uc}} \delta(\mathbf{r}) , \quad (3.2)$$

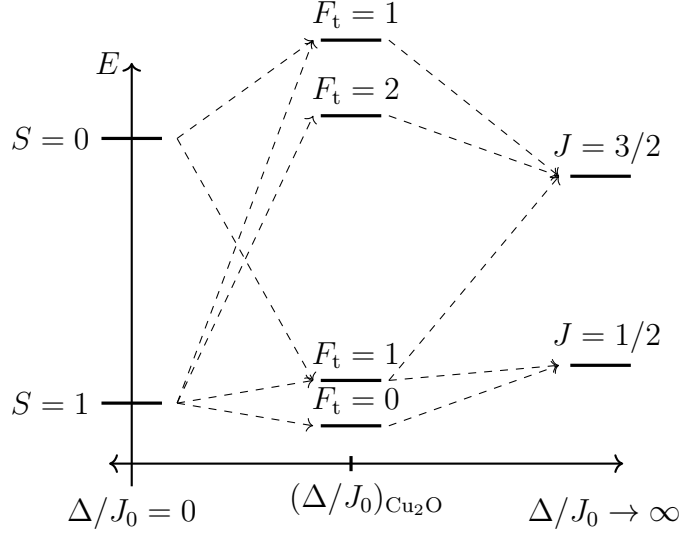


Figure 3.1.: Level scheme of S states as a function of the ratio between the exchange interaction strength J_0 and the spin-orbit coupling Δ . For $L = 0$, the total angular momentum F_t can be obtained by either coupling the quasispin of the hole \mathbf{I} with the total spin $\mathbf{S} = \mathbf{S}_e + \mathbf{S}_h$ or by coupling the electron spin \mathbf{S}_e with the effective hole spin $\mathbf{J} = \mathbf{I} + \mathbf{S}_h$. According to Eq. (2.11), the $S = 0$ singlet states are lifted above the $S = 1$ triplet states for vanishing spin-orbit coupling Δ . For $\Delta/J_0 \rightarrow \infty$, the splitting between the green $J = 3/2$ and yellow $J = 1/2$ states predominates. For general values in between, the levels split according to the total angular momentum F_t . As discussed in Sec. 3.5 with reference to the matrix element (3.5), for both the green and yellow S states, the $F_t = 1$ states are lifted above the $F_t = 2$ and $F_t = 0$ states, respectively.

which is part of the central-cell corrections $V_{\text{CCC}}^{\text{H}}(\mathbf{r})$. We first take a closer look at the exchange interaction (2.11) in the following.

We first note, that only $L = 0$ states are affected due to the presence of the δ term. From Eq. (3.2) it is clear, that the effect is a lifting of the states with $S = 0$ over the states with $S = 1$. When taking into account the quasispin \mathbf{I} in the crystal, S is not a good quantum number anymore, and we additionally need to consider the spin-orbit coupling given in Eq. (2.5). In Fig. 3.1 we show the level scheme of the S states caused by the competition between the exchange interaction and the spin-orbit coupling as a function of the ratio Δ/J_0 . Note that for the yellow $J = 1/2$ states only the threefold degenerate $F_t = 1$ orthoexcitons have an $S = 0$ component and are therefore dipole allowed. Here, $\mathbf{F}_t = \mathbf{J} + \mathbf{S}_e = \mathbf{I} + \mathbf{S}$ is the total angular momentum. While the singlet state $S = 0$ is lifted above the triplet state $S = 1$, it is the threefold degenerate $F_t = 1$ state which is

lifted above the non-degenerate $F_t = 0$ state, when only considering the yellow $J = 1/2$ states.

We want to perform a quick calculation to understand the behavior of the exchange interaction in a simplified model. This will allow us to investigate the impact of the correction terms, i.e., the band structure and central-cell corrections, by comparing our findings here with the results of the exact numerical calculation further below. Evaluating the integral for the matrix elements of the exchange interaction (2.11) with wave functions ψ_1 and ψ_2 over the δ term leads to a proportionality to $\psi_1^*(0)\psi_2(0)$. In a hydrogenlike model we choose the S states $\psi_1 = \psi_2 = \psi_{n,L=0,M=0}$. This yields

$$\langle n, L = 0, M = 0 | H_{\text{exch}} | n, L = 0, M = 0 \rangle = J_0 \left(1 - \frac{1}{2\hbar^2} \mathbf{S}^2 \right) V_{\text{uc}} \left(\frac{1}{\pi n a_{\text{B}}} \right)^3, \quad (3.3)$$

with the Bohr radius a_{B} . The relative energetic placement of multiplet states affected by the exchange interaction does not depend on the principal quantum number n in the hydrogenlike model, but only the strength of the splitting, since n affects only an overall factor. As will be shown in Sec. 3.3, this does not hold in the case of the yellow excitons in cuprous oxide, where ortho- and paraexcitons are reversed for $n = 2$. For the other principal quantum numbers, the order of states is as shown in Fig. 3.1. Additionally, the splitting decreases with n^{-3} as a function of the principal quantum number in the simplified model. The situation is more complicated for the yellow exciton series in cuprous oxide, which will be more thoroughly discussed in the following. To this end, we use numerical results obtained by diagonalizing the Hamiltonian as described in Sec. 2.8 and compare with experimental data obtained by Farenbruch *et al.* [101].

3.2 | Source of experimental data

The presented experimental data was obtained by the research group of M. Bayer at the TU Dortmund. To experimentally observe the dark excitons, the method in Ref. [109] was modified by additionally applying a magnetic field to optically activate the paraexcitons, leading to an orthoexciton admixture. The resulting paraexciton energy position as a function of the magnetic field strength is well approximated by a parabola. This makes it possible to extrapolate the observed energies to vanishing field strength.

The presented data was obtained in SHG experiments, using 200 fs laser pulses with a spectral width of 10 meV. The sample was cooled down to 1.4 K. Further details are given in Ref. [109].

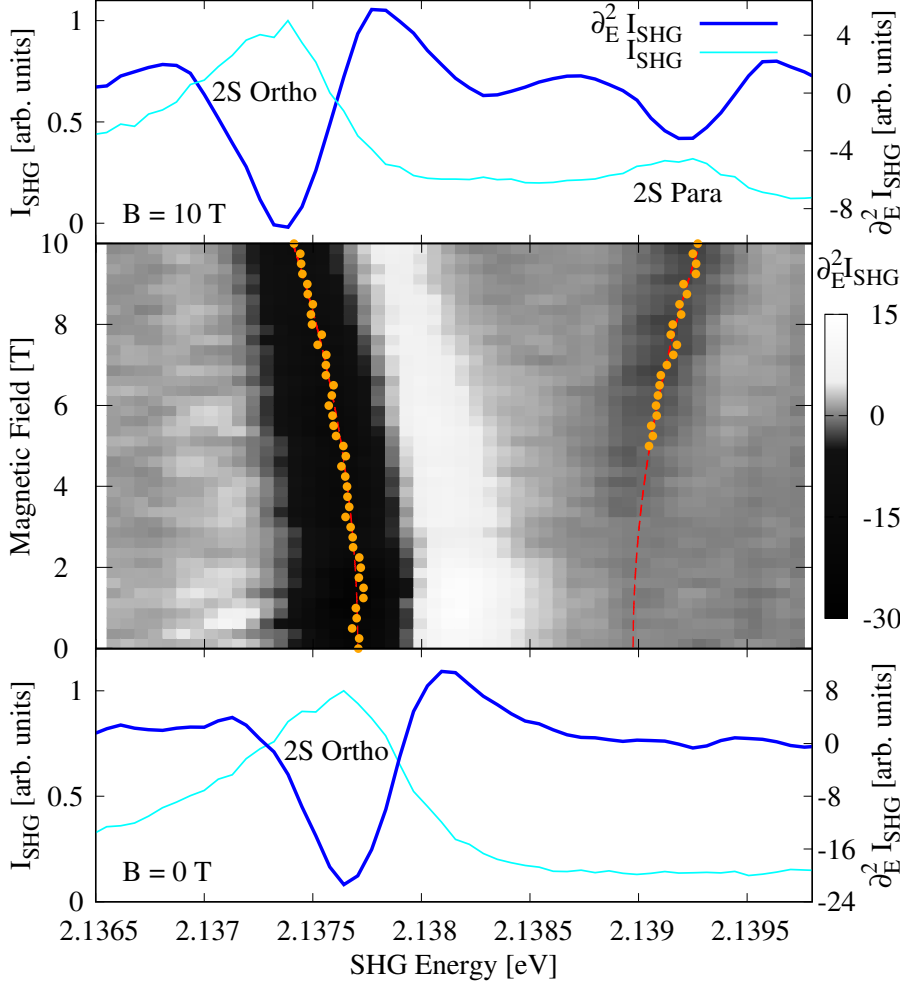


Figure 3.2.: Experimental SHG spectrum of the yellow 2S ortho- and paraexcitons. The wave vector \mathbf{K} is parallel to the $[111]$ axis and the magnetic field is applied in Voigt geometry along the $[11\bar{2}]$ direction. The polarizations of the incoming and outgoing light are parallel to the magnetic field. We show a contour plot of the second derivative of the SHG intensity in gray scale. The positions of the ortho- and paraexcitons extracted by a Gaussian fit to the SHG intensity are marked with orange dots. Using a quadratic fit (red dashed line), we can extrapolate the energy of the paraexciton to $E_{B=0\text{T}}^{2S,\text{para}} = 2.13897$ eV at vanishing magnetic field. An analogous fit to the orthoexciton energies yields an energy $E_{B=0\text{T}}^{2S,\text{ortho}} = 2.13771$ eV at vanishing magnetic field. The top and bottom panels show the SHG intensity and its second derivative at a magnetic field $B = 10$ T and $B = 0$ T, respectively.

3.3 Reversal of yellow 2S ortho- and paraexcitons

In this section, we first briefly recapitulate the experimental observation of the positions of the yellow 2S ortho- and paraexcitons, presenting additional data not shown in Ref. [63]. Note that we assign the labels *green* and *yellow*, as well as the principal and angular quantum numbers in accordance with the assignments given in Ref. [38]. We then present the underlying mechanisms. Since the paraexciton is spin-flip forbidden in electrical dipole and quadrupole transition experiments, a magnetic field was used to make them experimentally accessible. It is possible to include this magnetic field in the Hamiltonian introduced in Sec. 2.2, see for example Refs. [65, 110, 111]. Here, we extrapolate the experimental values to vanishing magnetic field and analyze those in the numerical calculations. We therefore do not consider the magnetic field in the theory.

In the central panel of Fig 3.2, we show a contour plot of the second derivatives of the SHG spectra of the 2S excitons. The corresponding SHG intensity measured at a magnetic field of 10 T and 0 T are presented in the top and bottom panel respectively. Spectra are measured with a resolution of $80 \mu\text{eV}$ from 0 T to 10 T in steps of 0.25 T in order to demonstrate the spectral shift of the 2S para- and orthoexciton in a magnetic field. The wave vector is directed along the SHG-allowed $[111]$ axis and the magnetic field is applied orthogonally to this in the $[11\bar{2}]$ direction. The polarization of the incoming and outgoing light is parallel to the magnetic field, i.e. $\mathbf{E}^{\text{in}} \parallel \mathbf{E}^{\text{out}} \parallel [11\bar{2}]$. This leads to a nonvanishing SHG signal of the paraexciton as discussed in Ref. [112]. It is much weaker than the intensity of the orthoexciton and only faintly becomes visible at about 5 T. We therefore extrapolate the position of the paraexciton to zero magnetic field, using a quadratic fit. We obtain $E_{B=0\text{T}}^{2\text{S,para}} = 2.13897 \text{ eV}$ for the paraexciton and $E_{B=0\text{T}}^{2\text{S,ortho}} = 2.13771 \text{ eV}$ for the orthoexciton. We can therefore experimentally confirm one of the curious features of the yellow paraexciton series in cuprous oxide predicted by Schweiner *et al.* in Ref. [38], viz. the observation that the 2S paraexciton is located at a higher energy than the 2S orthoexciton. This shows that the experimentally observed behavior of the yellow excitons here is qualitatively different from the hydrogenlike model in this respect. Farenbruch *et al.* identify the origin of this reversal in the influence of the green 1S exciton [63]. In the following, we want to corroborate this with a detailed numerical analysis.

In Fig. 3.3(a) we show the exchange splitting for the yellow 2S state as a function of the parameter J_0 , with the green states removed from the spectrum. For this calculation, we only used states with $J = 1/2$ in the basis. We see that in this case, the exchange interaction lifts the orthoexciton above the paraexciton as predicted. This confirms that the mixing with the 1S green orthoexciton is responsible for the surprising reversal, because without the green state, the reversal is absent.

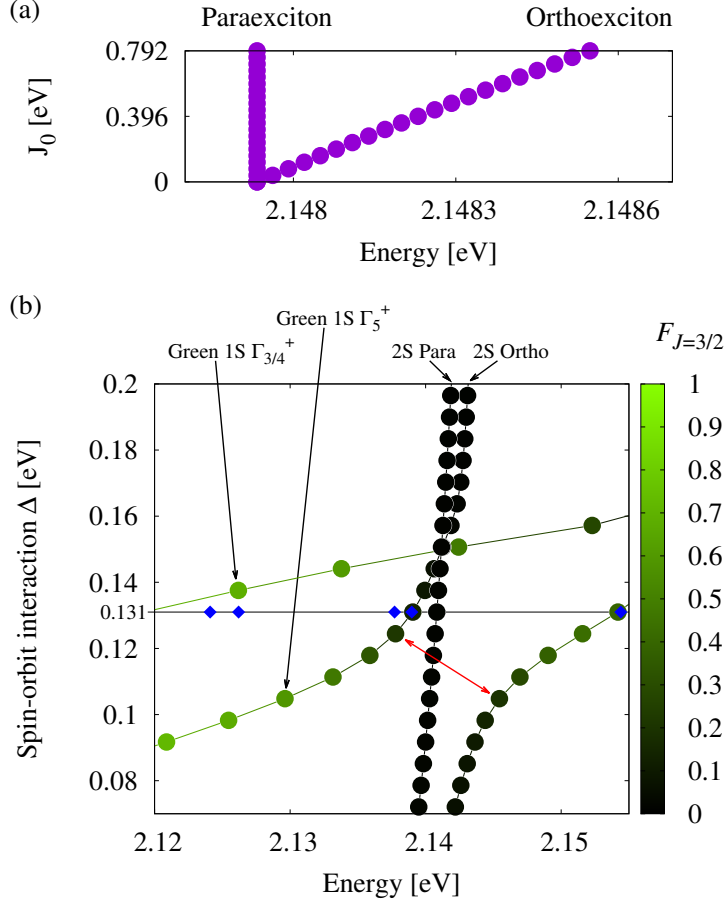


Figure 3.3.: (a) Splitting of the yellow 2S ortho- and paraexciton as a function of the strength of the exchange interaction J_0 when only the yellow $J = 1/2$ basis states are used for the diagonalization. In this case we observe that the orthoexciton is lifted above the paraexciton as expected. The exchange interaction is fully switched on for $J_0 = 0.792$ eV [38]. This shows that the exchange of the positions of the para- and orthoexciton has to originate in the influence of the green states. In (b), we show the responsible avoided crossing in the spectrum near the yellow 2S orthoexciton state as a function of the spin-orbit coupling Δ . We added lines to help guide the eyes. The green admixture $F_{J=3/2}$ to the states is indicated by the color bar. The horizontal line at $\Delta = 0.131$ eV marks the actual value of Δ in cuprous oxide. The avoided crossing between the yellow 2S orthoexciton and the Γ_5^+ green 1S state is marked in red. We point out that the green Γ_3^+ and Γ_4^+ states are degenerate in our model calculations, but show a small splitting in the experiment. This splitting is compatible with the cubic symmetry of the crystal, but the effect is not captured by our Hamiltonian.

For a better understanding, we calculate the positions of the yellow 2S and green 1S states as a function of the spin-orbit coupling, revealing an avoided crossing. In Fig. 3.3(b) we show this avoided crossing between the yellow 2S and the green 1S orthoexciton. The green admixture of the states given by the expectation value

$$F_{J=3/2} = \langle \psi | P_{J=3/2} | \psi \rangle, \quad (3.4)$$

of the projection operator onto the $J = 3/2$ Hilbert space for the exciton state ψ is indicated by the color bar. Using this green $J = 3/2$ fraction we can identify the green states coming from the left-hand side and follow them through the crossing. This avoided crossing was already noted in Ref. [38], but the implications for the relative placement of the 2S para- and orthoexcitons was not discussed. We can see that the avoided crossing leads to the yellow 2S orthoexciton being placed below the 2S paraexciton for the actual value of the spin-orbit coupling $\Delta = 0.131$ eV. For higher values at $\Delta \approx 0.15$ eV, the ortho and paraexcitons cross each other again, when the influence of the green Γ_5^+ 1S state is small enough. This further confirms and elucidates the influence of the mixing between the yellow and green series and its importance for a detailed understanding of the yellow excitons.

3.4 Dependence of the exchange splitting on the principal quantum number

Since the removal of the mixing with the green 1S state restores the expected placement of ortho- and paraexcitons also in the case of the yellow 2S state, it is a natural question whether the exchange splitting decreases with the third power of the principal quantum number n^{-3} as in the hydrogenlike model, Eq. (3.3). In this section we want to investigate the exchange splitting of the yellow S excitons as a function of n . To remove the influence of the green 1S states, we only use the basis states with $J = 1/2$ belonging to the yellow series for the calculations here. In Fig. 3.4(a) we compare the numerical data for the full basis extracted from Table III in Ref. [38] with the exchange splitting if the influence of the green states is removed. We additionally show the actual experimental values for reference. A fit of the form $\Delta E_{\text{exch}}(n) = An^B$ reveals an exponent $B = -3.34$ still differing from the expected $B = -3$ in the hydrogenlike model.

We identify two factors that explain this discrepancy. On the one hand, the Haken potential modifies the dielectric constant for small radii. This leads to a change in the effective Bohr radius and thus to a change in the value of the wave function at the origin. This disproportionally affects small quantum numbers, and thus changes the dependency of the splitting on n . On the other hand, the exchange interaction is not diagonal in the principal quantum number, i.e., the 2S state also influences the 1S state and so on. Going back to Eq. (2.11), we see that the matrix elements do not necessarily vanish if

3.4. Dependence of the exchange splitting on the principal quantum number

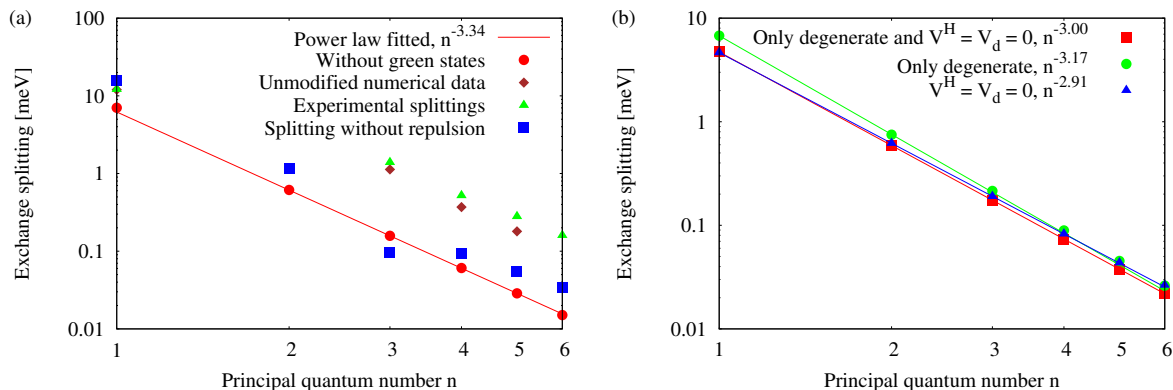


Figure 3.4.: Exchange splitting of the yellow excitons as a function of the principal quantum number n . To remove the influence of the green 1S exciton, only basis states with $J = 1/2$ were used. (a) Comparison of exchange splitting with (brown diamonds) and without (red circles) the influence of the green 1S state. Unmodified numerical data were taken from Ref. [38]. We additionally show the experimental values (green triangles) for reference. The blue squares show the splittings if the green state is included but the level repulsion between the green and yellow states due to the δ terms in the central-cell corrections is removed. (b) Exchange splitting as a function of n for modified material parameters, again with only the yellow $J = 1/2$ basis states. We show data where we removed the influence of the Haken potential (blue triangles), data where we diagonalized the exchange interaction only in the degenerate S spaces, neglecting the coupling between different principal quantum numbers (green circles) and data where we combined the previous two conditions (red squares). The fits show that only the combination of all modifications leads to the decrease with the third power of the principal quantum number expected from the hydrogenlike model.

the principal quantum numbers of the coupled states differ. This also leads to a small but significant deviation from the n^{-3} behavior.

We illustrate the effects of the different factors in Fig. 3.4(b). We find that only if both of the factors discussed above are corrected for does the n^{-3} behavior from the hydrogenlike model emerge again.

Interestingly, the removal of the green 1S state also has a significant effect on the absolute size of the splitting between ortho and paraexcitons in the range of principal quantum numbers shown, as can be seen in Fig. 3.4. The most important effect accounting for this is the level repulsion caused by the exchange interaction and V_d matrix elements between the green orthoexciton and the yellow Γ_5^+ states. The green Γ_5^+ exciton repels the yellow Γ_5^+ states, but the green Γ_4^+ and Γ_3^+ states leave the yellow paraexcitons of symmetry Γ_2^+ unaffected. For yellow states energetically higher than the green

1S state, this increases the splitting, whereas for those lower, it decreases it. The blue squares in Fig. 3.4 (a) show the splittings of the yellow excitons when this repulsion is removed. The resulting splittings in the yellow exciton series are far smaller than the experimental values for $n \geq 4$ and more in line with the values when the green 1S state is removed completely, as can be seen by comparison with the red circles. For the yellow 1S state, the effect is reversed and the removal of the level repulsion increases the splitting instead.

3.5 Splitting of yellow 1S state vs green 1S state

We conclude this chapter by investigating the difference in the strength between the exchange splitting of the green 1S state as compared to the yellow 1S state. We want to explain why the splitting of the green states is more than double that of the yellow states.

Diagonalizing the yellow series alone without the green $J = 3/2$ basis states, we find that the splitting of the yellow 1S excitons is approximately 7.02 meV, which is even smaller than with the full basis. Diagonalizing the green states alone, the splitting of the green 1S excitons is approximately 27.07 meV. The discrepancy can therefore not be explained by the mutual level shifts between the green 1S state and the yellow spectrum.

We again find that there are two factors which actually explain this difference. The first factor is the fact that the eigenvalues of the operator $\mathbf{S}_e \cdot \mathbf{S}_h$ differ between the $J = 1/2$ and $J = 3/2$ Hilbert space. According to the appendix of Ref. [38], the matrix elements in the basis (2.29) are given by

$$\begin{aligned}
 M = \langle \Pi' | \mathbf{S}_e \cdot \mathbf{S}_h \delta(\mathbf{r}) | \Pi \rangle &= \delta_{L'0} \delta_{L0} \delta_{F_t F'_t} \delta_{M_{F_t} M'_{F_t}} \frac{3}{2\pi} (-1)^{F_t + F' + F + J + J'} \quad (3.5) \\
 &\times [(2F + 1)(2F' + 1)(2J + 1)(2J' + 1)]^{\frac{1}{2}} \\
 &\times \begin{Bmatrix} F' & F & 1 \\ \frac{1}{2} & \frac{1}{2} & F_t \end{Bmatrix} \begin{Bmatrix} F & F' & 1 \\ J' & J & 0 \end{Bmatrix} \begin{Bmatrix} \frac{1}{2} & J' & 1 \\ J & \frac{1}{2} & 1 \end{Bmatrix}.
 \end{aligned}$$

Fixing either $J = J' = 1/2$ or $J = J' = 3/2$, the operator is already diagonal in the given basis. We can evaluate the matrix elements for the yellow and green series and $L = L' = 0$. For $J = J' = 1/2$, we calculate $M = 1/4\pi$ with $F_t = 0$ and $M = -1/12\pi$ with $F_t = 1$. For $J = J' = 3/2$ it is $M = 1/4\pi$ when $F_t = 2$ and $M = -5/12\pi$ when $F_t = 1$. Note that the exchange interaction (2.11) contains this operator with reversed sign. The exchange interaction therefore lifts the $F_t = 1$ states above the others in both the yellow and green series as depicted in Fig. 3.1. We thus find that the splitting in the

Table 3.1.: Energies of the lowest yellow and green 1S excitons for different choices of the parameters in the central-cell corrections with the exchange interaction removed. For the yellow values, we only diagonalized the $J = 1/2$ Hilbert space, and for the green values only the $J = 3/2$ Hilbert space. For the gap energies we used $E_{\text{gap,yellow}} = 2.17208 \text{ eV}$ and $E_{\text{gap,green}} = 2.30308 \text{ eV}$.

series	V_d	V^H	$E_{1S} [\text{eV}]$	$E_{\text{Ryd}} [\text{meV}]$
yellow	on	on	2.059	112.8
yellow	on	off	2.076	95.9
yellow	off	off	2.086	86.1
green	on	on	2.153	150.5
green	on	off	2.179	124.1
green	off	off	2.198	105.3

eigenvalues for $J = 3/2$ is $\Delta M_{\text{green}} = 2/3\pi$ and consequently exactly double the splitting for $J = 1/2$, which is $\Delta M_{\text{yellow}} = 1/3\pi$.

These calculations account for part of the difference between the yellow and green splitting. A factor of approximately 1.93 between the green and yellow splitting remains to be explained. Because of the δ term, the exchange splitting is proportional to $|\psi(0)|^2$, which in turn is proportional to the inverse third power of the Bohr radius a_B^{-3} . Since the Bohr radius is proportional to the reduced mass μ , it follows that $|\psi(0)|^2 \sim \mu^3$. This seems to be the reason for the factor 1.93, as explained in the following. The reduced mass is proportional to the Rydberg energy in a hydrogenlike system. To approximate the latter, we calculated the binding energy of the yellow and green 1S states while varying the exact form of the potential. The results are listed in Table 3.1. Based on these data, we can estimate the ratio of the reduced masses of the green and yellow 1S states with the ratio of the binding energies. Since the latter are not only affected by the Coulomb interaction, but also by the additional terms V^H and V_d in Eq. (2.12), we need to correct for those. Using the values where the central-cell corrections are removed completely, we get

$$\left(\frac{\mu_{\text{green}}}{\mu_{\text{yellow}}}\right)^3 \approx \left(\frac{E_{\text{Ryd}}^{\text{green}}}{E_{\text{Ryd}}^{\text{yellow}}}\right)^3 \approx \left(\frac{105.3 \text{ meV}}{86.1 \text{ meV}}\right)^3 \approx 1.22^3 \approx 1.82. \quad (3.6)$$

This is in good agreement with the factor of 1.93. The explanation for the different strengths of the exchange splitting in the yellow and green 1S exciton states therefore is on the one hand the factor two due to the operator $\mathbf{S}_e \cdot \mathbf{S}_h$ for $J = 1/2$ and $J = 3/2$ and on the other hand the difference in the reduced mass μ for the yellow and green 1S exciton.

4

Analysis of the fine structure of the D-exciton shell

In Chapter 3, we saw how the interplay between the yellow and green series can lead to unexpected effects, like reversing the order of the ortho-para pairs. In this chapter, we investigate another feature of the yellow exciton spectrum at the intersection of the exchange splitting and the yellow-green interaction. High resolution spectroscopy of the yellow D excitons in cuprous oxide reveal a pronounced splitting with one state being pushed above all other states of a given n -multiplet. This can be understood in the context of the reduced symmetry in the crystal environment and a strong mixing with the 1S exciton of the green series, as the theory developed by Schweiner *et al.* in Ref. [38] and the numerical calculations presented therein indicate. Here, we give a detailed analysis of the splitting of the yellow D excitons on the basis of theoretical considerations and experimental data, leading to a deeper understanding of the origin of the green admixtures to the yellow states as well as a revision of the assignment of approximate quantum numbers given in earlier studies such as by Uihlein *et al.* in Ref. [60]. The presented results have been published in Ref. [113]. In this chapter, we will first present the experimentally observed features of the fine structure we want to study in Sec. 4.1. We discuss the influence of the different terms of the Hamiltonian on the level splitting in Sec. 4.2, before analyzing the influence of the coupling to the green series in detail in Sec. 4.3. In Sec. 4.4, we extend the understanding of the energetic positions of the D excitons gained in the earlier sections to higher principal quantum numbers.

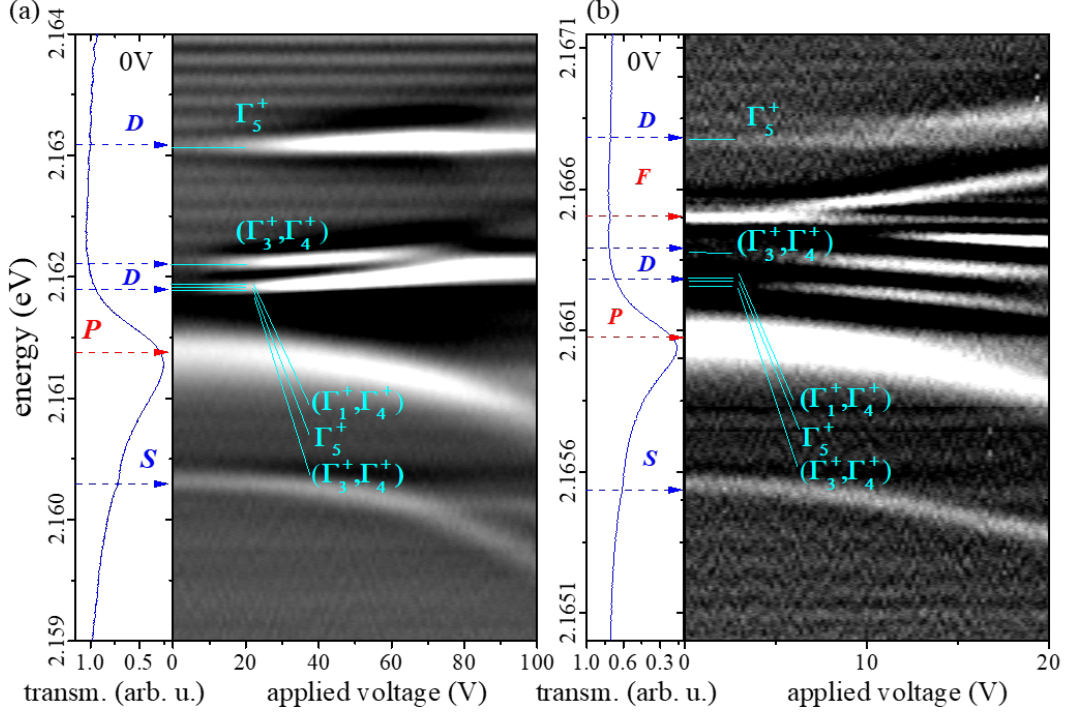


Figure 4.1.: Contour plots of second derivatives of experimental transmission spectra for the $n = 3$ exciton (a) and the $n = 4$ exciton (b) with an applied electric field. The corresponding spectrum without applied field is shown on the left, with the associated angular momenta labels in blue for even parity states and red for odd parity states. Numerically calculated energies are marked in cyan together with the associated irreducible representations, which are shifted by $-237 \mu\text{eV}$ for the $n = 3$ spectrum and $-218 \mu\text{eV}$ for the $n = 4$ spectrum. Taken from Ref. [113].

4.1 Experimentally observed structure of the n -multiplets

We begin by presenting the experimentally observed fine structure splitting for $n = 3$ and $n = 4$ in Fig. 4.1, the even parity states being made accessible by applying an external electric field. This leads to a mixing with the OPA allowed P and F states. The experimental data is shown as gray scale, with the numerically calculated positions of excitons superimposed. The latter are shifted as described in the caption. The resulting assignment of states differs from the one given in Ref. [38]. The experimental data was

obtained by M. Bayer's experimental group at TU Dortmund University [113].

The numerical calculation (cf. also Table 4.1) predicts five different D exciton levels, three of which are almost degenerate. The experiment reveals such a structure, with the three lowest levels remaining unresolved. In both multiplets $n = 3$ and $n = 4$ we observe a striking splitting between the D states with the representations (Γ_3^+, Γ_4^+) and Γ_5^+ . This splitting is of the same type as the ortho-para splitting of S states, which is why we will use the same nomenclature as in the latter case, and refer to the (Γ_3^+, Γ_4^+) states as parastates and to the Γ_5^+ states as orthostates. The magnitude of the splitting of the D states is comparable to the case of the S states, notwithstanding that the exchange splitting scales with the S admixture. To explain this surprising feature, we need to take a close look at the spectral structure of the yellow and green excitons in connection with the different terms of the Hamiltonian. The admixture of the green 1S state turns out to be central to a thorough understanding of the D exciton fine structure.

4.2 Separating the Hamiltonian according to symmetry

We want to understand how the observed fine-structure of the excitons follows from the terms of the Hamiltonian with increasingly reduced symmetry. The discussed separation of terms is closely reflected in the presentation in Fig. 4.2. The Hamiltonian (2.2) can be rewritten as in Refs. [35, 38],

$$H = E_g + \frac{\gamma'_1 \mathbf{p}^2}{2m_0} - \frac{e^2}{4\pi\epsilon_0\epsilon r} + H_{\text{SO}} + H_d + V_{\text{CCC}}, \quad (4.1)$$

with the relative momentum \mathbf{p} of electron and hole. The parameter γ'_1 determines the reduced mass of the system m_0/γ'_1 , where m_0 is the electron mass in vacuum. The band gap energy E_g is needed to lift the electron from the Γ_7^+ valence band to the Γ_6^+ conduction band. The parabolic kinetic energy term together with the screened Coulomb interaction with dielectric constant ϵ and the spin orbit interaction term H_{SO} form the hydrogenlike part of the Hamiltonian,

$$H_{\text{Hyd}} = E_g + \frac{\gamma'_1 \mathbf{p}^2}{2m_0} - \frac{e^2}{4\pi\epsilon_0\epsilon r} + H_{\text{SO}}. \quad (4.2)$$

The resulting spectrum consists of two independent hydrogenlike exciton series, i.e., the yellow and green series, which are characterized by the effective hole spin $J = 1/2$ and $J = 3/2$ respectively.

This simple picture is modified by the influence of the H_d terms originating from the nonparabolicity of the valence bands and the central-cell corrections V_{CCC} , which describe corrections for small electron-hole separations. The H_d terms can be separated into a

4. Analysis of the fine structure of the D-exciton shell

Table 4.1.: Numerically calculated exciton energies of the yellow $n = 3$ and $n = 4$ states for the different contributions to the Hamiltonian as discussed in relation to Eq. (4.1). We use the Haken potential, all values are in eV. We additionally show the values for the green 1S excitons. In the first column, we give the principal quantum number and angular momentum of the states, which we supplement by the associated irreducible representation in the second column. In the third column, we give the value of the angular momentum F according to the dominant contribution as presented in the last four columns. The seventh column shows the calculated green admixture.

nL	state Γ_i^\pm	F	energy [eV]			green adm. [%]	F [%]			
			$H_{\text{Hyd}} + H_d^s + H_\epsilon$	$+H_d^c$	$+H_{\text{exch}}$		1/2	3/2	5/2	7/2
1S _g	Γ_3^+, Γ_4^+	3/2	2.187237	2.118795	2.118795					
1S _g	Γ_5^+	3/2	2.187237	2.118795	2.154169					
3S	Γ_2^+	1/2	2.161730	2.159587	2.159587	0.5	99.5	0.0	0.0	0.5
3S	Γ_5^+	1/2	2.161730	2.159587	2.160714	4.2	71.7	5.1	22.5	0.6
3D	Γ_3^+, Γ_4^+	3/2	2.162462	2.162121	2.162121	0.3	0.0	96.6	3.1	0.1
3D	Γ_5^+	3/2	2.162462	2.162121	2.162150	0.3	0.2	96.1	3.5	0.0
3D	Γ_1^+, Γ_4^+	5/2	2.162485	2.162170	2.162170	0.3	0.0	0.0	99.8	0.1
3D	Γ_3^+, Γ_4^+	5/2	2.162485	2.162332	2.162332	0.4	0.0	3.4	96.5	0.0
3D	Γ_5^+	5/2	2.162485	2.162332	2.163286	7.0	19.1	8.4	72.0	0.4
3P	Γ_8^-	3/2	2.162361	2.161156	2.161156	1.0	0.0	98.9	0.7	0.1
3P	Γ_7^-	1/2	2.162353	2.161388	2.161388	0.7	99.3	0.0	0.0	0.1
4S	Γ_2^+	1/2	2.166379	2.165461	2.165461	0.2	99.8	0.0	0.0	0.2
4S	Γ_5^+	1/2	2.166379	2.165461	2.165834	1.4	80.1	2.5	17.0	0.3
4D	Γ_3^+, Γ_4^+	3/2	2.166668	2.166460	2.166460	0.2	0.0	96.0	3.8	0.0
4D	Γ_5^+	3/2	2.166668	2.166460	2.166478	0.2	0.3	96.7	2.8	0.0
4D	Γ_1^+, Γ_4^+	5/2	2.166684	2.168491	2.166490	0.2	0.0	0.0	99.9	0.1
4D	Γ_3^+, Γ_4^+	5/2	2.166684	2.166584	2.166584	0.2	0.0	4.0	96.0	0.0
4D	Γ_5^+	5/2	2.166684	2.166584	2.166991	3.0	17.4	4.3	78.0	0.2
4P	Γ_8^-	3/2	2.166633	2.166046	2.166046	0.5	0.0	99.4	0.4	0.1
4P	Γ_7^-	1/2	2.166630	2.166154	2.166154	0.3	99.5	0.0	0.0	0.2
4F	Γ_7^-	7/2	2.166696	2.166560	2.166560	0.1	0.2	0.0	0.0	99.8
4F	Γ_8^-	7/2	2.166696	2.166570	2.166570	0.1	0.0	0.1	45.9	54.0
4F	Γ_8^-	5/2	2.166696	2.166594	2.166594	0.1	0.0	0.0	54.0	45.9
4F	Γ_6^-	7/2	2.166696	2.166598	2.166598	0.1	0.0	0.0	48.1	51.9
4F	Γ_6^-	5/2	2.166696	2.166628	2.166628	0.1	0.0	0.0	51.9	48.1

spherical and a cubic part, $H_d = H_d^s + H_d^c$. Similarly, the central-cell corrections consist of two parts, namely corrections to the dielectric constant for small excitons, that is primarily the Haken or Pollman-Büttner potential, and the exchange interaction, which leads to a characteristic splitting between ortho- and parastates, $V_{CCC} = H_\epsilon + H_{\text{exch}}$.

The spherically symmetric description of the excitons is obtained by supplementing Eq. (4.2) with the spherical band structure term and the modifications to the dielectric constant,

$$H = H_{\text{Hyd}} + H_d^s + H_\epsilon. \quad (4.3)$$

For this Hamiltonian, the sum of angular momenta $\mathbf{F} = \mathbf{L} + \mathbf{J}$ remains a good quantum number. Accordingly, the states are labeled by L_F in this approximation. Note that the quantum number F for this angular momentum is not to be confused with the notation for states with $L = 3$ envelope, which we call F states. Which of these is meant follows from the context.

In the left column of Figure 4.2, we show the splitting for the spherical part of the Hamiltonian. Since the system is spherically symmetric but not hydrogenlike, the angular momentum F is a good quantum number, but the states belonging to the same principal quantum number are not necessarily degenerate. Nevertheless, states belonging to the same L are almost degenerate and we can use a quantum defect model, i.e., $E = -E_{\text{Ryd}}/(n - \delta_L)^2$ with the L -dependent quantum defect δ_L . The behavior of the quantum defects was investigated in Ref. [34].

Next, we consider the cubic H_d^c term, that reduces the spherical symmetry of the Hamiltonian to the cubic symmetry O_h and only the irreducible representations Γ_i^\pm remain as exact labels of the states, leading to a further splitting. The resulting level structure is depicted in the middle column of Figure 4.2. Due to the cubic contribution, the order of P states is flipped according to their total angular momenta F . The optically inactive $P_{1/2}$ state is shifted above the optically active $P_{3/2}$. On the other hand, the order of even parity states by increasing F from lower to higher energies is conserved. Note, the description given in Uihlein et al. [60] resulted in a reversed order of $D_{5/2}$ and $D_{3/2}$ excitons with the $D_{3/2}$ being the highest state. In their model, the parameter controlling the strength of the spherical valance band term has the value $\mu = 0.47$, while the cubic terms are neglected, $\delta = 0$. As discussed in Ref. [35], a fit of the material parameters to band structure calculations [34, 78] instead leads to the values $\mu = 0.0586$ and $\delta = -0.404$. The discussion in this chapter is based on the latter values. We thus find that the contribution of the cubic terms to the splitting of states is much more pronounced than indicated in Ref. [60], while the spherical H_d^s term is less important. Accordingly, the assignment of the angular quantum number F has to be changed in the case of the D states, compared to Ref. [60]. We will discuss this in greater detail below.

Finally, the exchange interaction is added. It requires the additional consideration of the electron spin. Therefore, the magnetic quantum number of the electron M_{S_e} ceases to be a good quantum number. The total angular momentum of the exciton $\mathbf{F}_t = \mathbf{F} + \mathbf{S}_e$ now characterizes the states as an approximate quantum number. The resulting splitting

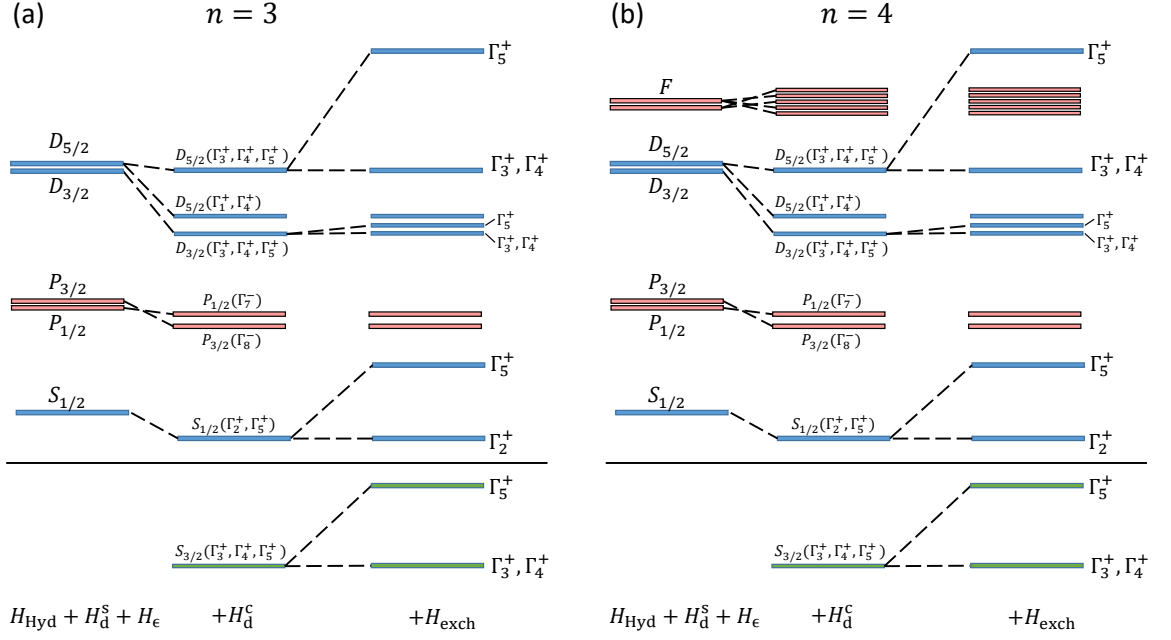


Figure 4.2.: Schematic illustration of the level splitting pattern of the $n = 3$ (a) and $n = 4$ (b) multiplets, first for the spherical part of the Hamiltonian $H_{\text{Hyd}} + H_{\text{d}}^{\text{s}} + H_{\epsilon}$ (left column), then adding the cubic band structure term H_{d}^{c} (middle column) and finally including the exchange interaction H_{exch} for the full Hamiltonian (right column). Odd parity and even parity states of the yellow series are depicted in red and blue color respectively. In the lower part, we additionally show the green 1S states in green. The presented level ordering is based on the numerical values in Table 4.1 and a comparison with experiment data as shown in Figure 4.1. Taken from Ref. [113].

pattern is shown in the right column for $n = 3$ and $n = 4$ respectively in Fig. 4.2.

4.3 Coupling to the green series

Central to the understanding of the behavior of the yellow D exciton lines is the admixture of the green 1S state. It can be understood now by analyzing the total angular momentum F without electron spin of the involved states. As mentioned above, an earlier analysis was given in Ref. [60], where the strong mixing of the energetically highest D exciton with the green 1S exciton compared to all other states within a multiplet was related to the spherical band structure terms. For excitons of the green series, one finds

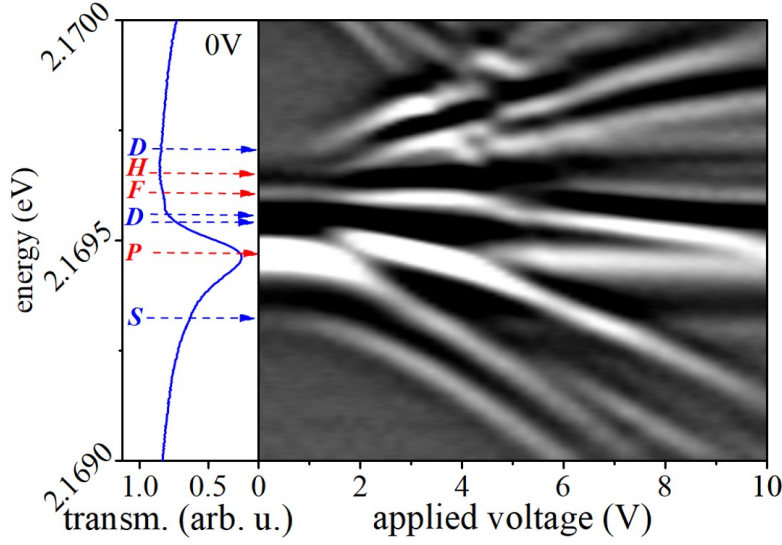


Figure 4.3.: Second derivative of experimental transmission spectra as a function of the applied external field for the $n = 6$ exciton states. For reference, the left side shows a spectrum at vanishing field. Red labels denote odd parity states, blue labels even parity states. The application of the electric field reveals that the $D_{5/2}(\Gamma_5^+)$ orthoexciton lies energetically above the H excitons. Taken from Ref. [113].

$J = 3/2$ and in particular $F = 3/2$ for the green $1S_{3/2}$ exciton. Since the spherical terms preserve F , the $D_{3/2}$ excitons are the only candidates that are mixed with the green $1S_{3/2}$ exciton already by the spherical part of the Hamiltonian (Eq. (4.3)), explaining their large amount of green content in the description given in Ref. [60]. Accordingly, the $D_{5/2}$ excitons have a lower content of green $1S_{3/2}$ in that model and the level repulsion between the green $1S_{3/2}$ state and the $D_{3/2}$ states then lifts the latter above the $D_{5/2}$ states.

However, as indicated in the discussion of the Hamiltonian further above, the actual material parameters of Cu_2O lead to a much weaker spherical H_d^s term [35] and a much more important cubic H_d^c term as assumed in Ref. [60]. We can understand how this changes the picture as explained in the following. Let Π' denote the quantum numbers of the green $1S_{3/2}$ state, such as $L' = 0$, $J' = 3/2$ and $F' = 3/2$ and Π the quantum numbers of a state from the yellow series such as L , $J = 1/2$ and F . The matrix elements belonging to the dominant cubic H_d term were presented in Ref. [35]. The derived expression depends upon a certain Wigner $9j$ -symbol [75] as follows,

$$\langle \Pi' | [P^{(2)} \times I^{(2)}]_q^{(4)} | \Pi \rangle = A_{\Pi', \Pi, q} \left\{ \begin{array}{ccc} L' & L & 2 \\ J' & J & 2 \\ F' & F & 4 \end{array} \right\}, \quad (4.4)$$

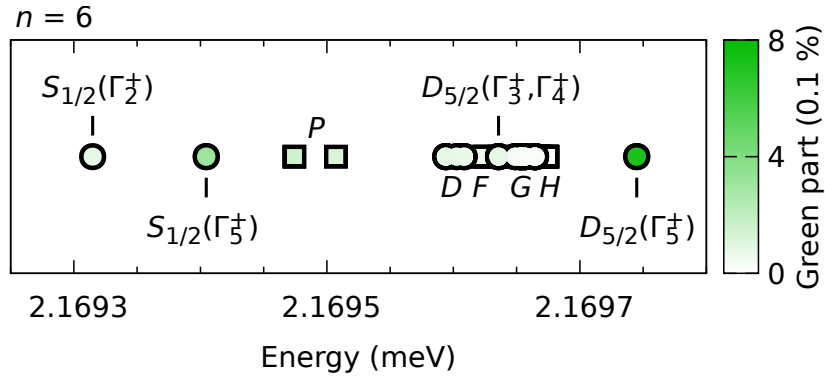


Figure 4.4.: Exciton energies for $n = 6$ states numerically calculated using the Haken potential. The admixture of green 1S is indicated by the color. We observe that the $D_{5/2}(\Gamma_5^+)$ exciton is shifted to a higher energy than the H excitons.

where $A_{\Pi', \Pi, q}$ is an abbreviation for the part of the formula we are not interested in for our discussion. The parameter q controls the behavior under rotations, and is not important here. The angular momenta and spins appearing in the $9j$ -symbols must fulfill certain selection rules, otherwise the matrix element vanishes. One of the conditions is that the angular momenta in each row satisfy the triangular inequalities of angular momentum coupling. From the second row we can thus deduce that the matrix element vanishes for $J' = J = 1/2$. The effect of the cubic terms on the yellow series thus crucially depends upon the coupling to the green series. The green 1S state has $L' = 0$ and $F' = 3/2$. From the first and third row, we can then conclude that it can only directly be coupled to states with $L = 2$ and $F \geq 5/2$, i.e. to the $D_{5/2}$ excitons. For any other yellow state, and in particular for the $D_{3/2}$ states, the matrix element vanishes. As a consequence, the level repulsion from the green 1S caused by the cubic terms most strongly affects the $D_{5/2}$ lines, lifting them above the $D_{3/2}$ lines. This is also consistent with the $\Gamma_{1/4}^+$ $D_{5/2}$ exciton staying energetically very close to the $D_{3/2}$ lines, since it cannot be repelled by the green states of different irreducible representation. This understanding of the energetic order of the states with different F values is corroborated by the numerically calculated F admixtures presented in Table 4.1, which are calculated analogously to the green admixtures.

4.4 Extension to principal quantum number $n \geq 6$

In the final section of this chapter, we want to generalize the findings of the preceding section to higher principal quantum numbers. In particular, we show that even for $n = 6$

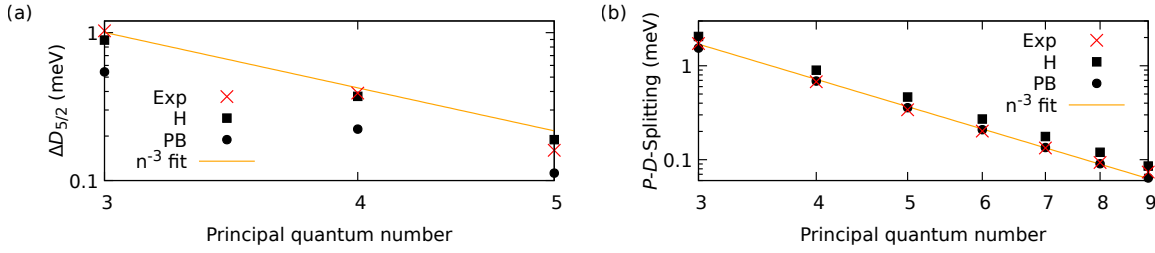


Figure 4.5.: (a) Splitting between the $D_{5/2}$ ortho- and paraexcitons as a function of the principal quantum number. (b) Splitting between the $D_{5/2}(\Gamma_5^+)$ orthostate and the dipole-allowed $P_{3/2}$ exciton as a function of the principal quantum number. Red crosses mark experimental data, numerical data calculated with the Haken potential is marked as black squares, numerical data calculated with the Pollmann-Büttner potential is marked as black circles. We additionally show a n^{-3} fit to the experimental data in yellow.

the ortho D state is still the highest state of the multiplet. We present data showing the n^{-3} scaling behavior of the exchange splitting of the D excitons. Since the other terms in the Hamiltonian causing the fine structure also scale as n^{-3} , we thus expect that the split off Γ_5^+ D exciton is the highest state even for large n .

In Fig. 4.3 we show experimental data of the $n = 6$ multiplet as a contour plot, similar to Fig. 4.1. We observe that the $D_{5/2}(\Gamma_5^+)$ states lie above the H states. This is corroborated by the numerical exciton positions presented in Fig. 4.4, which show the same behavior. The color scale used underlines the close connection between the level shifts and the green admixture.

To generalize this finding to higher quantum numbers we investigate the scaling law of the exchange splitting of the $D_{5/2}$ state in Fig. 4.5. We compare experimental data with numerical calculations, the latter using either the Haken or the Pollmann-Büttner potential. We first of all find that the Haken potential more faithfully reproduces the ortho-para-splitting of the $D_{5/2}$ state as shown on the left side, whereas the Pollmann-Büttner potential gives a more accurate estimate of the splitting between the ortho $D_{5/2}$ state and the dipole-active $P_{3/2}$ exciton as shown on the right side. We additionally performed a n^{-3} fit to the experimental data, which is in good agreement with the observations. We can thus extrapolate with reasonable certainty that the ortho $D_{5/2}$ exciton has the highest energy in all n -multiplets even for high n . This concludes our study of the fine structure of the D excitons and their interaction with the green series.

In this chapter and in Chapter 3 before it, we studied features of the yellow exciton series going beyond the hydrogenlike model in the field-free case. We saw how the interaction with the green series leads to interesting effects. In Chapter 5, we will study the application of an external magnetic field. The response of the excitonic system to the field is also significantly altered as compared to an atomic system.

5

Magneto-Stark effect of yellow excitons

In the previous chapters, we studied the yellow exciton series without external fields. Now we introduce a magnetic field into the description. As will be discussed in Sec. 5.1, this leads to the distinction between the Faraday and Voigt configuration. Here, we investigate and compare experimental and numerical excitonic spectra of the yellow series in cuprous oxide Cu_2O in the Voigt configuration and thus partially extend the results from Schweiner *et al.* [65], who only considered the Faraday configuration. The main difference between the configurations is given by an additional effective electric field in the Voigt configuration, caused by the motion of the exciton through the magnetic field. This magneto-Stark effect was already postulated by Gross *et al.* and Thomas *et al.* in 1961 [114, 115]. Group theoretical considerations show that the field most of all significantly increases the number of allowed lines by decreasing the symmetry of the system. Our conclusion is supported by both the experimental and numerical data. This represents a significant departure from the situation known in atomic physics, where the difference between the experimental geometries is strongly suppressed due to the higher masses. This study is published in Ref. [110].

Electric and magnetic fields aid in the investigation of quantum mechanical systems by introducing characteristic modifications of energy spectra, breaking symmetries and lifting selection rules. For example, the symmetry of the hydrogen atom is reduced from spherical to cylindrical [116–118] by the application of an external field. Excitons, being bound states between negatively charged electrons and positively charged holes, can for many purposes be modelled with a hydrogenlike description [11, 119]. Recent experimental investigations [30, 33, 120] uncovered deviations stemming from the reduction of the spherical symmetry to the discrete cubic symmetry, which arises from the complex valence band structure [34, 35, 65, 121]. The reduced symmetry leads to an observable fine structure splitting, since the mixing with the dipole allowed P states makes the F and H excitons visible.

But even when disregarding the reduced symmetry in the crystal environment, the changed material parameters of the exciton in comparison to the hydrogen atom lead

to a change of the relative mass and the mass of the center-of-mass motion, the latter being a lot smaller for the exciton. Because of this, it has a much more pronounced center-of-mass motion when experimentally excited by a photon. The associated momentum vector therefore potentially breaks the isotropy of the system. When applying an external field, we thus have to distinguish between the Faraday and Voigt configuration. In the former, the field is applied along the optical axis of the exciting laser, in the latter it is applied orthogonally. We here present experimental and numerical spectra demonstrating a difference between these two geometries for an external magnetic field in the case of excitons in cuprous oxide. We trace the difference to the magneto-Stark effect [114, 115, 122]: The charges moving in the magnetic field experience a Lorentz force analogous to the effect of an effective electric field (5.1)

$$\mathcal{F}_{\text{MSE}} = \frac{\hbar}{M} (\mathbf{K} \times \mathbf{B}), \quad (5.1)$$

where M is the exciton center-of-mass, \mathbf{K} is the exciton wavevector and \mathbf{B} the magnetic field. The effect of this term depends on the relative orientation of \mathbf{K} and \mathbf{B} and thus on the experimental geometry. This constitutes a difference between excitons and atoms, since for atoms, no such difference is expected due to the more strongly suppressed center-of-mass motion. The magneto-Stark effect was introduced theoretically already in the 1960s [114, 115, 122, 123] but there have only been few clear demonstrations [124] of it.

We first give some theoretical and experimental preliminaries in Secs. 5.1 and 5.2 before comparing our simulated spectra with experimental data in Sec. 5.3.

5.1 Faraday and Voigt configuration, magneto-Stark effect

In the following, we will differentiate between two different relative orientations of the magnetic field to the optical axis of the incoming laser beam. In the Faraday configuration, both axes are aligned to be parallel, whereas in the Voigt configuration, they are orthogonal to each other. Generally, the exciting laser will transfer a finite momentum $\hbar\mathbf{K}$ onto the exciton. This center of mass momentum would have to be added in the terms for the kinetic energies. Even without a magnetic field, this leads to quite complicated formulas (cf. the expressions for the Hamiltonian in the supplemental material of Ref. [89]) which are further complicated by the minimal substitution. Since the effect of many of the arising terms is presumably negligible due to the smallness of K , we simplify the problem and only consider the leading term [36, 118]

$$H_{\text{MSE}} = \frac{\hbar e}{M} (\mathbf{K} \times \mathbf{B}) \cdot \mathbf{r} \quad (5.2)$$

which we add to our Hamiltonian (2.2) in our numerical calculations. This is the well-known motional Stark effect term of the hydrogen atom. This term has the same form as an effective external electric field (5.1) perpendicular to the plane spanned by the wavevector \mathbf{K} and the magnetic field vector \mathbf{B} . The significance of this term evidently depends on the used configuration.

For the Faraday configuration, the effective electrical field (5.1) vanishes. A previous investigation of Schweiner *et al.* [65] was thus conducted under the approximation of vanishing center-of-mass momentum. They report a complicated splitting pattern where the magnetic field lifts all degeneracies. For a magnetic field oriented along one of the high symmetry axes of the crystal, the symmetry of the exciton is reduced from O_h to C_{4h} . Still, some selection rules remain, and not all lines become dipole-allowed. Parity remains a good quantum number and since only states with an admixture of P states have nonvanishing oscillator strengths, only states with odd values of L contribute to the exciton spectrum.

In the Voigt configuration on the other hand, the excitons have a nonvanishing momentum perpendicular to the magnetic field and the magneto-Stark term has to be considered. For our calculations, we therefore include an electric field, the size of which is given by the wavevector $K_0 = 2.79 \times 10^7 \frac{1}{\text{m}}$ of the incident light and the magnetic field. This value is obtained by the condition, that the exciting laser has the appropriate energy to create an exciton in the energy range we consider,

$$\frac{\hbar c K_0}{\sqrt{\varepsilon_{b2}}} = E_g - \frac{E_{\text{Ryd}}}{n^2} \quad (5.3)$$

for $n = 5$ and with $\varepsilon_{b2} = 6.46$ [125] and $E_{\text{Ryd}} = 86 \text{ meV}$ [34]. Note that we here use the dielectric constant $\varepsilon_{b2} = 6.46$ in the high frequency limit to describe the refractive index of the incident light. Since the total mass M of the exciton is about three orders of magnitude smaller than for a hydrogen atom, this term will have a significant effect on the spectra, even more so if we consider that the region of high fields is shifted to much lower values for the exciton [65]. The term (5.2) breaks the inversion symmetry and parity ceases to be a good quantum number. While in the Faraday configuration only the dipole-allowed exciton states of odd angular momentum have been important, now also the states with even angular momentum need to be considered. Hence, we need to include the terms for the central-cell corrections with the Haken potential as given in Refs. [38, 89] in our treatment of the Voigt geometry to correctly take the coupling to the low lying S states into account.

5.2 Source of experimental data

The experimental data was obtained by M. Bayers experimental group at the TU Dortmund University.

Three different Cu_2O crystal slabs were investigated experimentally, with the crystal surface normal to the [001], [110] and [111] directions respectively. The samples were cooled to a temperature of 1.4 K. Using a superconducting split coil magnet, magnetic fields up to 7 T could be applied either in the Faraday configuration or in the Voigt configuration.

For the absorption measurement, a white light source was filtered with a double monochromator to the range of energies of interest. The exciting light was linearly polarized. After being transmitted, the light was again filtered by a second double monochromator and then detected using a liquid-nitrogen cooled charge coupled device camera with a resolution of approximately $10 \mu\text{eV}$.

5.3 Comparison of experimental and numerical data

The left of Figure 5.1 shows experimental spectra for $n = 4$ to $n = 7$ in Voigt configuration with polarization orthogonal and parallel to the magnetic field respectively. The spectra for the two cases show clear differences due to the different selection rules for different polarizations. We will show in Sec. 5.3.1 that all lines in principle become dipole allowed and can be excited by exactly one of the two polarizations shown here.

For the comparison between the Faraday and Voigt configuration we show in Fig. 5.1 on the right experimental spectra taken (c) in Voigt configuration and (d) in Faraday configuration with polarization orthogonal to the magnetic field respectively. The polarizations are chosen in such a way that the same selection rules would apply to both spectra in Fig. 5.1 without the magneto-Stark field on the right. Thus, the differences between them must be due to the different geometries. S lines are visible for both configurations. This can be attributed to quadrupole-allowed transitions in the case of the Faraday configuration [65]. For the Voigt configuration, these lines quickly fade away. This is a sign that the additional mixing from the electric field transfers quadrupole oscillator strength away from the S excitons. This effect is not reproduced in the numerical spectra since we only extracted dipole oscillator strengths. In general, the effective electric field lifts selection rules, revealing additional lines not visible in the Faraday configuration. This can for example clearly be seen for the $n = 5$ states.

In Fig. 5.2 we show a comparison between experimental and numerically obtained line positions for $n = 4$ and $n = 5$. To improve the presentation of areas with many densely lying lines that individually have very low oscillator strengths, numerical spectra are convoluted using a Gaussian function with a constant width of $13.6 \mu\text{eV}$. This value is of the same order of magnitude as the width of the sharpest lines visible in the experiment. While the position of the P and F lines is reproduced very well, noticeable disagreement is observed for the S lines and also the faint 4D line visible in Fig. 5.2 on the

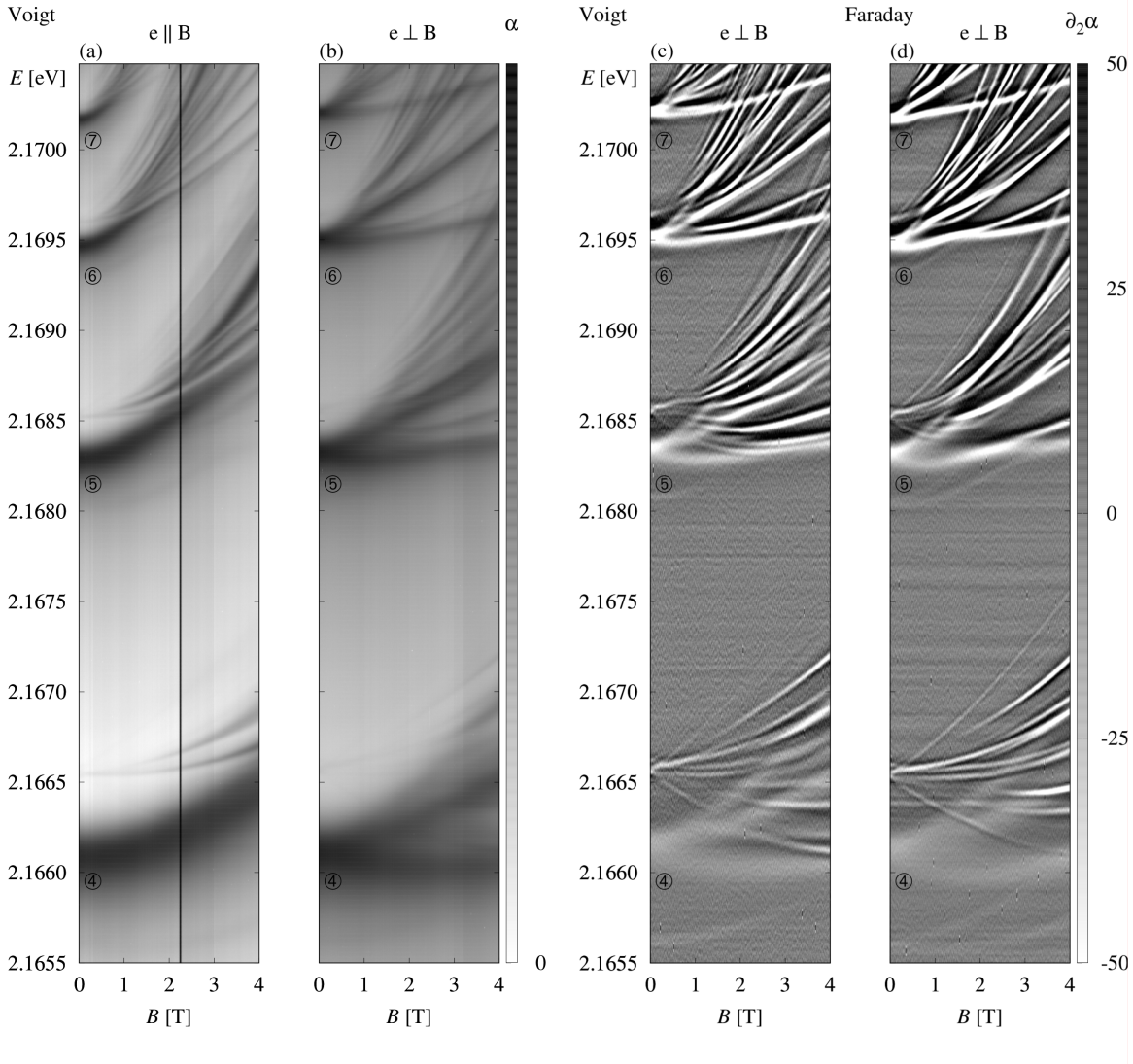


Figure 5.1.: *Left*: Experimental transmission spectra in arbitrary units for $n = 4$ to $n = 7$ taken in Voigt configuration for polarization (a) parallel [100] and (b) orthogonal [010] to the magnetic field. *Right*: Second derivative of experimental transmission spectra for $n = 4$ to $n = 7$ taken in (c) Voigt configuration and (d) Faraday configuration with polarization orthogonal [010] to the magnetic field. Data for the Faraday configuration were obtained by combining σ^+ - and σ^- -polarized spectra from Ref. [65] in an appropriate linear combination. We use the second derivative for better visibility of weak lines. Experimental data taken from Ref. [110].

right. Since our model is not explicitly constructed on a lattice [126], we have to include the central-cell corrections as an approximation into our Hamiltonian. As the central-

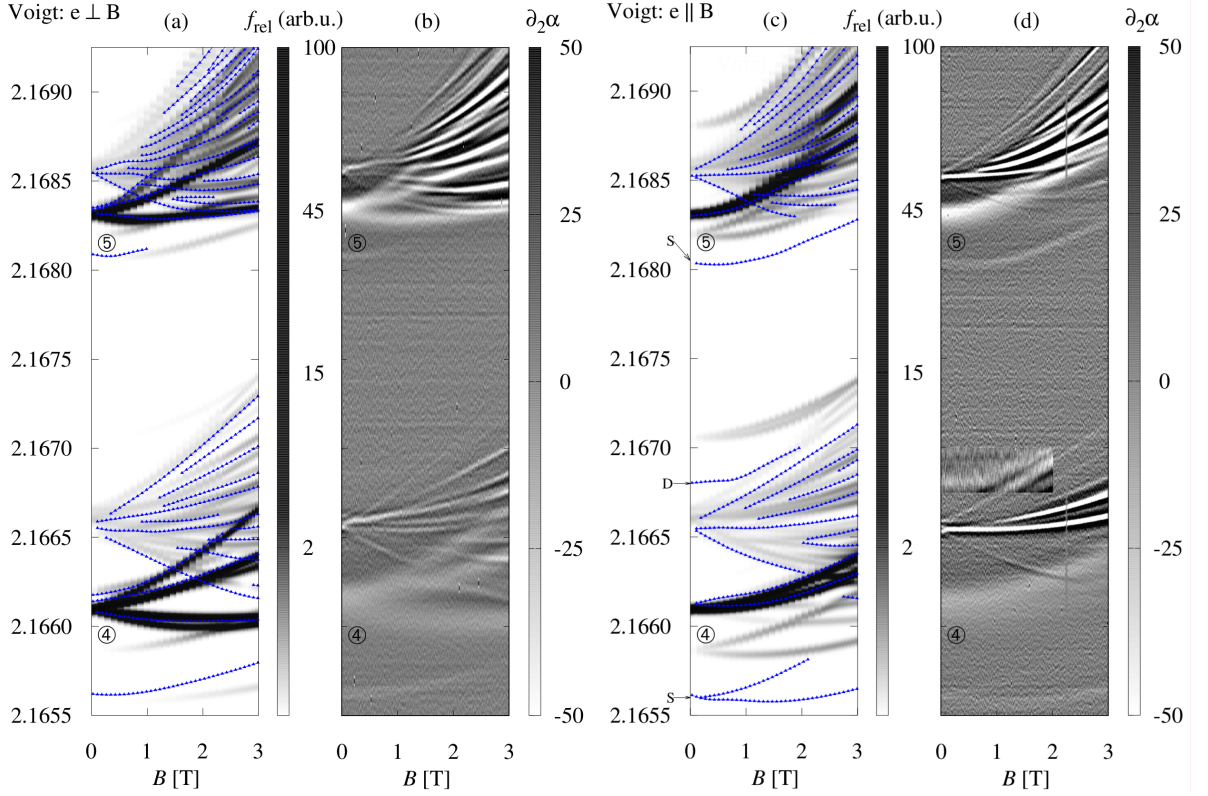


Figure 5.2.: *Left*: Comparison between numerical and experimental line positions for the Voigt configuration with light polarized orthogonally [010] to the magnetic field. (a) Numerical data in grayscale with read out experimental line positions (blue triangles) and (b) experimental data using the second derivative to enhance visibility of weak lines. *Right*: Same as on the left, but with light polarized parallelly [100] to the magnetic field. We increase the visibility of the experimental 4D line by using a different filter width and higher contrast. Note that the resolution of the numerical data is not uniform for all field strengths. Experimental data taken from Ref. [110].

cell corrections influence the even parity states much more strongly than the odd parity states, the error involved in this is more pronounced for the former than for the latter. A similar effect can also be seen in the tables in Ref. [38]. To make additional comparison involving the oscillator strengths possible we also present in Fig. 5.3 (a) data with light linearly polarized orthogonally [010] to the magnetic field in Faraday configuration taken from Ref. [65] and in (b) and (c) spectra in the Voigt configuration with light polarized orthogonally [010] and parallelly [100] to the magnetic field axis, respectively, for the principal quantum numbers $n = 4$ and $n = 5$. The experimental absorption coefficients do not fall to zero far away from the peaks due to phonon background. We lowered the values with a constant shift to counteract this effect. Note that we investigate a

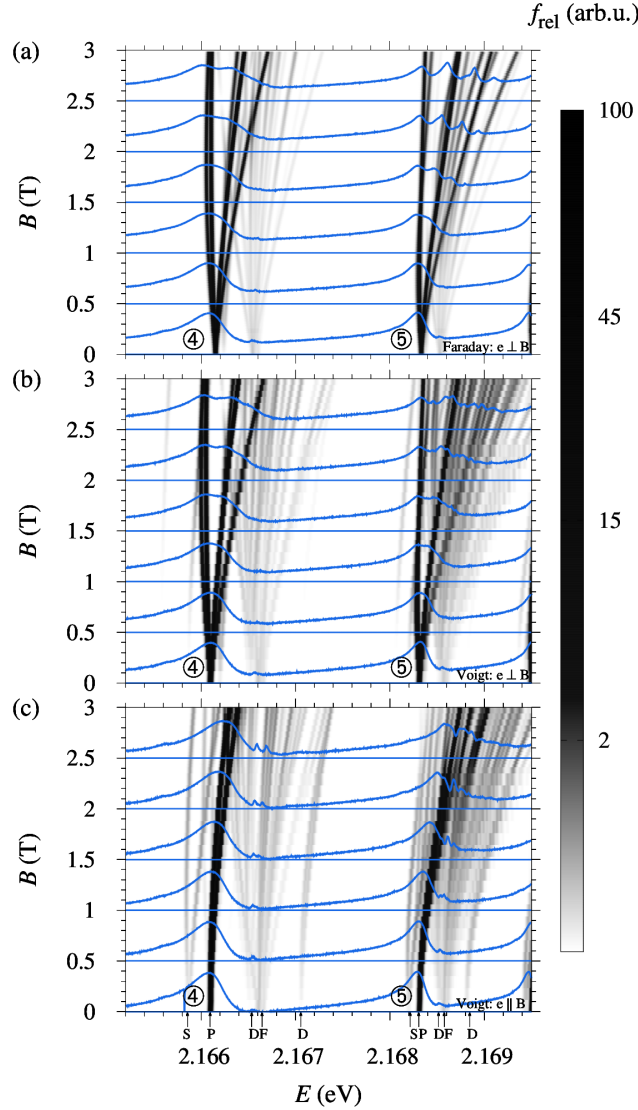


Figure 5.3.: Numerical and experimental spectra of the $n = 4$ and $n = 5$ excitons in an external magnetic field $\mathbf{B} \parallel [100]$. (a) Faraday configuration with light polarized along the $[010]$ direction. Data were obtained by combining σ^+ - and σ^- -polarized spectra from Ref. [65] in an appropriate linear combination. (b) and (c) Voigt configuration with a wavevector aligned with the $[001]$ direction and the light polarized (b) orthogonally $[010]$ and (c) parallelly $[100]$ to the magnetic field. Numerically calculated relative oscillator strengths are shown in grayscale. Experimentally measured absorption coefficients α are superimposed for a few selected values of B (blue solid lines). Note that the resolution of the numerical data is not uniform. We point out the theoretical visibility of S and D excitons as marked in (c).

parameter region where the effects of quantum chaos as discussed in Ref. [102] are not important.

In general, a good agreement between the experimental and numerical data sets is obtained. In the Voigt configuration in Figs. 5.2 and 5.3, a rich splitting is observed, especially of the F states of the $n = 5$ excitons. We see that light polarized orthogonally to the magnetic field probes complementary lines to the ones excited by light polarized in the direction of the field, a result that will also follow from our discussion below.

The experiment can not resolve the multiplicity of lines observed in the numerical simulation. This is because of the linewidths induced by the interaction with phonons and by radiative decay, which are not included in our theoretical description.

5.3.1 Influence of the magneto-Stark effect

We conclude this chapter by discussing the effects of the additional effective electric field on the line spectra in a group theoretical context. As we will see in the following derivations, the most pronounced effect is a significant increase in the number of dipole-allowed lines due to the decreased symmetry with the electric field. Panels (a) and (b) in Fig. 5.3 show this quite clearly, especially for the large number of additional F lines and also G lines for $n = 5$ in the Voigt configuration. This is most obvious for the theoretical spectra, but can also distinctly be seen in the experiment for $n = 5$. Note that without the magneto-Stark effect the same selection rules would apply to the spectra in (a) and (b), but not in (c). In contrast to the Faraday configuration [65], we can not limit ourselves to the states with odd values for L , owing to the mixture of the even and odd series in the electric field. We discuss the case of a magnetic field aligned in [001] direction and will disregard the influence of the central-cell corrections in this discussion.

We consider the reduction of the irreducible representations \tilde{D}_F^\pm of the full rotation group in the presence of the crystal as well as the magnetic and effective electric field, where $F = J + L = (I + S_h) + L$ is the angular momentum without the electron spin. Here, the quasispin I and hole spin S_h are first coupled to the effective hole spin J and then combined with the orbital angular momentum L to form F . With this information we will be able to deduce the splitting of the lines due to the reduced symmetry [127]. Additionally we can compare the resulting irreducible representations with those that the dipole operator belongs to. This will tell us which lines are dipole-allowed and which are not. Note that the symmetry of the quasispin I in O_h is given by $\Gamma_5^+ = \Gamma_4^+ \otimes \Gamma_2^+$ [65] and therefore all irreducible representations have to be multiplied by Γ_2^+ in comparison with the case of an ordinary spin. Keeping this in mind, we have [76]

$$L = 0 : \\ \tilde{D}_{\frac{1}{2}}^+ = D_{\frac{1}{2}}^+ \otimes \Gamma_2^+ = \Gamma_6^+ \otimes \Gamma_2^+ = \Gamma_7^+, \quad (5.4a)$$

$L = 1 :$

$$\tilde{D}_{\frac{1}{2}}^- = D_{\frac{1}{2}}^- \otimes \Gamma_2^+ = \Gamma_6^- \otimes \Gamma_2^+ = \Gamma_7^-, \quad (5.4b)$$

$$\tilde{D}_{\frac{3}{2}}^- = D_{\frac{3}{2}}^- \otimes \Gamma_2^+ = \Gamma_8^- \otimes \Gamma_2^+ = \Gamma_8^-, \quad (5.4c)$$

$L = 2 :$

$$\tilde{D}_{\frac{3}{2}}^+ = D_{\frac{3}{2}}^+ \otimes \Gamma_2^+ = \Gamma_8^+ \otimes \Gamma_2^+ = \Gamma_8^+, \quad (5.4d)$$

$$\tilde{D}_{\frac{5}{2}}^+ = D_{\frac{5}{2}}^+ \otimes \Gamma_2^+ = (\Gamma_7^+ \oplus \Gamma_8^+) \otimes \Gamma_2^+ = \Gamma_6^+ \oplus \Gamma_8^+, \quad (5.4e)$$

$L = 3 :$

$$\tilde{D}_{\frac{5}{2}}^- = D_{\frac{5}{2}}^- \otimes \Gamma_2^+ = (\Gamma_7^- \oplus \Gamma_8^-) \otimes \Gamma_2^+ = \Gamma_6^- \oplus \Gamma_8^-, \quad (5.4f)$$

$$\tilde{D}_{\frac{7}{2}}^- = D_{\frac{7}{2}}^- \otimes \Gamma_2^+ = (\Gamma_6^- \oplus \Gamma_7^- \oplus \Gamma_8^-) \otimes \Gamma_2^+ = \Gamma_7^- \oplus \Gamma_6^- \oplus \Gamma_8^-, \quad (5.4g)$$

$L = 4 :$

$$\tilde{D}_{\frac{7}{2}}^+ = D_{\frac{7}{2}}^+ \otimes \Gamma_2^+ = (\Gamma_6^+ \oplus \Gamma_7^+ \oplus \Gamma_8^+) \otimes \Gamma_2^+ = \Gamma_7^+ \oplus \Gamma_6^+ \oplus \Gamma_8^+, \quad (5.4h)$$

$$\tilde{D}_{\frac{9}{2}}^+ = D_{\frac{9}{2}}^+ \otimes \Gamma_2^+ = (\Gamma_6^+ \oplus \Gamma_8^+ \oplus \Gamma_8^+) \otimes \Gamma_2^+ = \Gamma_7^+ \oplus \Gamma_8^+ \oplus \Gamma_8^+. \quad (5.4i)$$

We still need to include the spin of the electron which transforms according to Γ_6^+ . For vanishing magnetic field strengths, the representations belonging to an irreducible representation without the spin are degenerate. Those will be written in brackets. The reduction [76] will only be specified for even parity, since the odd case only changes the sign. We obtain

$$\tilde{D}_{\frac{1}{2}}^+ \otimes \Gamma_6^+ = (\Gamma_2^+ \oplus \Gamma_5^+), \quad (5.5a)$$

$$\tilde{D}_{\frac{3}{2}}^+ \otimes \Gamma_6^+ = (\Gamma_3^+ \oplus \Gamma_4^+ \oplus \Gamma_5^+), \quad (5.5b)$$

$$\tilde{D}_{\frac{5}{2}}^+ \otimes \Gamma_6^+ = (\Gamma_1^+ \oplus \Gamma_4^+) \oplus (\Gamma_3^+ \oplus \Gamma_4^+ \oplus \Gamma_5^+), \quad (5.5c)$$

$$\tilde{D}_{\frac{7}{2}}^+ \otimes \Gamma_6^+ = (\Gamma_2^+ \oplus \Gamma_5^+) \oplus (\Gamma_1^+ \oplus \Gamma_4^+) \oplus (\Gamma_3^+ \oplus \Gamma_4^+ \oplus \Gamma_5^+), \quad (5.5d)$$

$$\tilde{D}_{\frac{9}{2}}^+ \otimes \Gamma_6^+ = (\Gamma_2^+ \oplus \Gamma_5^+) \oplus (\Gamma_3^+ \oplus \Gamma_4^+ \oplus \Gamma_5^+) \oplus (\Gamma_3^+ \oplus \Gamma_4^+ \oplus \Gamma_5^+). \quad (5.5e)$$

Γ_1^+ and Γ_2^+ are one-dimensional, Γ_3^+ is two-dimensional, and Γ_4^+ and Γ_5^+ are three-dimensional. So without the field, we have for example fourfold degenerate S states and P states that are split into one fourfold and one eightfold degenerate line. If the magnetic field is switched on, the electric field becomes nonvanishing too. The symmetry is reduced from O_h to C_S [76]. All representations of C_S are one-dimensional, so all degeneracies will be lifted, just as in the case with only a magnetic field. But in contrast to the Faraday configuration, the symmetry is lowered even further, leading to a greater mixture of the states. In fact, all lines become dipole-allowed. To see this, we have to consider the reduction of the irreducible representations of O_h in C_S [76, 127]. The relevant expressions are

$$\begin{array}{ll} \Gamma_1^+ \rightarrow \Gamma_1, & \Gamma_1^- \rightarrow \Gamma_2, \\ \Gamma_2^+ \rightarrow \Gamma_1, & \Gamma_2^- \rightarrow \Gamma_2, \\ \Gamma_3^+ \rightarrow \Gamma_1 \oplus \Gamma_1, & \Gamma_3^- \rightarrow \Gamma_2 \oplus \Gamma_2, \\ \Gamma_4^+ \rightarrow \Gamma_1 \oplus \Gamma_2 \oplus \Gamma_2, & \Gamma_4^- \rightarrow \Gamma_2 \oplus \Gamma_1 \oplus \Gamma_1, \\ \Gamma_5^+ \rightarrow \Gamma_1 \oplus \Gamma_2 \oplus \Gamma_2, & \Gamma_5^- \rightarrow \Gamma_2 \oplus \Gamma_1 \oplus \Gamma_1. \end{array}$$

The dipole operator belongs to Γ_4^- in O_h [76] and its reduction therefore includes all appearing representations. Thus, all $4n^2$ lines receive nonvanishing oscillator strength, the only limitation being given by the polarization of the incident light, i.e., a given state can either be excited by radiation polarized in the z -direction (Γ_2) or by radiation polarized in the x - y -plane (Γ_1).

In this chapter, we introduced the magneto-Stark effect and the associated effective electric field. In Chapter 6, this will also play an important role in the process of second harmonic generation along forbidden directions in a magnetic field.

6

Second harmonic generation in magnetic fields

The application of external fields can reduce the symmetry of a system, leading to novel selection rules as explored in Chapter 5. Here, we will see how this affects the theory of Second Harmonic Generation (SHG). Recently SHG for the yellow exciton series in cuprous oxide has been demonstrated [64]. Assuming perfect O_h symmetry, SHG is forbidden along certain high-symmetry axes. Perturbations can break this symmetry and forbidden transitions may become allowed. We investigate theoretically the effect of external magnetic fields on the yellow exciton lines of cuprous oxide. We identify two mechanisms by which an applied magnetic field can induce a second harmonic signal in a forbidden direction. First of all, a magnetic field by itself generally lifts the selection rules. In the Voigt configuration, an additional magneto-Stark electric field appears. This also induces certain SHG processes differing from those induced by the magnetic field alone. Complementary to the manuscript by A. Farenbruch *et al.* [109], we perform a full numerical diagonalization of the exciton Hamiltonian including the complex valence band structure. Numerical results are compared with experimental data. Essential parts of this chapter are published in Ref. [111].

Due to the influence of the crystal symmetry and complex valence band structure, the exciton spectrum shows typical deviations from a hydrogen spectrum leading to an observable splitting and mixing between P and different F states [33]. Additionally, the symmetry of the bands also significantly affects the selection rules for different optical processes [30, 35, 65] such as one-photon and two-photon excitation.

After the first theoretical treatment of two-photon processes in 1931 [128], and their first experimental demonstration in the optical range in 1963 [129], nonlinear optical techniques have established themselves as useful methods for the study of electronic properties of solids [130, 131]. They complement linear tools due to different selection rules [132]. For example, in one-photon absorption spectroscopy in cuprous oxide the odd exciton states are excited, whereas in two-photon excitation, it is the even parity

states.

One example of a nonlinear optical process is Second Harmonic Generation (SHG). In SHG, two incoming photons are combined into one outgoing photon of double energy. Recently, Mund *et al.* have demonstrated SHG for the yellow exciton series in cuprous oxide [64]. Here, the spectrum consists mainly of the even parity excitons.

The symmetry induced selection rules determine which exciton states can participate in SHG processes. Additional limitations concerning the polarization and direction of the incoming and outgoing light exist. One important limitation is the existence of forbidden directions in the crystal, where SHG is not allowed due to symmetry reasons. There is a number of ways in which a SHG signal can nevertheless be induced along such a direction [133–137]. In general, a perturbation can break the crystal symmetry and lift this selection rule. One possibility of such a perturbation is strain in the crystal. Even without the application of an external strain, SHG has been observed for the yellow 1S orthoexciton in forbidden directions due to residual strain in the sample [138]. The excitons with higher principal quantum numbers remain forbidden, since the energetic splitting due to the strain does not exceed their linewidths and the selection rule thus is not lifted for them [138].

To observe the higher exciton states, a different method is required. Here, we investigate the application of an external magnetic field. For a discussion of the resulting SHG spectra, we have to differentiate the two experimental geometries as in Chapter 5. In Faraday configuration, the magnetic field is applied parallel to the wave vector of the incident light, whereas in Voigt configuration the two are perpendicular to each other. In the latter case, an additional term behaving like an effective electric field orthogonal to both the wave vector and the magnetic field appears, breaking the inversion symmetry of the crystal. This leads to a mixing of odd and even parity excitons [110] and thus to additional features in the SHG spectra. In Faraday configuration this effective electric field is absent.

The induced SHG spectra significantly depend on the choice of polarization of the incoming and outgoing light. In particular, these dependencies differ among the mechanisms inducing SHG and can therefore be used for their differentiation.

We focus on the diagonalization of the complete exciton Hamiltonian including the valence band structure and on the detailed comparison of numerical and experimental data for certain fixed choices of polarization in this chapter. The polarization dependencies of the SHG spectra in general are investigated more thoroughly in the manuscript by Farenbruch *et al.* [109], where SHG intensities are treated as a function of the linear polarization angles of incoming and outgoing light for certain fixed peaks. Additional mechanisms for the production of SHG light beyond those in the present chapter are considered as well.

In Sec. 6.1 we show how our calculated eigenvalues and eigenvectors can be used to simulate Second Harmonic Generation spectra and derive the selection rules in Sec. 6.2. We describe the experimental setup for SHG in Sec. 6.3. In 6.4, the numerical results are shown and compared with experimental spectra.

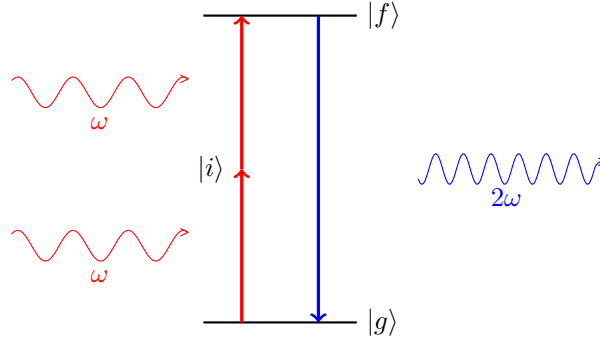


Figure 6.1.: Scheme of a Second Harmonic Generation process. The ground state of the crystal is denoted by $|g\rangle$, the resonantly stimulated exciton state by $|f\rangle$, and the virtual intermediate state by $|i\rangle$.

6.1 Second Harmonic Generation

Second Harmonic Generation is a process where two incoming photons are coherently transformed into one outgoing photon of doubled frequency as illustrated in Fig. 6.1. A given exciton state can only contribute to the SHG spectrum, if it is both two-photon and one-photon allowed. In the field-free case, only even exciton states can be excited in two-photon transition processes. Since these are dipole forbidden, SHG can only be obtained by the addition of a quadrupole emission process. There are two conditions that determine the selection rules for these processes: For the dominant contribution, the envelope wave function has to be nonvanishing at the origin [89, 132], which requires an $L = 0$ component, and the exciton state has to have an admixture of vanishing total spin $\mathbf{S} = \mathbf{S}_e + \mathbf{S}_h = 0$, since a spin flip is forbidden here. Only the Γ_5^+ excitons of even parity fulfill both conditions. This can be seen by considering the resulting set of angular momenta. With $L = 0$, $S = 0$ and $I = 1$, the rotational behavior for the exciton states is determined by the quasi-spin \mathbf{I} , which, as stated above, transforms according to Γ_5^+ . We see that in the tensor product [76]

$$\Gamma_4^- \otimes \Gamma_4^- = \Gamma_1^+ \oplus \Gamma_3^+ \oplus \Gamma_4^+ \oplus \Gamma_5^+ \quad (6.1)$$

belonging to both the two-photon (Γ_4^- for each incoming photon) and quadrupole operator (Γ_4^- for both the outgoing photon and the \mathbf{K} vector), only the Γ_5^+ term contributes in leading order.

6.1.1 Calculation of SHG intensities

To simulate the SHG intensity spectra for a given polarization of the outgoing light \mathbf{E}^{out} ,

$$I(2\omega) = \left| \sum_i E_i(2\omega) E_i^{\text{out}} \right|^2 \quad (6.2)$$

with

$$E_i(2\omega) \sim \sum_{j,k} \chi_{ijk}^{(2)} E_j(\omega) E_k(\omega), \quad (6.3)$$

we need to calculate the corresponding nonlinear susceptibilities

$$\chi_{f,lmn}^{(2)} \sim \sum_i \frac{\langle g | V_l^Q | f \rangle \langle f | V_m^D | i \rangle \langle i | V_n^D | g \rangle}{(E_f - 2\hbar\omega - i\Gamma_f)(E_i - \hbar\omega)}. \quad (6.4)$$

Here, D and Q mark terms belonging to the excitation by two dipole steps and to the quadrupole emission process, respectively. The states involved are denoted by $|g\rangle$ for the ground state of the crystal, $|f\rangle$ for the resonantly excited exciton state, and $|i\rangle$ for the virtual intermediate states. The conditions of vanishing total spin (admixture of $\mathbf{S} = 0$) and nonvanishing wave function at the origin (admixture of $\mathbf{L} = 0$) imply that the strength of both processes is given by the overlaps with the following states with irreducible representation Γ_5^+ [89]:

$$\begin{aligned} |\pi_{yz}^Q\rangle &= \frac{1}{\sqrt{2}} (|1, -1\rangle_Q - |1, 1\rangle_Q), \\ |\pi_{xz}^Q\rangle &= \frac{i}{\sqrt{2}} (|1, -1\rangle_Q + |1, 1\rangle_Q), \\ |\pi_{xy}^Q\rangle &= |1, 0\rangle_Q, \end{aligned} \quad (6.5)$$

with

$$\begin{aligned} |F_t, M_{F_t}\rangle_Q &= |S, I; I + S, L; F_t, M_{F_t}\rangle \\ &= |0, 1; 1, 0; 1, M_{F_t}\rangle. \end{aligned} \quad (6.6)$$

In Eq. (6.5), the quantization axis is chosen to be along the [001] direction. If [110] is chosen to be the z - and quantization axis, we instead have

$$\begin{aligned} |\pi_{yz}^Q\rangle &= \frac{i}{2} |1, -1\rangle_Q^{[110]} + \frac{i}{2} |1, 1\rangle_Q^{[110]} + \frac{1}{\sqrt{2}} |1, 0\rangle_Q^{[110]}, \\ |\pi_{xz}^Q\rangle &= -\frac{i}{2} |1, -1\rangle_Q^{[110]} - \frac{i}{2} |1, 1\rangle_Q^{[110]} + \frac{1}{\sqrt{2}} |1, 0\rangle_Q^{[110]}, \\ |\pi_{xy}^Q\rangle &= \frac{1}{\sqrt{2}} |1, -1\rangle_Q^{[110]} - \frac{1}{\sqrt{2}} |1, 1\rangle_Q^{[110]}. \end{aligned} \quad (6.7)$$

For the case of the quantization axis being parallel to the [111] direction, we obtain

$$\begin{aligned}
 |\pi_{yz}^Q\rangle &= \left(\frac{1}{2\sqrt{3}} - \frac{i}{2}\right) |1, -1\rangle_Q^{[111]} + \left(\frac{1}{2\sqrt{3}} + \frac{i}{2}\right) |1, 1\rangle_Q^{[111]} + \frac{1}{\sqrt{3}} |1, 0\rangle_Q^{[111]}, \\
 |\pi_{xz}^Q\rangle &= \left(\frac{1}{2\sqrt{3}} + \frac{i}{2}\right) |1, -1\rangle_Q^{[111]} - \left(\frac{1}{2\sqrt{3}} - \frac{i}{2}\right) |1, 1\rangle_Q^{[111]} + \frac{1}{\sqrt{3}} |1, 0\rangle_Q^{[111]}, \\
 |\pi_{xy}^Q\rangle &= -\frac{1}{\sqrt{3}} |1, -1\rangle_Q^{[111]} + \frac{1}{\sqrt{3}} |1, 1\rangle_Q^{[111]}.
 \end{aligned} \tag{6.8}$$

For the two-photon excitation, we have to consider the coupling of $\Gamma_4^- \otimes \Gamma_4^- \rightarrow \Gamma_5^+$ for the two polarization vectors of the incoming light. Here, we only consider the case of two identical incoming photons with polarization $\mathbf{E}^{\text{in}} = (E_1^{\text{in}}, E_2^{\text{in}}, E_3^{\text{in}})$. The coupling coefficients as given in [76] imply that the transition amplitudes for two-photon absorption with two dipole steps \mathbf{O}_{TPDD} can then be calculated using the symmetrical cross product

$$\mathbf{O}_{\text{TPDD}} \sim \mathbf{E}^{\text{in}} \otimes \mathbf{E}^{\text{in}} = \frac{1}{\sqrt{2}} \begin{pmatrix} E_2^{\text{in}} E_3^{\text{in}} + E_3^{\text{in}} E_2^{\text{in}} \\ E_3^{\text{in}} E_1^{\text{in}} + E_1^{\text{in}} E_3^{\text{in}} \\ E_1^{\text{in}} E_2^{\text{in}} + E_2^{\text{in}} E_1^{\text{in}} \end{pmatrix}, \tag{6.9}$$

where the components give the amplitude for the excitation of a state transforming as yz for \mathbf{e}_1 , as xz for \mathbf{e}_2 and as xy for \mathbf{e}_3 . We see that, for example, light polarized along the [110] direction will produce exciton states transforming according to the basis vector xy of Γ_5^+ .

For the quadrupole emission process, we similarly have to consider the coupling of the polarization vector \mathbf{E}^{out} of the outgoing light, determined by the analyzer in the experiment, and the wave vector \mathbf{K} ,

$$\mathbf{O}_Q \sim \mathbf{K} \otimes \mathbf{E}^{\text{out}} = \frac{1}{\sqrt{2}} \begin{pmatrix} K_2 E_3^{\text{out}} + E_3^{\text{out}} K_2 \\ K_3 E_1^{\text{out}} + E_1^{\text{out}} K_3 \\ K_1 E_2^{\text{out}} + E_2^{\text{out}} K_1 \end{pmatrix}. \tag{6.10}$$

Analogously to the case of two-photon excitation, we can, for example, conclude that light polarized along the [001] direction with a wave vector parallel to [100] can only be emitted by exciton states transforming as xz .

6.1.2 Dipole emission process

In Voigt configuration, considered in some of the spectra here, an effective electric field arises. This electric field breaks the inversion symmetry of the crystal and mixes states of different parity. This will also make certain SHG processes involving a dipole emission step allowed. Similarly to the case of the two-photon excitation and quadrupole emission

processes, the strength of these dipole emission processes are given by the overlaps with the three states of symmetry Γ_4^- as derived in Refs. [35, 65, 89]:

$$\begin{aligned} |\pi_x^D\rangle &= \frac{i}{\sqrt{2}} (|2, -1\rangle_D + |2, 1\rangle_D) , \\ |\pi_y^D\rangle &= \frac{1}{\sqrt{2}} (|2, -1\rangle_D - |2, 1\rangle_D) , \\ |\pi_z^D\rangle &= \frac{i}{\sqrt{2}} (|2, -2\rangle_D - |2, 2\rangle_D) , \end{aligned} \quad (6.11)$$

with

$$\begin{aligned} |F_t, M_{F_t}\rangle_D &= |S, I; I + S, L; F_t, M_{F_t}\rangle \\ &= |0, 1; 1, 1; F_t, M_{F_t}\rangle . \end{aligned} \quad (6.12)$$

Again, Eq. (6.11) gives the result with quantization axis along [001]. For [110], we get

$$\begin{aligned} |\pi_x^D\rangle &= -\frac{i}{2}|2, -2\rangle_D^{[110]} + \frac{1}{2}|2, -1\rangle_D^{[110]} - \frac{1}{2}|2, 1\rangle_D^{[110]} + \frac{i}{2}|2, 2\rangle_D^{[110]} , \\ |\pi_y^D\rangle &= \frac{i}{2}|2, -2\rangle_D^{[110]} + \frac{1}{2}|2, -1\rangle_D^{[110]} - \frac{1}{2}|2, 1\rangle_D^{[110]} - \frac{i}{2}|2, 2\rangle_D^{[110]} , \\ |\pi_z^D\rangle &= -\frac{1}{\sqrt{8}}|2, -2\rangle_D^{[110]} + \frac{\sqrt{3}}{2}|2, 0\rangle_D^{[110]} + \frac{1}{\sqrt{8}}|2, 2\rangle_D^{[110]} , \end{aligned} \quad (6.13)$$

and for the [111] direction

$$\begin{aligned} |\pi_x^D\rangle &= \left(\frac{1}{\sqrt{18}} - \frac{i}{6}\right) |2, -2\rangle_D^{[111]} + \left(\frac{1}{6} + \frac{i}{\sqrt{12}}\right) |2, -1\rangle_D^{[111]} \\ &\quad - \left(\frac{1}{6} + \frac{i}{\sqrt{12}}\right) |2, 1\rangle_D^{[111]} + \left(\frac{1}{\sqrt{18}} + \frac{i}{6}\right) |2, 2\rangle_D^{[111]} + \frac{1}{3}|2, 0\rangle_D^{[111]} , \\ |\pi_y^D\rangle &= \left(\frac{1}{6} - \frac{i}{\sqrt{12}}\right) |2, 1\rangle_D^{[111]} + \left(\frac{1}{\sqrt{18}} - \frac{i}{6}\right) |2, 2\rangle_D^{[111]} \\ &\quad + \left(\frac{1}{6} - \frac{i}{\sqrt{12}}\right) |2, -1\rangle_D^{[111]} + \left(\frac{1}{\sqrt{18}} + \frac{i}{6}\right) |2, -2\rangle_D^{[111]} + \frac{1}{3}|2, 0\rangle_D^{[111]} , \\ |\pi_z^D\rangle &= \frac{1}{\sqrt{3}}|2, 0\rangle_D^{[111]} + \frac{1}{3}|2, 1\rangle_D^{[111]} - \frac{2}{\sqrt{18}}|2, 2\rangle_D^{[111]} \\ &\quad - \frac{2}{\sqrt{18}}|2, -2\rangle_D^{[111]} - \frac{1}{3}|2, -1\rangle_D^{[111]} . \end{aligned} \quad (6.14)$$

6.1.3 Linewidths

In addition to the transition matrix elements discussed above, the nonlinear susceptibilities (6.4) also depend on the linewidths of the involved exciton states Γ_f . The

homogeneous linewidths of the involved states are for the most part unknown. Additionally, the strong mixing of states makes accurate assignments of states difficult. Various attempts to incorporate the linewidths in a more detailed way did not lead to results in better agreement with experiment than the simple assumption of a constant linewidth of $\Gamma = 150 \mu\text{eV}$ for all states. This linewidth also approximately reproduces the widths of the dominant S and D states, as visible in Figs. 6.2 and 6.3. We will thus use this simple approach for our numerical calculations.

6.1.4 Relative strength of dipole and quadrupole emission processes

In spectra where both quadrupole and dipole emission processes play a role, their relative oscillator strengths have to be considered. According to Ref. [89], the combined transition matrix elements for both processes is given by

$$M \sim \lim_{r \rightarrow 0} \left[-i \left(\tilde{M}_v^* + \tilde{M}_c^* \right) \frac{\partial}{\partial r} \langle T_{\text{out}}^D | \Psi \rangle + \left(-(1 - \alpha) \tilde{M}_v^* + \alpha \tilde{M}_c^* \right) \frac{K}{\sqrt{6}} \langle T_{\text{out}}^Q | \Psi \rangle \right], \quad (6.15)$$

with the exciton wave function $|\Psi\rangle$. The parameter α relates to the chosen center-of-mass transformation (2.18) by $\alpha = m_e / (m_e + m_h) = 0.63$. The states $|T_{\text{out}}^D\rangle$ and $|T_{\text{out}}^Q\rangle$ are related to the states in Eqs. (6.5) and (6.11) via

$$|T_{\text{out}}^D\rangle = \sum_{i \in \{x, y, z\}} E_i^{\text{out}} |\pi_i^D\rangle, \quad (6.16)$$

$$|T_{\text{out}}^Q\rangle = \sum_{v \in \{yz, xz, xy\}} \sqrt{2} (\mathbf{E}^{\text{out}} \otimes \hat{\mathbf{K}})_v |\pi_v^Q\rangle, \quad (6.17)$$

with the normalized wave vector $\hat{\mathbf{K}}$. We see that the correct calculation of the SHG intensities requires the values for the constants \tilde{M}_v^* and \tilde{M}_c^* . These are independent of the exciton state and the magnetic field. We rescale and rewrite Eq. (6.15) as

$$M \sim \lim_{r \rightarrow 0} \left[-iA \frac{\partial}{\partial r} \langle T_{\text{out}}^D | \Psi \rangle + \frac{K}{\sqrt{6}} \langle T_{\text{out}}^Q | \Psi \rangle \right], \quad (6.18)$$

where

$$A = \frac{\tilde{M}_v^* + \tilde{M}_c^*}{-(1 - \alpha) \tilde{M}_v^* + \alpha \tilde{M}_c^*}. \quad (6.19)$$

A now parametrizes the relative contribution of dipole and quadrupole emission processes, i.e., for $|A| \rightarrow \infty$ the spectrum is only determined by dipole processes, whereas for $A \rightarrow 0$, they play no role. In Fig. 6.2 we show a comparison of experimental and numerical spectra for a particular strength of the magnetic field $B = 6 \text{ T}$. Since the SHG spectrum is sensitive to the relative contributions of the quadrupole and dipole emission

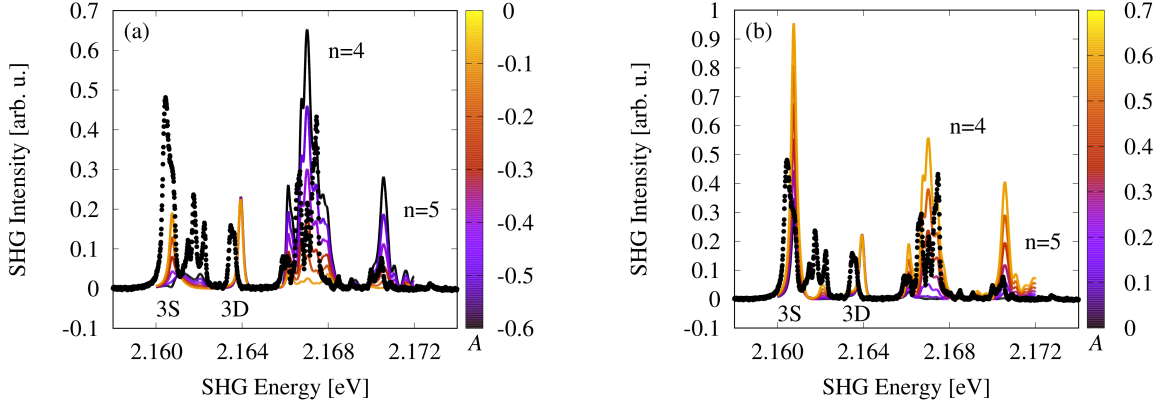


Figure 6.2.: Comparison of experimental (black) and numerical (color palette) SHG spectra in arbitrary units with $\mathbf{E}^{\text{in},2} \parallel [110]$, $\mathbf{E}^{\text{out},2} \parallel [001]$ for different values of A as defined in Eq. (6.19). The wave vector points along the $[1\bar{1}0]$ axis and the magnetic field is applied in Voigt geometry in $[110]$ direction and has a strength of $B = 6$ T. The main features shown belong to principal quantum numbers $n = 3$ and $n = 4$. The color encodes the value of A , which parametrizes the relative strength of dipole emission processes to quadrupole ones. We show the comparison for (a) negative and (b) positive values of A .

processes, we can use this comparison to estimate the value of A . Reasonable agreement is achieved for $A = 0.4$, see Fig. 6.3, and we will choose this value for A for our further calculations. This allows us to estimate the ratio of \tilde{M}_c^* to \tilde{M}_v^* . Using Eq. (6.19), we find

$$\frac{\tilde{M}_c^*}{\tilde{M}_v^*} = -\frac{(1 - \alpha)A + 1}{1 - \alpha A} \approx -1.5. \quad (6.20)$$

Note that this result can only be taken as a rough estimate. We chose the value of A mainly on the basis of the agreement with the 3S and 3D states and the $n = 4$ manifold. Still, the accordance between experiment and theory is not perfect, especially for the lines between the 3S and 3D states, which are not reproduced very well in the simulations. Presumably, this is due to the simplified treatment of the linewidths. We also see that the feature around the 3S states comes out too strong. This is also observed in some of the following spectra. Two remarks are important here. First of all, the linewidth of the 3P state is around $500 \mu\text{eV}$ [30] and thus considerably larger than the value used here. Broader lines generally have weaker SHG intensities, exceptions may be caused by interference between different states. The second remark concerns the line positions of the even exciton states being influenced by the central-cell corrections. Since the central-cell corrections are only an approximation, the positions of the even excitons are not reproduced as faithfully as the positions of the odd states. Instead, the numerical

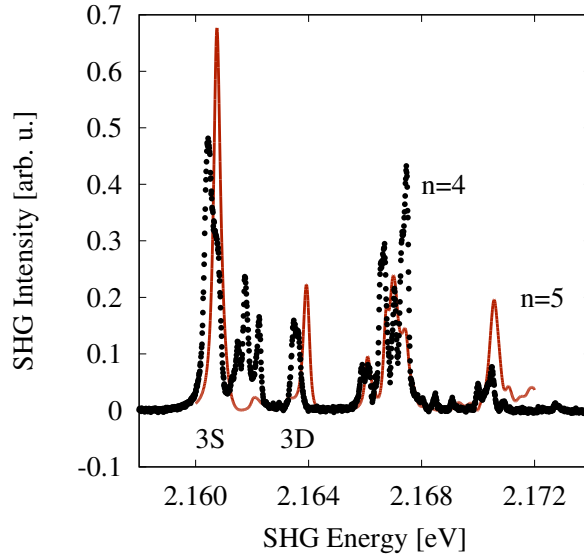


Figure 6.3.: Same as Fig. 6.2 but with a fixed value of $A = 0.4$. With this value, the numerical spectrum matches the experimental spectrum reasonably well. Choosing a higher value for A leads to the 3S peak being excessively high, whereas a lower value results in a too weak $n = 4$ manifold. For further discussion, see text.

S and D excitons are shifted to slightly higher energies as compared to experiment, an effect also observed in Refs. [38, 110] and in previous chapters. The reduced energetic distance between the S and P states probably leads to a stronger mixing and thus, for SHG with a dipole emission step, to an overestimated intensity. The reverse will hold for the D states.

6.2 Discussion of selection rules

Second Harmonic Generation is principally forbidden in inversion symmetric crystals such as Cu_2O . To see this, we consider the SHG amplitude $E_i(2\omega)$ given in Eq. (6.3). The application of the inversion operation switches the signs of the amplitudes E , but leaves the susceptibility χ invariant due to the symmetry of the crystal. It follows that the amplitudes $E_i(2\omega)$ vanish unless the inversion symmetry is broken.

6.2.1 Quadrupole and electric-field induced dipole emission

A two-photon absorption process can only excite even parity states. For two incoming photons with identical polarization \mathbf{E}^{in} , the corresponding two-photon absorption amplitudes are given by the symmetrical cross product (6.9),

$$\mathbf{O}_{\text{TPDD}} \sim \mathbf{E}^{\text{in}} \otimes \mathbf{E}^{\text{in}}. \quad (6.21)$$

The stimulated excitons transform according to Γ_5^+ . Due to their parity, they cannot emit photons in a dipole process. For SHG to become possible, a perturbation has to break the inversion symmetry. In the field-free case, this is accomplished by the wave vector \mathbf{K} , allowing for quadrupole emission processes. For a given polarization of outgoing SHG light \mathbf{E}^{out} , the associated quadrupole transition amplitudes transform like the symmetrical cross product (6.10),

$$\mathbf{O}_{\text{Q}} \sim \mathbf{K} \otimes \mathbf{E}^{\text{out}}. \quad (6.22)$$

Combining both steps, the wave-vector induced SHG amplitude M_K is proportional to

$$M_K(\mathbf{E}^{\text{in}}, \mathbf{E}^{\text{out}}, \mathbf{K}) \sim (\mathbf{E}^{\text{in}} \otimes \mathbf{E}^{\text{in}}) \cdot (\mathbf{K} \otimes \mathbf{E}^{\text{out}}). \quad (6.23)$$

A different way to break the inversion symmetry is to apply an external electric field. This causes the Γ_5^+ excitons to gain an admixture of dipole-allowed Γ_4^- states. This makes a dipole emission step possible. The first order transition amplitude for a dipole emission process from the Γ_5^+ exciton state ψ_i^{5+} to the ground state of the crystal $|g\rangle$ is then given by

$$O_{\text{D},i}^{\mathcal{F}} \sim \sum_{j,k,l} E_l^{\text{out}} \mathcal{F}_j \frac{\langle \psi_i^{5+} | V_j^{\mathcal{F}} | \psi_k^{4-} \rangle \langle \psi_k^{4-} | V_l^D | g \rangle}{E_k - \hbar\omega_{\text{out}}}. \quad (6.24)$$

Here, V_l^D is the term of the dipole operator belonging to the component of the polarization of the outgoing light E_l^{out} and transforms according to Γ_4^- , as does the perturbation $V_j^{\mathcal{F}}$ belonging to the component \mathcal{F}_j of the electric field. The projection operator

$$P^{4-} = \sum_k \frac{|\psi_k^{4-}\rangle \langle \psi_k^{4-}|}{E_k - \hbar\omega_{\text{out}}} \quad (6.25)$$

transforms according to the irreducible representation Γ_1^+ . For a nonvanishing contribution, the total matrix element for a given term in the sum over j and l has to transform as Γ_1^+ . Since the ground state $|g\rangle$ belongs to Γ_1^+ , this can only happen if the complete operator between bra $\langle \psi_i^{5+}|$ and ket $|g\rangle$ transforms as Γ_5^+ . The matrix element is thus proportional to the group theoretical coupling coefficients belonging to the product $\Gamma_4^- \otimes \Gamma_4^- \rightarrow \Gamma_5^+$, which give the symmetrical cross product of the outgoing polarization \mathbf{E}^{out} with the electric field \mathcal{F} ,

$$\mathbf{O}_{\text{D}}^{\mathcal{F}} \sim \mathcal{F} \otimes \mathbf{E}^{\text{out}}. \quad (6.26)$$

Taking the two-photon absorption step into account, the electric-field induced SHG amplitude $M_{\mathcal{F}}$ is given by

$$M_{\mathcal{F}}(\mathbf{E}^{\text{in}}, \mathbf{E}^{\text{out}}, \mathcal{F}) \sim (\mathbf{E}^{\text{in}} \otimes \mathbf{E}^{\text{in}}) \cdot (\mathcal{F} \otimes \mathbf{E}^{\text{out}}). \quad (6.27)$$

Comparing formulas (6.23) and (6.27), we see the close analogy between the wave vector \mathbf{K} and the electric field \mathcal{F} in inducing an SHG signal.

6.2.2 Separating magneto-Stark effect and Zeeman effect in forbidden directions

Second Harmonic Generation induced by the finite wave vector \mathbf{K} is not always possible. If \mathbf{K} is directed along an axis with a C_2 symmetry, an argument analogous to the one for the inversion symmetry above shows that the SHG signal vanishes. Group theoretically, the two-photon absorption process can only excite longitudinal states belonging to the irreducible representation Γ_1 in C_2 . Only transversal states of symmetry Γ_2 can emit a photon. The crystal has a C_2 symmetry for rotations around the [001] and [110] axis and their equivalents. SHG is thus forbidden along those directions.

The direction investigated in this chapter is given by $\mathbf{K} \parallel [1\bar{1}0]$. To produce a SHG signal, the C_2 symmetry has to be broken and states belonging to Γ_1 and Γ_2 have to be coupled to each other. To this end, we consider the application of an external magnetic field. In Faraday configuration, the C_2 symmetry remains. It is therefore necessary to apply the field in Voigt configuration. We choose $\mathbf{B} \parallel [110]$. In this case, in addition to the magnetic field the magneto-Stark electric field has to be treated as well. According to Eq. (5.1) it is directed along $\mathcal{F} \parallel [001]$. Both the magnetic field and the electric field each induce a contribution to the SHG signal. The magnetic field breaks the C_2 symmetry and produces exciton eigenstates containing Γ_1 and Γ_2 admixtures as necessary. The emission step still results from a quadrupole process and can therefore be described using Eq. (6.22). For the electric field, the description given in Sec. 6.2.1 is valid and Eq. (6.27) can be used if the Zeeman splitting is weak.

Evaluating these formulas in the given configuration reveals that the quadrupole emission induced by the Zeeman effect and the dipole emission induced by the magneto-Stark effect have orthogonal polarizations to each other. Orienting the analyzer according to $\mathbf{E}^{\text{out},1} \parallel [110]$, only electric-field induced dipole processes are possible. By contrast, for $\mathbf{E}^{\text{out},2} \parallel [001]$ only quadrupole emission is observable. This allows for the possibility of separating Zeeman-induced SHG from magneto-Stark-induced SHG. Combining $\mathbf{E}^{\text{out},1}$ with $\mathbf{E}^{\text{in},1} \parallel [11\sqrt{2}]$, a SHG signal caused only by the electric field can be observed. To accomplish the same for the Zeeman effect, we need to understand the effect of the magnetic field in greater detail.

6.2.3 Symmetry reduction by the magnetic field

A magnetic field reduces the symmetry of the system and leads to a mixing of previously uncoupled states. The principal effect relevant for SHG production is the coupling of states in the degenerate spaces belonging to the irreducible representation Γ_5^+ and the consequent lifting of their degeneracy. As the magnetic field is of even parity, SHG is only produced by the combination of a two-photon excitation with a quadrupole emission process involving these states. Using Eqs. (6.9) and (6.10), a sum of basis vectors transforming like the Γ_5^+ states ψ_{yz}^{5+} , ψ_{xz}^{5+} and ψ_{xy}^{5+} can be assigned to the two-photon and quadrupole amplitudes for a given pair of polarizations of the incoming and outgoing light. An exciton state can generally be excited in a two-photon absorption process if it has a nonzero overlap with the resulting vector for the two-photon amplitudes. It can emit in a quadrupole step if it has a nonzero overlap with the resulting vector for the quadrupole amplitudes. SHG is thus possible if the admixture by the magnetic field produces exciton states fulfilling both conditions.

To apply these rules in specific cases, we first need to understand the effect of the magnetic field on the exciton states. To this end we will use a perturbation theoretical approach, considering the mixture of the Γ_5^+ states to leading order in \mathbf{B} . We have to consider the lifting of the degeneracy through the magnetic field, leading to mixtures of zeroth order when the splitting is larger than the linewidths of the states. Using the coupling coefficients in Ref. [76], we see that we have to diagonalize the following matrix with the identification $\mathbf{e}_1 = \psi_{yz}^{5+}$, $\mathbf{e}_2 = \psi_{xz}^{5+}$, $\mathbf{e}_3 = \psi_{xy}^{5+}$, $\mathbf{B} = (B, B, 0)$,

$$H_B \sim \frac{1}{\sqrt{2}} \begin{pmatrix} 0 & -B_z & B_y \\ B_z & 0 & -B_x \\ -B_y & B_x & 0 \end{pmatrix} = \frac{1}{\sqrt{2}} \begin{pmatrix} 0 & 0 & B \\ 0 & 0 & -B \\ -B & B & 0 \end{pmatrix}. \quad (6.28)$$

The eigenvectors are

$$\psi_0^{5+} = \frac{1}{\sqrt{2}} \begin{pmatrix} 1 \\ 1 \\ 0 \end{pmatrix}, \quad \psi_{\pm 1}^{5+} = \frac{1}{2} \begin{pmatrix} -1 \\ 1 \\ \mp i\sqrt{2} \end{pmatrix}, \quad (6.29)$$

where the states can be classified according to a magnetic quantum number as given in the subscript of ψ with quantization axis along the [110] direction. Note that the resulting eigenstates couple longitudinal and transversal polarizations. They therefore allow for a SHG signal for arbitrary nonvanishing magnetic field strength if the polarizations are chosen correctly. In fact, these states can of course already be used in the degenerate case without a magnetic field. The reason why a significant SHG signal is only visible for sufficiently high fields lies in the linewidths of the states. To the degree that the different lines overlap, destructive interference prevents the production of SHG light. Physical intuition for this behavior can be gained by understanding the behavior of the Γ_5^+ excitons as damped oscillations in the crystal,

$$\xi_i(t) = \xi_i e^{-\gamma t} e^{i\omega_i t}, \quad (6.30)$$

with $i = 0, \pm 1$ denoting the oscillation modes belonging to the states ψ_i^{5+} with frequencies $\omega_i = E_i/\hbar$ and

$$\boldsymbol{\xi}_0 = \frac{1}{\sqrt{2}} \begin{pmatrix} 1 \\ 1 \\ 0 \end{pmatrix}, \quad \boldsymbol{\xi}_{\pm 1} = \frac{1}{2} \begin{pmatrix} -1 \\ 1 \\ \mp i\sqrt{2} \end{pmatrix}. \quad (6.31)$$

The damping γ is proportional to the linewidths of the states. The femtosecond pulse stimulates an initial amplitude according to

$$\boldsymbol{\xi}(t=0) \sim \mathbf{E}^{\text{in}} \otimes \mathbf{E}^{\text{in}}. \quad (6.32)$$

After the stimulation, the oscillatory modes evolve as given in Eq. (6.30). At every time t , the excitonic oscillation is connected to a macroscopic polarization \mathbf{P} via

$$\mathbf{P}(t) \sim \mathbf{K} \otimes \boldsymbol{\xi}(t), \quad (6.33)$$

which will finally produce the observed SHG light at the boundary of the crystal according to $I(t) \sim |\mathbf{E}^{\text{out}} \cdot \mathbf{P}(t)|^2$. In the configuration considered here, the mode $\boldsymbol{\xi}_0$ does not produce a macroscopic polarization in the crystal, since $\mathbf{K} \otimes \boldsymbol{\xi}_0 = 0$. The other two modes are associated with a circular polarization,

$$\mathbf{P}_{\pm 1}(t) \sim \mathbf{K} \otimes \boldsymbol{\xi}_{\pm 1}(t) = \pm \frac{i}{2} e^{-\gamma t} e^{i\omega_{\pm 1} t} \begin{pmatrix} 1 \\ -1 \\ \mp i\sqrt{2} \end{pmatrix}. \quad (6.34)$$

Because both modes can only be stimulated through their xy parts, they are excited with the same amplitude but differing sign. The total polarization $\mathbf{P}_{\text{total}}(t)$ is therefore linear with a polarization plane normal to the $[110]$ direction. The polarization vector rotates in this plane with the beat frequency $\omega_B = (\omega_{+1} - \omega_{-1})/2$ determined by the difference of the individual frequencies belonging to the oscillatory modes,

$$\mathbf{P}_{\text{total}}(t) \sim e^{-\gamma t} e^{i\frac{\omega_{+1} - \omega_{-1}}{2} t} \begin{pmatrix} \cos(\omega_B t) \\ -\cos(\omega_B t) \\ \sqrt{2} \sin(\omega_B t) \end{pmatrix}. \quad (6.35)$$

Directly after the stimulation by the femtosecond pulse, the polarization points along the longitudinal direction $[1\bar{1}0]$ and no SHG is possible. A SHG signal is produced to the degree that the polarization vector is rotated into the transversal $[001]$ or $[00\bar{1}]$ direction and the emitted photons are therefore polarized along the z axis. This process is determined by the competition between the Zeeman-induced beat frequency ω_B and the damping γ . The integrated intensity and therefore the total number of detected photons is proportional to

$$\int I(t) dt \sim \int_0^\infty |E_z^{\text{out}} e^{-\gamma t} \sin(\omega_B t)|^2 dt \sim \frac{|E_z^{\text{out}}|^2 \omega_B^2}{\gamma(\omega_B^2 + \gamma^2)}. \quad (6.36)$$

Since $\omega_B \sim B$ for small field strengths, the number of photons detected is to leading order quadratic in \mathbf{B} .

The preceding discussion reveals that only an incoming polarization exciting Γ_5^+ states transforming according to xy can produce SHG light. Returning to our goal of separating Zeeman and magneto-Stark effect, we can combine $\mathbf{E}^{\text{out},2} \parallel [001]$ with $\mathbf{E}^{\text{in},2} \parallel [110]$ to generate a SHG signal induced by the Zeeman effect alone.

6.2.4 Additional consideration of the Γ_4^- states

The preceding discussion only took the Γ_5^+ states into account. We now want to consider the role of the dipole-active Γ_4^- excitons. To become SHG-allowed, they have to be mixed with the Γ_5^+ states. This can only happen if the inversion symmetry is broken. The magnetic field alone can therefore not induce a SHG signal mediated by odd parity states. For this, we have to turn our attention to the magneto-Stark effect. Since the Γ_4^- states can emit photons in a dipole process, the two-photon absorption has to be modified here to make SHG allowed. The two-photon absorption transition amplitude for a Γ_4^- state ψ_j^{4-} due to the presence of the electric field is given by

$$O_{\text{TPDD},j}^{\mathcal{F},\Gamma_4^-} \sim \sum_{i,k,l} (\mathbf{E}^{\text{in}} \otimes \mathbf{E}^{\text{in}})_i \mathcal{F}_l \times \frac{\langle g | V_i^{DD} | \psi_k^{5+} \rangle \langle \psi_k^{5+} | V_l^{\mathcal{F}} | \psi_j^{4-} \rangle}{E_k - 2\hbar\omega_{\text{in}}}. \quad (6.37)$$

The relevant components of the two-photon operator V_i^{DD} transforming as Γ_5^+ are given by

$$V_i^{DD} = \sum_{j,k} \frac{|\epsilon_{ijk}|}{\sqrt{2}} \sum_l \frac{V_j^D |l\rangle \langle l| V_k^D}{E_l - \hbar\omega_{\text{in}}}, \quad (6.38)$$

with the Levi-Cevita symbol ϵ_{ijk} , the dipole operators $V_{j,k}^D$ for the individual steps and the virtual intermediate states $|l\rangle$. The components of the perturbation belonging to the electric field $V_l^{\mathcal{F}}$ behave as Γ_4^- . The projection operator

$$P^{5+} = \sum_k \frac{|\psi_k^{4-}\rangle \langle \psi_k^{4-}|}{E_k - \hbar\omega_{\text{out}}} \quad (6.39)$$

again transforms according to Γ_1^+ . The matrix elements are thus also proportional to the same coupling coefficients as in the discussion of the Γ_5^+ states. The modified two-photon absorption amplitude is therefore given by

$$\mathbf{O}_{\text{TPDD}}^{\mathcal{F},\Gamma_4^-} = \hat{\mathcal{F}} \otimes (\mathbf{E}^{\text{in}} \otimes \mathbf{E}^{\text{in}}). \quad (6.40)$$

The Γ_4^- states emit SHG radiation by a dipole step. The SHG transition amplitude is thus proportional to

$$\begin{aligned}
M_{\mathcal{F}}^{\Gamma_4^-}(\mathbf{E}^{\text{in}}, \mathbf{E}^{\text{out}}, \mathcal{F}) &\sim \mathbf{O}_{\text{TPDD}, \mathcal{F}} \cdot \mathbf{O}_{\text{D}} \\
&= (\hat{\mathcal{F}} \otimes (\mathbf{E}^{\text{in}} \otimes \mathbf{E}^{\text{in}})) \cdot \mathbf{E}^{\text{out}} \\
&= (\mathbf{E}^{\text{in}} \otimes \mathbf{E}^{\text{in}}) \cdot (\hat{\mathcal{F}} \otimes \mathbf{E}^{\text{out}}), \tag{6.41}
\end{aligned}$$

and we get the same formula as for the Γ_5^+ states. Our conclusions regarding the polarization dependencies of the Zeeman-induced and magneto-Stark-induced SHG amplitudes thus remain unchanged by the additional consideration of the Γ_4^- excitons. In particular, it remains the case that with the combination of polarizations given by $\mathbf{E}^{\text{in},1} \parallel [11\sqrt{2}]$ and $\mathbf{E}^{\text{out},1} \parallel [110]$ only SHG induced by the magneto-Stark effect is visible and with the combination of polarizations given by $\mathbf{E}^{\text{in},2} \parallel [110]$ and $\mathbf{E}^{\text{out},2} \parallel [001]$ only SHG induced by the Zeeman effect is visible.

These combinations of polarizations for the incoming and outgoing light allow for the separation of the Zeeman and magneto-Stark effect to the degree that the approximations made in the preceding discussion are valid. In the first configuration with $\mathbf{E}^{\text{in},1}$ and $\mathbf{E}^{\text{out},1}$, quadrupole emission is forbidden entirely. Restricting our treatment to the dominant contributions, only the electric-field induced mixture of Γ_4^- and Γ_5^+ excitons can produce any SHG signal at all, even for strong fields. For the second configuration with $\mathbf{E}^{\text{in},2}$ and $\mathbf{E}^{\text{out},2}$, only weaker statements are possible. The electric-field induced SHG vanishes only if the Zeeman splitting between the states is small. Still, if the energetic distance of a SHG-active Γ_5^+ multiplet to the dipole-active Γ_4^- states is large, the contribution of dipole emission processes remains minor. This effect can be seen in Fig. 6.2, where the second combination of polarizations is used. The high energy 3D line shows an especially small influence of the electric field, its intensity being almost unaffected by variations in the strength of dipole emission processes. This is probably explained by its high energetic distance to the 3P lines and other odd parity states as stated above.

Apart from allowing for the separation of Zeeman and magneto-Stark effect, the formulas for the SHG amplitudes derived in this section can be used for the detailed discussion of the polarization dependencies of the SHG signal. Since $M_{\mathcal{F}}(\mathbf{E}^{\text{in}}, \mathbf{E}^{\text{out}}, \mathcal{F})$ and the amplitude induced by the magnetic field are different functions of the polarizations, the effects can be distinguished experimentally. Complementary to the discussion here, this is done in the manuscript by A. Farenbruch *et al.* [109], where the polarization dependencies for SHG processes other than the ones considered here are studied as well.

6.3 Source of experimental data

The experiment was carried out by the experimental group under M. Bayer at the TU Dortmund University. The experimental set-up is described in Ref. [109]. It allows for the application of magnetic fields with strengths up to 10 T in Faraday and Voigt configuration to the sample, which was cooled down to 1.4 K. Using half-wave plates, the linear polarization of the incoming laser light and of the outgoing SHG light can be varied independently. Excitons were excited by a femtosecond laser pulse (200 fs, spectral width of 10 meV) with a frequency-doubled intensity profile centered on 2.164 eV and a FWHM of 14 meV, cf. Ref. [64]. To take its influence into account for the numerical calculations, we convolute the numerically obtained spectrum with a Gaussian function with the appropriate parameters.

6.4 Presentation of spectra

In Fig. 6.4, both experimental and numerical spectra with the polarizations discussed in Sec. 6.2 are shown. A general agreement between experiment and numerical spectra is observed. Some discrepancies remain: For both spectra, the numerical features in the region of the 3S states are too strong. This is probably due to the central-cell corrections as explained at the end of Sec. 6.1.4.

In general, the SHG spectrum is determined by a combination of the Zeeman and magneto-Stark effect. In Fig. 6.5, we show additional examples of magnetic-field-induced SHG spectra in a forbidden direction. The used combination of polarizer and analyzer in Fig. 6.5 (a) produces a spectrum that is a product of both the Zeeman and magneto-Stark effect in full generality, whereas Fig. 6.5 (b) shows another spectrum entirely produced through the MSE, since $\mathbf{K} \otimes \mathbf{E}^{\text{out}} = 0$ in this case. Here too, in both cases reasonable agreement between experiment and numerical simulation is achieved. In the numerical data in Fig. 6.5 (a), a strong feature appears for $E \approx 2.162$ eV, $B \approx 8 - 10$ T that is not seen in the experiment. The two remarks from the end of section 6.1.4 apply here: The inaccuracies in the central-cell corrections and the linewidths lead to an overestimated SHG intensity. Fig. 6.5 (b) on the other hand shows generally good agreement.

In Fig. 6.6, we show pictures of SHG along the allowed direction [111]. Some agreement is observed, but there are also significant differences. Most evidently, the D excitons are stronger than the S excitons in the numerical data, but in the experiment the reverse is the case. A possible explanation is to be found in the treatment of the center-of-mass motion. Due to the inversion symmetry of cuprous oxide, the SHG signal in the field-free case can be thought of as being induced by the finite wave vector \mathbf{K} . For $\mathbf{B} \neq 0$, this will give an additional contribution to the spectrum that requires a more careful

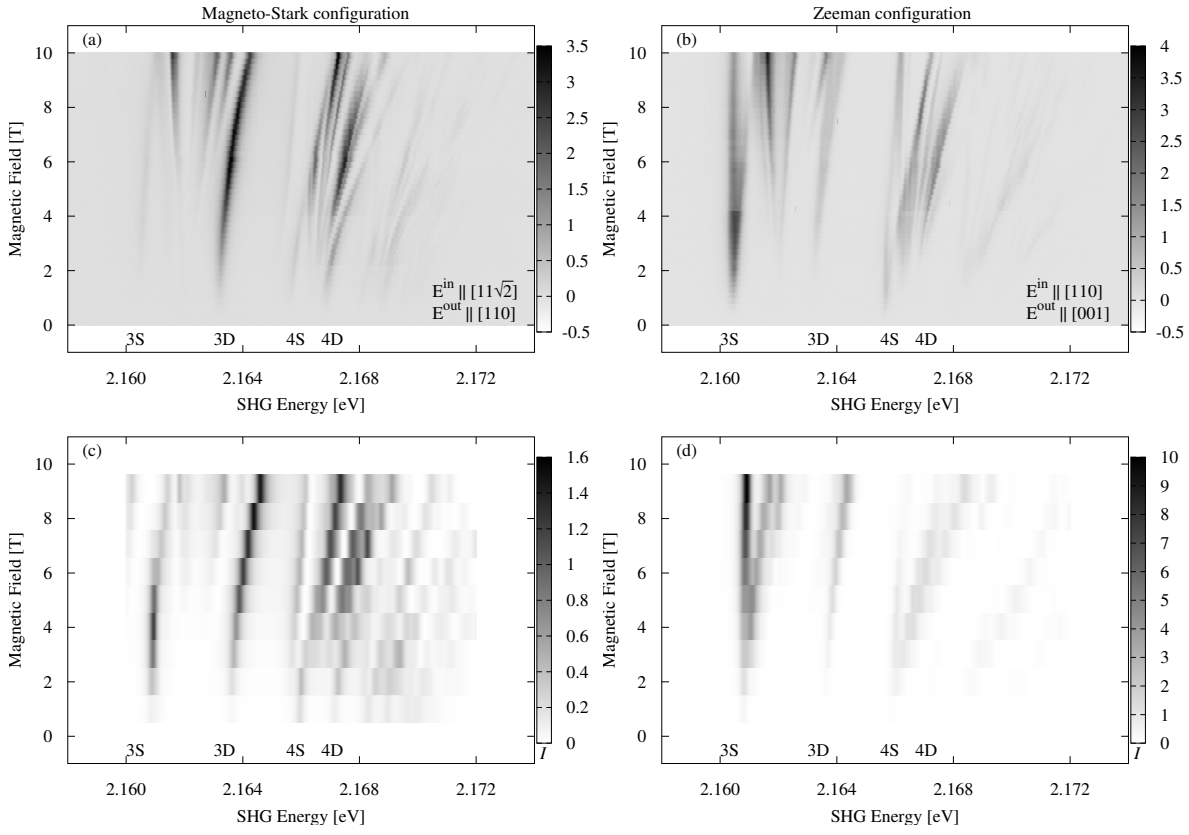


Figure 6.4.: Experimental SHG spectra in arbitrary units with (a) $\mathbf{E}^{\text{in},1} \parallel [11\sqrt{2}]$, $\mathbf{E}^{\text{out},1} \parallel [110]$ and (b) $\mathbf{E}^{\text{in},2} \parallel [110]$, $\mathbf{E}^{\text{out},2} \parallel [001]$. The wave vector points along the $[1\bar{1}0]$ axis and the magnetic field is applied in $[110]$ direction. The spectra on the left hand side are mediated through the magneto-Stark effect and the spectra on the right are mediated by the Zeeman effect. The main features visible belong to excitons with principal quantum numbers $n = 3$ and $n = 4$. The corresponding numerically calculated spectra (see Eq. (6.2)) are shown in (c) and (d). Experimental data taken from Ref. [111].

consideration of the center-of-mass motion than the one used here. For SHG in forbidden directions, the center-of-mass motion by itself does not induce a SHG signal, and thus our treatment is sufficient in that case. As expected, the Voigt configuration as seen in Fig. 6.6 (b) shows more features compared to the Faraday configuration in Fig. 6.6 (a) due to the additional mixing caused by the electric field.

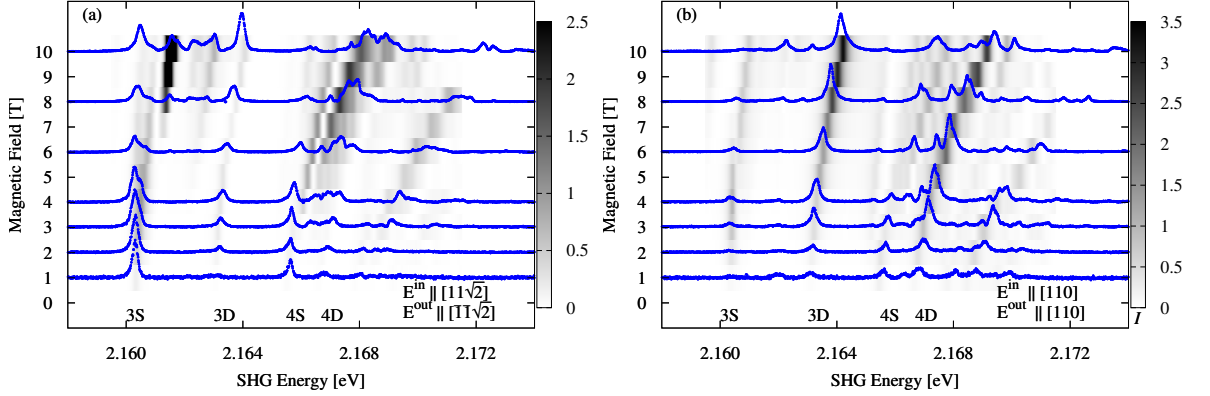


Figure 6.5.: Experimental SHG spectra (blue lines) with $\mathbf{B} \parallel [001]$, $\mathbf{K} \parallel [1\bar{1}0]$ and (a) $\mathbf{E}^{\text{in}} \parallel [11\sqrt{2}]$, $\mathbf{E}^{\text{out}} \parallel [\bar{1}\bar{1}\sqrt{2}]$ and (b) $\mathbf{E}^{\text{in}} \parallel [110]$, $\mathbf{E}^{\text{out}} \parallel [110]$. The corresponding numerically simulated spectra (grayscale) have been shifted by -0.5 meV to allow for a better comparison. The main visible features belong to excitons with principal quantum numbers $n = 3$ and 4 . The feature visible at $E \approx 2.162$ eV, $B \approx 8 - 10$ T in the numerical spectrum in panel (a) has an intensity exceeding the color palette scale and is most likely due to some numerical artifact. Experimental data taken from Ref. [111].

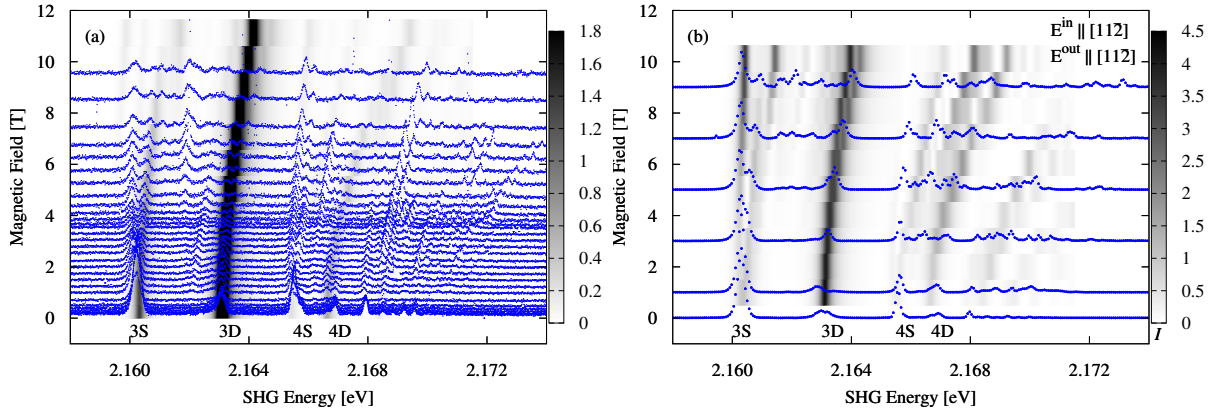


Figure 6.6.: Experimental spectra (blue lines) with $\mathbf{K} \parallel [111]$, $\mathbf{E}^{\text{in}} \parallel \mathbf{E}^{\text{out}} \parallel [11\bar{2}]$ in (a) Faraday configuration with $\mathbf{B} \parallel [111]$ and (b) Voigt configuration with $\mathbf{B} \parallel [1\bar{1}0]$. The corresponding numerically simulated spectra (shifted by -0.5 meV) are shown in grayscale. The main features visible belong to excitons with principal quantum numbers $n = 3$ and 4 . Note that the 3D line in panel (a) exceeds the upper limit of the gray scale. Experimental data taken from Ref. [111].

7

Rydberg excitons in electric and magnetic fields

In Chapters 5 and 6, we studied the application of an external magnetic field. In the Voigt configuration, this led to an additional effective electric field over the magneto-Stark effect. The resulting electric field strengths were quite small. By contrast, we now want to explore field strengths in the regime where autoionization takes place. To this end, we need to extend our numerical approach to include the complex-coordinate-rotation method. In Refs. [65, 111], absorption and second-harmonic generation spectra of magnetoexcitons in cuprous oxide have been calculated numerically and compared with experimental data. We thus want to extend these results to external electric fields and parallel electric and magnetic fields. The spectra calculated in this chapter have been published in Ref. [93].

Taking proper account of the complex valence band structure allowed Schweiner *et al.* to calculate the spectra of excitons and magnetoexcitons [35, 65], achieving excellent agreement with experimental data. In Chapter 5, we presented spectra extending this approach to the Voigt configuration and discussed the effect of the perpendicular orientation of exciton momentum and magnetic field in the framework of the magneto-Stark effect. Due to the weakness of the induced electric field, the line positions are only very weakly affected. The more prominent consequence is a reshuffling of oscillator strength to a greater number of lines due to the reduced symmetry and associated mixing of states.

In this chapter, we want to discuss the application of an *external* electric field to the spectra, which leads to the dissociation of excitons as investigated by Heckötter *et al.* [139]. They observed similar behavior as known from the Stark effect in atoms, with stronger dissociation for higher principal quantum numbers n , but weaker dissociation for higher energies within a multiplet of fixed n . In Ref. [139], the results were compared to calculations with a simplified model.

Here, we want to go beyond these calculations and include the valence band terms into

the description, which is required for the proper treatment of the crystal environment with cubic symmetry. For the calculation of the autoionization resonances, we use the complex scaling method [94–96] as introduced in Sec. 2.7, which has also already been applied to the calculation of resonances of the hydrogen atom in external fields [140–143]. We calculate the appearance of resonance states in the absorption spectra in Faraday configuration as a function of the applied fields strengths, first for an applied electric field and then for parallel electric and magnetic fields. The solution of the Schrödinger equation in a complete basis additionally allows for the calculation of relative oscillator strengths.

We first present the theoretical model used in this chapter in section 7.1 before presenting results in section 7.2.

7.1 Application of an external electric field

In this chapter, we use the Hamiltonian (2.2) including external fields as described in Sec. 2.4. We neglect the central-cell corrections because we are interested in exciton states with high principal quantum numbers, which are less affected by them. It reads,

$$H = E_g + H_e(\mathbf{p} + e\mathbf{A}(\mathbf{r})) + H_h(-\mathbf{p} + e\mathbf{A}(\mathbf{r})) + V(\mathbf{r}) + H_B + V_F(\mathbf{r}), \quad (7.1)$$

where the magnetic field is added in the same way as in previous chapters. The electric field \mathbf{F} is added in the term

$$V_F(\mathbf{r}) = -e\mathcal{F} \cdot \mathbf{r}. \quad (7.2)$$

In comparison to Chapters 5 and 6, the electric field here is strong enough to cause autoionization. We thus use the complex-coordinate-rotation method as described in Sec. 2.7 to treat the resulting resonances.

The resulting Hamiltonian is diagonalized as outlined in Sec. 2.8. With the calculated eigenstates we can obtain the oscillator strengths for circularly polarized light using

$$f_{\text{rel}} \sim \left(\lim_{r \rightarrow 0} \frac{\partial}{\partial r} \langle \sigma_z^\pm | \Psi(\mathbf{r}) \rangle \right)^2 \quad (7.3)$$

with

$$|\sigma_z^+\rangle = |2, -1\rangle_D, \quad |\sigma_z^-\rangle = -|2, 1\rangle_D. \quad (7.4)$$

We use the abbreviation

$$\begin{aligned} |F_t, M_{F_t}\rangle_D &= |(S_e, S_h) S, I; I + S, L; F_t, M_{F_t}\rangle \\ &= |(1/2, 1/2) 0, 1; 1, 1; F_t, M_{F_t}\rangle. \end{aligned} \quad (7.5)$$

We can then calculate the absorption spectrum using [144]

$$f(E) = -\frac{1}{\pi} \text{Im} \sum_j \frac{f_{\text{rel}}^{(j)}}{E - E_j} \quad (7.6)$$

with the energy E and the complex energies E_j of the resonances.

7.2 Discussion of spectra

We present the investigated resonances in the complex energy plane and the resulting absorption spectra for circularly polarized light. We only show resonances and removed the bound states from the spectra, which otherwise would appear as delta-like peaks. Note that we only include the linewidths caused by the ionizing effect of the electric field, the broadening caused by the interaction with phonons is not included.

We begin with excitons in an external electric field and afterwards in parallel electric and magnetic fields.

7.2.1 Electric fields in [001] direction

In Figs. 7.1 and 7.2 we show the complex resonances and absorption spectrum for excitons in an external electric field along the [001] axis with field strengths $\mathcal{F} = 7200 \text{ V/m}$ and $\mathcal{F} = 9000 \text{ V/m}$, respectively. We can see that the spectra for σ^+ and σ^- polarized light are identical.

We first discuss the spectrum at $\mathcal{F} = 7200 \text{ V/m}$, Fig. 7.1, which includes resonances with principal quantum numbers in the range of $n = 8$ to $n = 15$. Since the linewidth and lifetime are inversely related, long-lived resonances manifest as thin peaks. As known from the hydrogen atom in electric field, the linewidths increase with increasing principal quantum number n , but within each n -multiplet the linewidth decreases with the energy, although the different multiplets already strongly overlap at this field strength, so this is hard to verify in our spectra.

We can compare the spectrum with the situation when the electric field is increased to $\mathcal{F} = 9000 \text{ V/m}$, as shown in Fig. 7.2. As expected, additional long-lived resonances appear at lower energies and the linewidths of the resonances are increased in general.

This point is underlined in Fig. 7.3, where multiple spectra with different electric fields ranging from $\mathcal{F} = 3400 \text{ V/m}$ to $\mathcal{F} = 21600 \text{ V/m}$ are shown. Note again, that only the resonances are shown, meaning that there are additional bound states which are not depicted, mostly at lower energies.

The figure helps illustrate the effects of increasing the electric field strength. Most evidently, the range where resonances are found increases from bottom to the top. Owing to the lowering of the potential barrier (cf. Fig. 2.3), additional bound states become

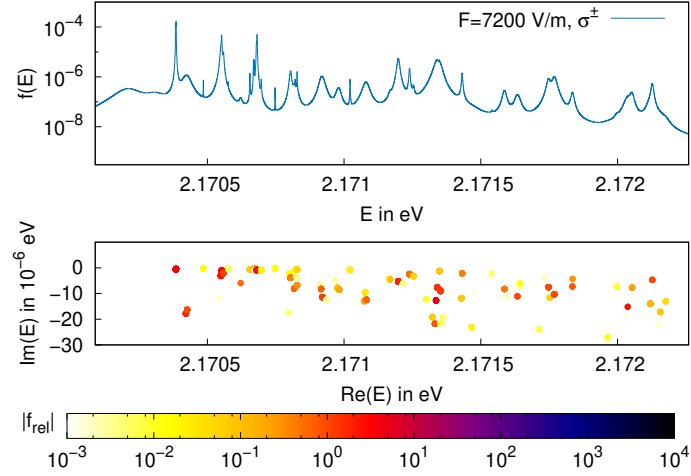


Figure 7.1.: *Lower panel*: Resonances in the complex energy plane with an applied electric field $\mathcal{F} = 7200 \text{ V/m}$ in $[001]$ direction. The color shows the absolute value $|f_{\text{rel}}|$ of the relative oscillator strength for σ^\pm polarized light. *Upper panel*: Corresponding simulated absorption spectrum. Light with σ^+ and σ^- polarization leads to coincident spectra. Taken from Ref. [93].

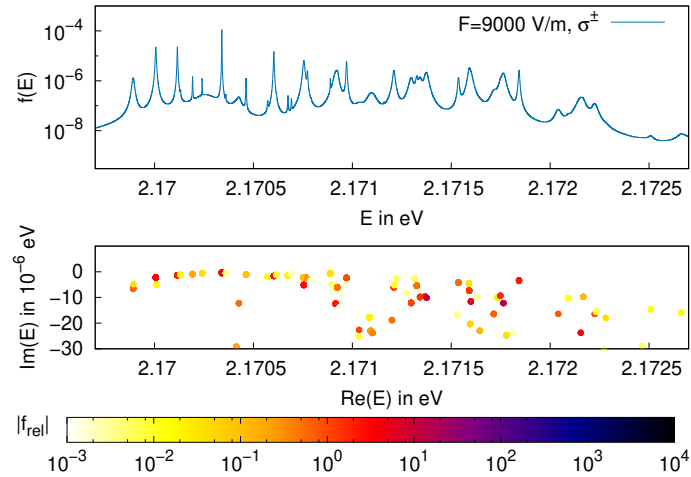


Figure 7.2.: Same as figure 7.1 but with $\mathcal{F} = 9000 \text{ V/m}$. Taken from Ref. [93].

resonances at lower energies. Additionally, the Stark effect leads to a fan-like splitting of states which contributes to this observation. The lowering of the potential barrier also shifts the resonances down in the complex plane, leading to a broadening.

Note that we could not yet assign any quantum numbers, even approximate, to our

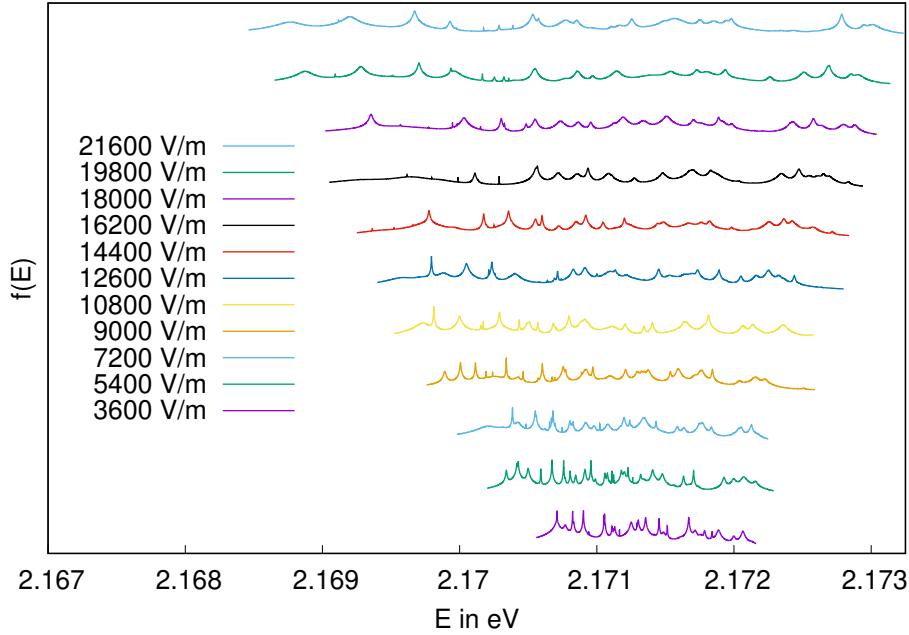


Figure 7.3.: Resonance spectra for σ^\pm polarized light as a function of the electric field. The electric field is orientated in the [001] direction and varies from $\mathcal{F} = 3600$ V/m (bottom) to $\mathcal{F} = 21600$ V/m (top). Taken from Ref. [93].

calculated resonances, since doing so would have required a much smaller stepsize when increasing the field strength, which was beyond our numerical capabilities.

7.2.2 Parallel electric and magnetic fields

The calculation of resonances in an external electric field as in section 7.2.1 is an important test case for the application of the complex-coordinate-rotation method. Now we want to go beyond this and additionally apply a magnetic field, also in [001] direction. We thus have the situation of parallel electric and magnetic fields.

In Figs. 7.4 and 7.5 we present resonances and absorption spectra for σ^- polarized and σ^+ polarized light respectively. The electric field strength is $\mathcal{F} = 7200$ V/m as in Fig. 7.1, but here we add a magnetic field $B = 0.5$ T. This leads to an additional reduction of the symmetry of the system, completely lifting the degeneracy of the spectrum. Because of this, the spectra for the different polarizations differ now, in contrast to Figs. 7.1 and 7.2. As known from Ref. [65], σ^- polarized and σ^+ polarized light excites different excitons in a magnetic field parallel to [001]. Using our coupling scheme, we can deduce that states with large admixtures of $L = 1$, $F_t = 2$, $M_{F_t} = -1$ respond to σ^+ polarized light and states with large admixtures of $L = 1$, $F_t = 2$, $M_{F_t} = +1$ respond to σ^- polarized light. Again, we are unable to assign quantum numbers to the calculated states.

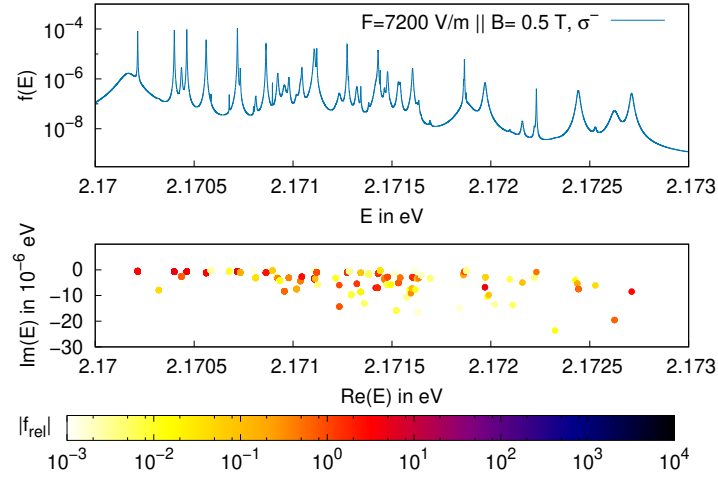


Figure 7.4.: Complex resonance positions and corresponding spectrum for parallel electric and magnetic field along [001] direction with $\mathcal{F} = 7200$ V/m and $B = 0.5$ T. The light is σ^- polarized. Taken from Ref. [93].

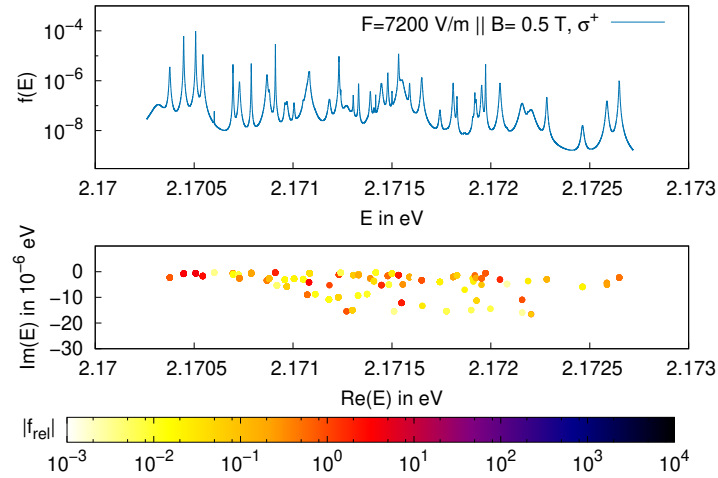


Figure 7.5.: Same as figure 7.4 but with σ^+ polarized light. Taken from Ref. [93].

Excitons in parallel fields form a non-Hermitian system with two controllable external parameters. This opens up the possibility for the observation of exceptional points. Feldmaier *et al.* theoretically investigated this prospect in a hydrogenlike model, observing that the required field strengths are much more experimentally accessible than in the hydrogen atom [145]. Our results thus provide an important stepping stone towards the study of exceptional points in excitons of the yellow series under the full consideration of

the band structure and additional corrections. This will help advance the experimental search for exceptional points in Rydberg systems.

In Chapter 8, we will look at another application of the complex-coordinate-rotation method, the green exciton series. On the basis of this, we can then go on to calculate interseries transitions between the yellow and green series in Chapter 9.

8

The green exciton series in cuprous oxide

In Chapter 7 we needed to introduce resonances with complex energies in order to take autoionization in the presence of an external electric field into account. We here numerically investigate the states of the green exciton series in cuprous oxide. Considering the coupling to the yellow series and especially to the yellow continuum, the green excitons are also quasibound resonances with a finite lifetime which cannot conveniently be described with Hermitian operators. To calculate their positions and linewidths, we thus use the method of complex-coordinate rotation again, leading to a non-Hermitian complex eigenvalue problem as well. We first investigate the odd parity states, finding that the behavior of the dominant P states is very well approximated by a modified Rydberg formula using a negative quantum defect. The corresponding linewidths induced by the coupling to the yellow continuum decrease with the third power of the principal quantum number. We published these results in Ref. [146].

We then extend the calculations by the inclusion of the central-cell corrections and present the even parity green states, completing the calculation of the green resonances. We investigate several features of the even-parity spectrum, including the linewidths, two-photon absorption strengths and exchange splittings of the most prominent S states.

In an idealized model, excitons can be described as bound states between electrons and holes. In general, a range of mechanisms make scattering possible and induce a finite linewidth. The excitons become quasibound states or resonances. In case of the yellow excitons, the most prominent process is the scattering with phonons [73, 74]. Bound states can also become resonances by application of an external electric field, which allows for tunneling processes into the unbound region [93, 139].

In cuprous oxide, the excitons constituted by electrons in the lowest conduction Γ_6^+ band and holes in the highest Γ_7^+ valence band are part of the yellow exciton series. An electron can also be lifted from the Γ_8^+ valence band into the Γ_6^+ conduction band, forming a green exciton [51, 147, 148]. Since the energy of the Γ_8^+ valence band is lowered by an amount Δ in comparison to the uppermost Γ_7^+ valence band, all green excitons, except for the even parity 1S states investigated in [38, 60], lie within the energy range

of the yellow continuum. Yellow and green states are coupled by the valence band structure [35, 86], and the green states with principal quantum numbers $n \geq 2$ are therefore resonances instead of truly bound states.

An efficient numerical method for the computation of the bound states of Cu_2O including the impact of the valence band structure (but ignoring the phonon coupling) is the diagonalization of the Hamiltonian using a complete basis set [35, 38]. The method can be applied to obtain the bound states of the yellow exciton series at energies below the gap energy $E_g = 2.17208 \text{ eV}$ and the green 1S excitons, which are the only bound states of the green exciton series. However, the Hermitian eigenvalue problem does not allow for the computation of unbound resonance states.

Recent work by Krüger and Scheel has focused on the interseries transitions such as between the yellow and green excitons [66], which we will discuss in Chapter 9. A better understanding of the unbound resonances of the green series is a valuable prerequisite for this. A convenient description of these resonance states is achieved by the introduction of a complex energy, where the imaginary part is related to the linewidth of the quasibound state. These complex energies can be calculated by way of the complex-coordinate-rotation method [94–96] as presented in Sec. 2.7, where a complex scaling operation is performed to expose the resonance positions in the complex plane. In this chapter we again augment the numerical algorithm introduced in Refs. [35, 38] for the computation of bound excitons by application of the complex-coordinate rotation. This rotation turns the Hermitian eigenvalue problem into a non-Hermitian system, and thus allows for the computation of the complex resonance energies of the green excitons. To this end, we first recall the associated theory in Sec. 8.1. We present our numerical results on the odd and even parity states in Secs. 8.2 and 8.3, respectively, and discuss their implications.

8.1 | The green excitons

To study the green excitons, we can use the theoretical description given by the Hamiltonian (2.2), since it provides a unified model of the yellow and green series,

$$H = E_g + H_e(\mathbf{p}_e) + H_h(\mathbf{p}_h) + V(\mathbf{r}_e - \mathbf{r}_h) + V_{\text{CCC}}. \quad (8.1)$$

At first, we only study the odd-parity excitons in this chapter and hence leave out the central-cell corrections, adding them back in for the calculation of the even-parity states. The crucial difference between the yellow and green series arises from the spin-orbit coupling

$$H_{\text{SO}} = \frac{2}{3} \Delta \left(1 + \frac{1}{\hbar^2} \mathbf{I} \cdot \mathbf{S}_h \right), \quad (8.2)$$

which is part of the hole kinetic energy $H_h(\mathbf{p}_h)$. It can be diagonalized by introducing the effective hole spin $\mathbf{J} = \mathbf{I} + \mathbf{S}_h$. We thus obtain a splitting between states with

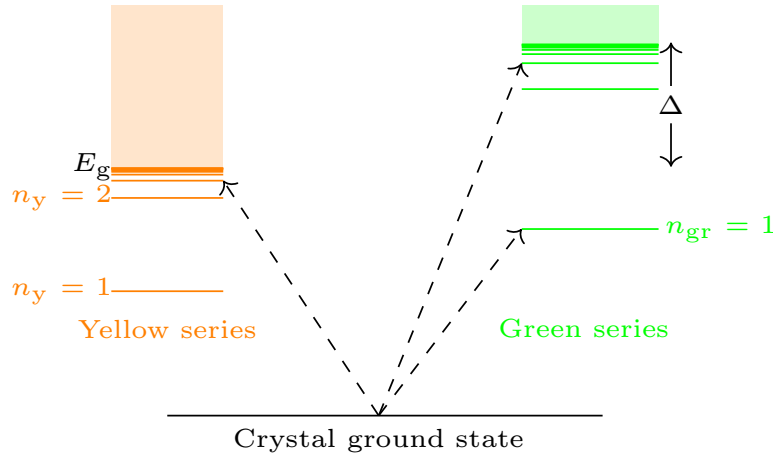


Figure 8.1.: Scheme of the relative energetic arrangements of the yellow and green exciton series. All green excitons except for the 1S state are located inside of the yellow continuum. The valence band structure couples these states to the continuum, making them resonances rather than bound states. The arrows indicate transitions from the crystal ground states into the two exciton series. Here, we will study transitions like those indicated by the arrows going to the right side, i.e., to the green series.

$J = 1/2$ and $J = 3/2$. The former belong to the yellow series and the latter to the green series. The expression (8.2) is set up in such a way that the yellow $J = 1/2$ states remain unaffected, while the green $J = 3/2$ states are lifted by the energy Δ . This leads to the situation depicted in Fig. 8.1. Since the green exciton states above the yellow threshold are coupled to the yellow continuum, they are not bound states but quasibound resonances. For this reason, we have to use the complex-coordinate-rotation method as outlined in Sec. 2.7 and used in the previous Chapter 7.

For the calculation of the even-parity series, we also need to take into account the central-cell corrections. The matrix elements for the Haken potential, given in Appendix D of Ref. [38], requires the evaluation of a sum of alternating terms with large absolute values. To study resonance states, we additionally need to perform the complex rotation. Implementing the central-cell conditions under these conditions is the step which allows us to go beyond Ref. [146] and calculate the green even parity states.

One-photon transition spectra Using the eigenfunctions obtained from the solution of the resulting generalized eigenvalue problem (2.27), we are able to simulate absorption spectra for the yellow and green series. The absorption coefficients for the odd-parity states are calculated with the formula [93]

$$\sigma(E = \hbar\omega_{\text{ph}}) \cong \text{Im} \sum_{\text{f}} \frac{f_{\text{rel}}^{\text{f}}}{E_{\text{f}} - E}, \quad (8.3)$$

where E_j are the complex energies of the resonance states and

$$f_{\text{rel}} \sim \left(\lim_{r \rightarrow 0} \frac{\partial}{\partial r} \langle \sigma_z^\pm | \Psi(\mathbf{r}) \rangle \right)^2 \quad (8.4)$$

is the complex generalization of the relative oscillator strength. The overlaps with the states

$$|\sigma_z^+\rangle = |2, -1\rangle_D, \quad |\sigma_z^-\rangle = -|2, 1\rangle_D, \quad (8.5)$$

determine the spectrum for σ^+ and σ^- polarized light. Here, we use the abbreviation

$$\begin{aligned} |F_t, M_{F_t}\rangle_D &= |(S_e, S_h) S, I; I + S, L; F_t, M_{F_t}\rangle \\ &= |(1/2, 1/2) 0, 1; 1, 1; F_t, M_{F_t}\rangle, \end{aligned} \quad (8.6)$$

to denote the states with a coupling scheme differing from the one in the basis states.

Two-photon transition spectra In the yellow and green series in cuprous oxide, one-photon dipole transitions can only excite odd parity states. Since we are also interested in even parity excitons here, we additionally study two-photon absorption processes [132] in the following.

For the calculation of the two-photon oscillator strengths, we first have to consider the tensor product of irreducible representations $\Gamma_4^- \otimes \Gamma_4^- = \Gamma_1^+ \oplus \Gamma_3^+ \oplus \Gamma_4^+ \oplus \Gamma_5^+$ resulting from the combination of the two dipole operators belonging to the two photons. As discussed in greater detail for example in Ref. [111], only the term with irreducible representation Γ_5^+ contributes to leading order. In the following, we only consider processes where the two-photon operator transforms according to this representation. Only states of the same symmetry Γ_5^+ can then be excited. It is thus useful to get an overview of the relevant states and their irreducible representations in Sec. 8.3.1.

For a detailed numerical calculation of the relative two-photon oscillator strengths, we use the formula given in Ref. [38],

$$f_{\text{rel}}^{\text{TP}} \sim \lim_{r \rightarrow 0} {}_T \langle 1, M'_{F_t} | \Psi(\mathbf{r}) \rangle \langle \Psi(\mathbf{r}) | 1, M'_{F_t} \rangle_T, \quad (8.7)$$

where $|\Psi\rangle$ is the wave function. $|F_t, M_{F_t}\rangle_T$ is an abbreviation for

$$\begin{aligned} |F_t, M_{F_t}\rangle_T &= |(S_e, S_h) S, I; I + S, L; F_t, M_{F_t}\rangle \\ &= |(1/2, 1/2) 0, 1; 1, 0; F_t, M_{F_t}\rangle, \end{aligned} \quad (8.8)$$

where the coupling scheme of the spins and angular momenta differs from the one introduced before.

Using the oscillator strengths (8.7), we can calculate the photoabsorption spectra. The calculation of asymmetric Lorentz peaks as discussed in Refs. [93, 96, 144] in the case

of one-photon absorption can be understood as an application of the optical theorem of scattering theory [149], which relates the extinction cross section to the amplitude for scattering in the forward direction. Adopting analogous reasoning for the case of two-photon scattering, we obtain

$$\sigma^{\text{TP}}(E = 2\hbar\omega_{\text{ph}}) \cong \text{Im} \sum_{\text{f}} \frac{f_{\text{rel}}^{\text{TP,f}}}{E_{\text{f}} - 2\hbar\omega_{\text{ph}}}, \quad (8.9)$$

where we additionally assumed that the laser frequency is approximately constant over the investigated spectral range. The frequency of the incoming photon is denoted by ω_{ph} . The summed terms (8.7) can be understood as the amplitudes for the excitation of the resonance states f , followed by the relaxation back to the ground state with the emission of the outgoing photon pair in the same direction, i.e. forward scattering. For vanishing linewidths, Eq. (8.9) reduces to delta peaks.

8.2

The spectrum of odd-parity green excitons

The results for both the yellow and green exciton series are presented in Fig. 8.2. In the computations we have used the basis set (2.29) with $N + L < 50$, $|\alpha| = 63$, and $\theta = 0.14$ and restricted ourselves to the odd states, as only those contribute to the absorption coefficient of one-photon transitions. In the lower part of Fig. 8.2 we show the resonance positions of the yellow and green exciton series in the complex energy plane. Clearly visible are the bound states of the yellow exciton series at energies below the gap energy E_{g} and the resonances of the green exciton series at energies below the band edge $E_{\text{g}} + \Delta$. Above the band edges energies are bundled along straight lines and rotated into the complex plane. The rotation angle is nearly given by 2θ as is expected for complex rotated continuum states [94–96]. Note that the numerical resonance positions are already rotated into the lower complex energy plane at energies slightly below the band edges. This is a numerical artifact due to the finite size of the basis set.

The upper part of Fig. 8.2 presents the corresponding absorption spectrum obtained with Eq. (8.3). Since we do not include the effects of phonons in our model, the yellow exciton states here are bound states with infinite lifetimes. To avoid δ function type absorption peaks we have simulated the interaction with phonons by manually introducing the finite linewidths

$$\gamma_n = 9 \text{ meV}(n^2 - 1)/n^5 \quad (8.10)$$

with an effective principal quantum number

$$n = \sqrt{E_{\text{Ryd}}/(E_{\text{g}} - E) + \delta_{\text{P}}} \quad (8.11)$$

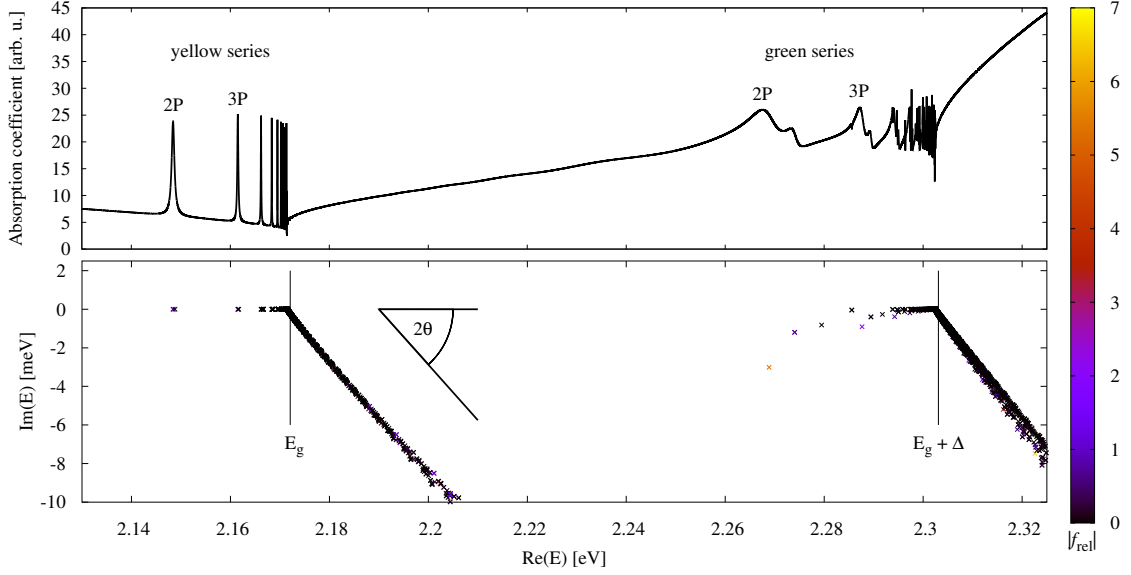


Figure 8.2.: Spectrum and resonance positions in the complex plane for the yellow and green exciton series of Cu_2O . Note that only the odd parity states are included. The color bar shows the absolute value of the relative oscillator strength $|f_{\text{rel}}|$. As coupling with phonons is not considered here, the linewidths of the yellow exciton states in the upper panel were put in by hand, as explained in the text. The vertical lines mark the respective band gaps. Due to the finite basis, the numerical resonance positions are already rotated into the lower complex plane at a slightly lower energies. The absorption coefficient is given in arbitrary units and with an arbitrary shift of the base line.

derived from the approximate Rydberg formula [30, 74] with $E_{\text{Ryd}} = 92 \text{ meV}$ and $\delta_{\text{P}} = 0.23$.

The green exciton states, however, are true resonances even apart from phonons, since they are coupled to the yellow continuum by the valence band structure. The linewidths visible in the upper part of Fig. 8.2 are solely due to this effect. The continuum states of both the yellow and green excitons provide for a square root function shaped background starting at energies above the respective band edges.

We now want to discuss the classification and symmetries of resonances of the green exciton series. The green excitons are defined by the condition $J = 3/2$. Additionally, we have to consider the angular momentum L . The electron spin plays no role for the odd states and remains a good quantum number. Thus, for the P states we have $F = 1/2, 3/2$, and $5/2$. Reducing the symmetry to the octahedral group O_h , the irreducible representations are Γ_6^- , Γ_8^- , and $\Gamma_7^- \oplus \Gamma_8^-$, respectively [76]. We have to take into account, however, that the quasispin \mathbf{I} transforms according to Γ_5^+ instead of Γ_4^+ . Since $\Gamma_5^+ =$

$\Gamma_4^+ \otimes \Gamma_2^+$, this can be done by performing the coupling of angular momenta as usual, but multiplying by Γ_2^+ in the end. For the P states, we thus have the representations Γ_6^- , Γ_8^- , Γ_7^- , and Γ_8^- . Note that the degeneracy of these states is doubled due to the electron spin. Since half-integer angular momenta only have the above mentioned irreducible representations in O_h [76], all states considered in this work can be classified according to them. Of those, only Γ_6^- and Γ_8^- states are dipole active, because only those contain Γ_4^- when multiplied with the electron spin symmetry Γ_6^+ [76]. Additional consideration of the degree of degeneracy then allows for the unique assignment of irreducible representations to the odd exciton states as given in Appendix B.

In Table 8.1 and in Fig. 8.3 on the left the resonance positions of the dominant P states are presented. We extract the band gap, Rydberg constant and quantum defect using a fit of the form $E(n) = E_{g,\text{green}} - E_{\text{Ryd}}^{\text{gr}}/(n - \delta)^2$. As expected, the fitted continuum threshold $E_{g,\text{green}}^{\text{fit}} = 2.30302 \text{ eV}$ shows excellent agreement with the band gap of the green excitons $E_g + \Delta = 2.30308 \text{ eV}$. For the Rydberg constant we obtain $E_{\text{Ryd}}^{\text{gr}} = 150.4 \text{ meV}$, which is in good agreement with literature [60, 147, 150, 151]. In previous theoretical work by Schöne *et al.* [150], the quantum defect of the green exciton series was investigated using a simplified treatment of the valence band dispersion neglecting the coupling of the green resonances to the yellow continuum, yielding negative quantum defects, which for the P states are in reasonable agreement with our result of $\delta = -0.112$. In Fig. 8.3 we also present a fit without using a quantum defect. Detailed comparison shows that this fit is slightly less accurate, especially for low principal quantum numbers. This motivates the

Table 8.1.: Numerically determined resonance positions of some of the lowest P states belonging to the irreducible representation Γ_6^- . The selected states produce the dominant peak of each n -manifold in the absorption spectrum.

State	Re E [eV]	Im E [meV]	Re f_{rel}	Im f_{rel}
2P	2.26887	-3.01965	4.2998	5.8604
3P	2.28765	-0.90691	1.1603	1.8982
4P	2.29423	-0.38575	0.5028	0.8270
5P	2.29731	-0.19095	0.2571	0.4496
6P	2.29901	-0.10700	0.1337	0.2630
7P	2.30005	-0.06821	0.1416	0.1579
8P	2.30072	-0.04328	0.0519	0.1085
9P	2.30120	-0.03314	0.0438	0.0730
10P	2.30154	-0.02334	0.0302	0.0550
11P	2.30180	-0.01733	0.0268	0.0387
12P	2.30199	-0.01459	0.0198	0.0322
13P	2.30215	-0.01012	0.0168	0.0223
14P	2.30227	-0.00903	0.0118	0.0212
15P	2.30237	-0.00742	0.0105	0.0165

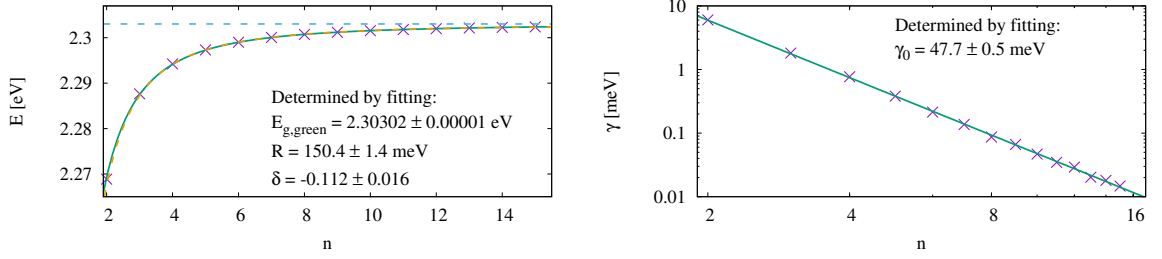


Figure 8.3.: *Left*: Numerically determined energies of the lowest dominant P states. The band gap energy $E_{g,green}$, Rydberg constant R , and quantum defect δ are determined by a fit (green solid line). For comparison, the dashed yellow line shows a fit without quantum defect (see text). *Right*: The numerically determined yellow-continuum induced linewidths of the dominant green P states. A fit using the function $\gamma_n = \gamma_0 n^{-3}$ is in good agreement with the numerical data.

validity of the quantum-defect corrected Rydberg formula also for the dominant P states of the green exciton series. A more complete version of Table 8.1 is given in Appendix B, where we assign quantum numbers to all odd parity states.

The green exciton series has already been experimentally investigated in Ref. [9]. At temperature $T = 4.2$ K Gross found $E_{2P} = 2.266$ eV, $E_{3P} = 2.287$ eV, $E_{4P} = 2.294$ eV and $E_{5P} = 2.298$ eV, which agrees with the numerical energies given in Table 8.1 to within approximately 1 - 2 meV.

The behavior of the linewidths of the green excitons induced by the coupling to the yellow continuum as a function of the principal quantum number is shown on the right in Fig. 8.3. A function of the form $\gamma_n = \gamma_0 n^{-3}$ provides a good fit to the numerically determined values. We obtain $\gamma_0 = 47.7$ meV, which means that the yellow-continuum induced linewidths of the dominant green P states are large compared to the phonon-coupling induced linewidths of the yellow excitons given in Eq. (8.10). Assuming that the phonon-coupling leads to similar linewidths for both the yellow and green excitons, the widths of the green excitons shown in Fig. 8.2 would only slightly increase when taking phonon-coupling into account, however, a more detailed theory of the phonons or precise state-of-the-art experimental data are necessary to clarify this point.

8.3

The spectrum of even-parity green excitons

In this section, we now want to extend our results to the case of the even-parity states, like the S and D states. We start by exploring the general level-structure of the even-

parity multiplets.

8.3.1 Classification of the even parity states of the green series

We want to understand the structure of the even green exciton spectrum and identify the involved irreducible representations. We begin by discussing the situation in the hydrogenlike model without the central-cell corrections and especially the exchange interaction. In this case the electron spin \mathbf{S}_e does not appear in the Hamiltonian and $\mathbf{F} = \mathbf{J} + \mathbf{L}$ is a good quantum number, taking half-integer values. In a model with spherical symmetry $O(3)$, the states of the spectrum can then be classified according to F and its z -component M_F .

Introducing the band-structure term reduces the symmetry to the cubic group O_h . Even parity states with a half-integer spin can only have three irreducible representations, which are Γ_6^+ , Γ_7^+ , and Γ_8^+ [76].

Finally adding in the central-cell corrections and especially the exchange interaction, we have to consider the product representations of Γ_6^+ , Γ_7^+ , and Γ_8^+ with the representation Γ_6^+ of the electron. They are given by [76]:

$$\begin{aligned}\Gamma_6^+ \otimes \Gamma_6^+ &= (\Gamma_1^+ \oplus \Gamma_4^+) \\ \Gamma_7^+ \otimes \Gamma_6^+ &= (\Gamma_2^+ \oplus \Gamma_5^+) \\ \Gamma_8^+ \otimes \Gamma_6^+ &= (\Gamma_3^+ \oplus \Gamma_4^+) \oplus \Gamma_5^+.\end{aligned}\tag{8.12}$$

The exchange interaction only acts upon states with an S admixture. Representations in brackets thus remain approximately degenerate as explained in the following. For the green series the S states have $L = 0$ and $J = 3/2$, leading to $F = 3/2$ and thus to the representation Γ_8^+ . The exchange interaction then causes a splitting between the threefold-degenerate Γ_5^+ subspace and the fivefold-degenerate $\Gamma_3^+ \oplus \Gamma_4^+$ subspace, lifting the former above the latter. States with small S admixtures effectively retain their eightfold-degeneracy. Since only Γ_8^+ states can have a green S admixture, the $\Gamma_6^+ \otimes \Gamma_6^+ = \Gamma_1^+ \oplus \Gamma_4^+$ and $\Gamma_7^+ \otimes \Gamma_6^+ = \Gamma_2^+ \oplus \Gamma_5^+$ spaces remain approximately fourfold degenerate; they additionally can have no significant two-photon oscillator strengths. They can, on the other hand, couple to yellow S states. The yellow admixtures are quite small for large parts of the spectrum, as we will see further below, so this does not change the previous conclusions by much.

Let D_F denote the irreducible representation of O_h belonging to the angular momentum F . With those, the irreducible representations of the lowest even parity states of the green series are as follows:

$$\begin{aligned}\text{S states } (L = 0) : \quad & D_{3/2} \otimes \Gamma_2^+ \quad \rightarrow \quad \Gamma_8^+, \\ \text{D states } (L = 2) : \quad & (D_{1/2} \oplus \cdots \oplus D_{7/2}) \otimes \Gamma_2^+ \quad \rightarrow \quad 2\Gamma_6^+ \oplus 2\Gamma_7^+ \oplus 3\Gamma_8^+, \\ \text{G states } (L = 4) : \quad & (D_{1/2} \oplus \cdots \oplus D_{11/2}) \otimes \Gamma_2^+ \quad \rightarrow \quad 3\Gamma_6^+ \oplus 4\Gamma_7^+ \oplus 7\Gamma_8^+.\end{aligned}$$

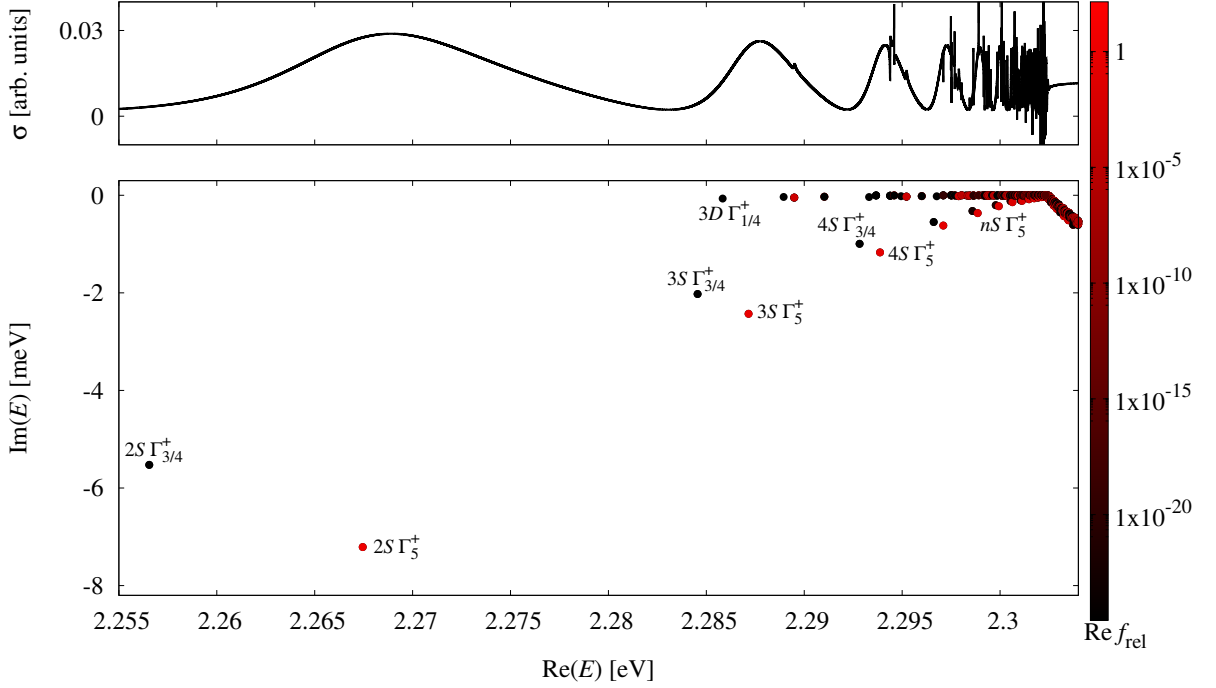


Figure 8.4.: Resonance positions of the green even exciton series in the complex plane and the corresponding spectrum when taking the central-cell corrections into account. The color bar gives the relative two-photon oscillator strength in arbitrary units.

The multiplication by Γ_2^+ is necessary because the quasispin states transform according to $\Gamma_5^+ = \Gamma_4^+ \otimes \Gamma_2^+$. This allows us to perform the usual coupling of angular momenta and only multiplying by Γ_2^+ in the end. Equations (8.12) can then be used to deduce the level structure.

8.3.2 Two-photon absorption spectra of green excitons

We first of all show the numerically simulated even exciton spectrum with the influence of the central-cell corrections in Fig. 8.4. We can see that the spectrum is dominated by a series of states with especially strong two-photon absorption and large linewidths. Since the strength of two-photon absorption processes is determined by the admixture of $L = 0$ to the envelope function of the excitons, it is reasonable to conclude that those are indeed S states. We confirm this by calculating the admixture of different angular momenta to the obtained states in Appendix B. The corresponding complex energies as a function of the principal quantum number are listed in Table 8.2. More data on the resonances and their quantum numbers, including all even parity states up to the 6S exciton is given in Table B.2.

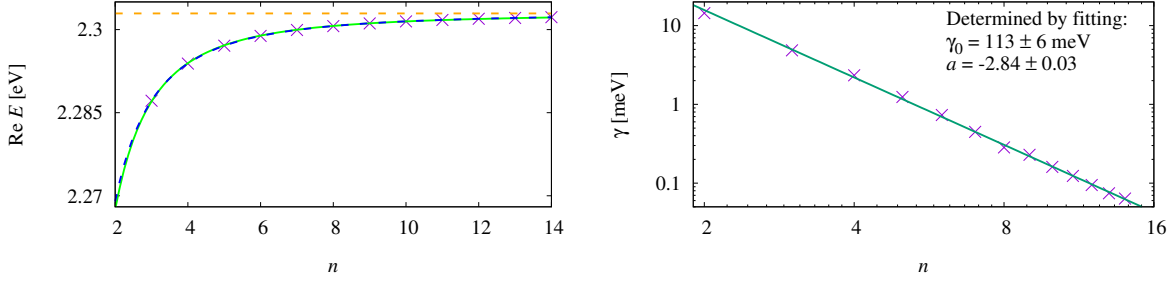


Figure 8.5.: *Left*: Real parts of the energies of the two-photon active green S excitons as a function of the principal quantum number. We perform a fit to obtain the gap energy E_{gap} , Rydberg energy E_{Ryd} and quantum defect δ_S once over the whole range of n (solid green line) and once for $n \geq 3$ (dashed blue line). The fitted values are given in the text. *Right*: Linewidths γ of the green S excitons as a function of the principal quantum number n . We perform a fit to obtain the parameters γ_0 and a in $\gamma = \gamma_0 n^a$.

The left-hand side of Fig. 8.5 shows the numerically determined energies of the dominant green S states as a function of the principal quantum number. We perform a fit of the form

$$E(n) = E_{\text{gap}} - \frac{E_{\text{Ryd}}}{(n - \delta_S)^2}. \quad (8.13)$$

Table 8.2.: Numerically determined energies and relative oscillator strengths for the dominant S peaks in the spectrum. We additionally list the exchange splittings in the last column.

n	Re E [eV]	Im E [meV]	Re f_{rel} [a.u.]	Im f_{rel} [a.u.]	Δ^{Ex} [meV]
2	2.26745	-7.210	2.413	-1.279	10.90
3	2.28716	-2.429	0.762	-0.537	2.60
4	2.29387	-1.170	0.355	-0.296	1.04
5	2.29710	-0.621	0.187	-0.165	0.49
6	2.29886	-0.366	0.108	-0.103	0.27
7	2.29994	-0.224	0.068	-0.064	0.15
8	2.30063	-0.142	0.041	-0.050	0.10
9	2.30112	-0.114	0.033	-0.036	0.07
10	2.30148	-0.080	0.022	-0.026	0.05
11	2.30174	-0.062	0.018	-0.021	0.03
12	2.30195	-0.047	0.014	-0.015	0.02
13	2.30211	-0.037	0.011	-0.012	0.02
14	2.30224	-0.032	0.009	-0.010	0.01

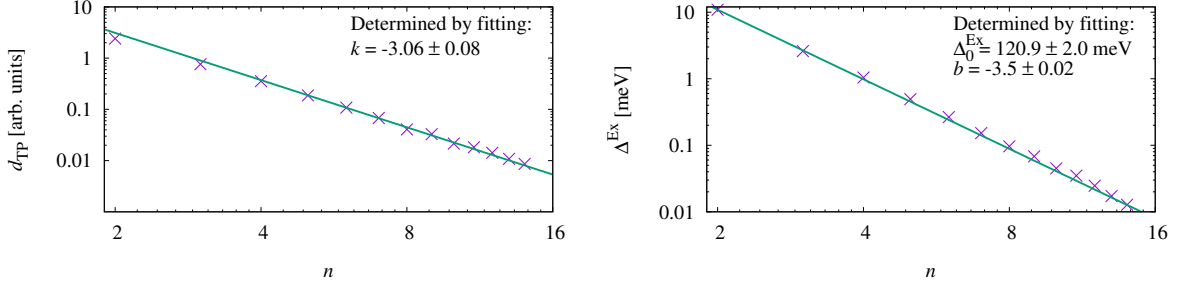


Figure 8.6.: *Left*: Two-photon oscillator strengths d_{TP} for polarization $\mathbf{E}^1 \parallel \mathbf{E}^2 \parallel [110]$ of two-photon active green S excitons as a function of the principal quantum number. We perform a fit for $n \geq 6$ to obtain the exponent k in the formula $d = d_0 n^k$ for large quantum numbers. *Right*: Exchange splitting of the green S excitons as a function of the principal quantum number. We perform a fit to obtain the parameters Δ_0^{Ex} and b in $\Delta^{\text{Ex}} = \Delta_0^{\text{Ex}} n^b$.

The fitted gap energy $E_{\text{gap}} = 2.30293 \pm 0.00003$ eV approximately agrees with the sum of the yellow gap energy and the spin-orbit coupling $E_g + \Delta = 2.30308$ eV. For the Rydberg energy of the green 1S series, we obtain $E_{\text{Ryd}} = 146 \pm 2$ meV and the quantum defect $\delta_S = -0.03 \pm 0.01$. These values significantly deviate from the values obtained for the green P excitons in Ref. [146] and from the quantum defects calculated in Ref. [150]. A plausible explanation for this is the influence of the central-cell corrections, which mostly affect states of small radii. To account for this, we repeat the fit over the restricted range of principal quantum numbers $n \geq 3$. We obtain values $E_{\text{gap}}^{n \geq 3} = 2.30302 \pm 0.00001$ eV, $E_{\text{Ryd}}^{n \geq 3} = 157 \pm 1$ meV and $\delta^{n \geq 3} = -0.15 \pm 0.01$. The quantum defect is more in line with the values obtained by Schöne *et al.* in Ref. [150].

We investigate the linewidths $\gamma = -2 \text{Im}E$ of the prominent even S excitons and their behavior as a function of n . On the right-hand side in Fig. 8.5 we present the numerically determined values in a log-log-plot. We fit a function of the form

$$\gamma(n) = \gamma_0 n^a \quad (8.14)$$

to the data. We obtain $\gamma_0 = 113$ meV and $a = -2.84$. There is a significant deviation from a decrease with the third power of the principal quantum number n^{-3} . The parameter γ_0 is significantly greater than the value determined for the green P states $\gamma_0^P = 47.7$ meV in Ref. [146].

In Fig. 8.6 on the left, we show the relative two-photon oscillator strength of the strongest S states as a function of the principal quantum number n . Our fit of the form

$$d(n) = d_0 n^k \quad (8.15)$$

reveals that the oscillator strength decreases with the third power of n for large principal quantum numbers. The same behavior has been experimentally observed for the P states in the yellow series [30].

8.3.3 Exchange splitting of the even exciton states

In Chapter 3, we investigated various features of the exchange splitting in the yellow series. We can augment this discussion here with the values of the exchange splittings for the green states with $n \geq 2$ given in the last column in Table 8.2. We additionally plot the exchange splitting as a function of the principal quantum number n in Fig. 8.6 on the right and perform a fit of the form $\Delta^{\text{Ex}} = \Delta_0^{\text{Ex}} n^b$. The results are $\Delta_0^{\text{Ex}} = 129.4$ meV and $b = -3.5$. Extrapolating this to $n = 1$ leads to a significantly stronger splitting than experimentally observed [63], indicating that the behavior of the higher-lying green resonances differs from the behavior of the bound $n = 1$ state in this respect. According to our calculation, the coupling to the yellow continuum plays an important role here. A quick diagonalization of the Hamiltonian in the reduced Hilbert space of states with $J = 3/2$ for example leads to a splitting of the green 2S states of $\Delta E \approx 2.8$ meV, which is much more in line with the result for $n = 1$. Some further numerical calculations show that the increased splitting for the resonances with $n \geq 2$ is already present in degenerate perturbation theory, showing that it is not primarily due to mutual level shifts caused by the exchange interaction between different principal quantum numbers or between the green and yellow series in general. Rather, our calculations indicate that the coupling to the yellow series and the complex rotation actually lead to an amplification of the wave function at the origin for the involved green S states, causing a stronger exchange interaction.

Table 8.2 shows no case of a reversal of ortho- and paraexciton as the one discussed in Chapter 3 for the yellow states.

With this, we conclude the chapter on the calculation of the green exciton resonances and their general discussion. We implemented the complex-coordinate-rotation method to calculate the complex energies of states lying in the yellow continuum and simulated spectra of optical transitions from the crystal ground state. In Chapter 9, we use the insights obtained here as a basis for the investigation of interseries transitions between the yellow and green series.

9

Interseries dipole transitions from yellow to green excitons

After having introduced the series of green exciton resonances in cuprous oxide in Chapter 8, we now want to study interseries dipole transitions between the yellow and green exciton series including the complex valence band structure. To this end, we extend previous studies of the spectrum of complex green exciton resonances presented in Chapter 8 to optical transitions between different exciton states in addition to transitions from the crystal ground state. This allows us to augment previous calculations on interseries transitions using a hydrogenlike model [66] by a more comprehensive treatment of the valence band structure. The analytical and numerical results discussed in this chapter are published in Ref. [152].

Cuprous oxide offers a wide variety of possibilities of probing exciton physics and studying the influence of band structure effects. This is underlined by the fact that excitons were first observed in cuprous oxide [8, 9], and that resonances with principal quantum number of up to $n = 25$ have been experimentally detected [30]. Most of the work in the literature focuses on the yellow series, which is formed by electrons in the lowest Γ_6^+ conduction band and holes in the uppermost Γ_7^+ valence band [33, 35, 153]. The green excitons, on the other hand, are formed by holes in the Γ_8^+ valence band [51, 147, 148]. For principal quantum numbers $n \geq 2$, they are located at energies above the band gap of the yellow excitons, and couple to the yellow continuum states. Thus, even without taking phonon coupling into account, the green excitons above the yellow band gap are no longer bound states with infinite lifetimes, but quasibound resonances with finite lifetimes. We calculated the locations of the green exciton resonances [146] using the complex-scaling method [93, 94] in Chapter 8.

Motivated by the aim to identify promising experimentally accessible dipole transitions for the coherent manipulation of Rydberg excitons [154, 155] and the generation of giant optical nonlinearities [156], interseries transitions between the yellow and green, respectively yellow and blue, exciton series have been investigated using a hydrogenlike

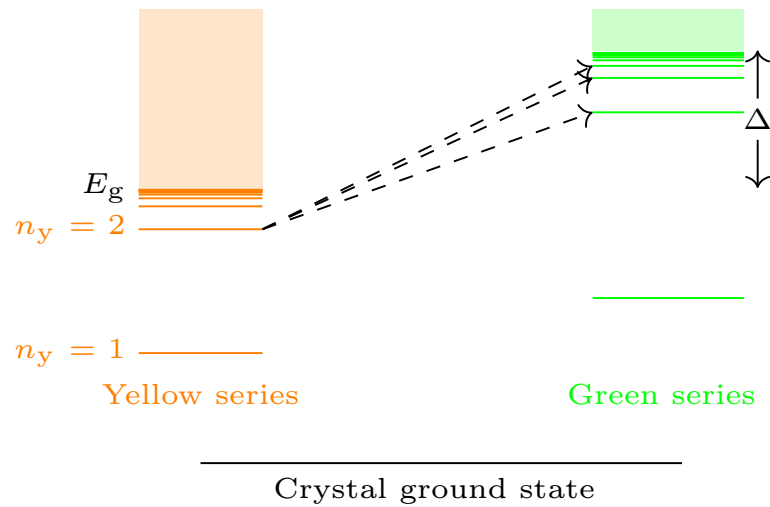


Figure 9.1.: We investigate dipole transitions from the yellow to the green series, here illustrated with the case of transitions from the yellow $n = 2$ excitons to some of the green resonances inside the yellow continuum.

model for the exciton interaction [66]. The interseries transitions, i.e., those between different exciton series, provide for more accessible interrogation wavelengths than transitions within a single exciton series, and thus offer a distinct advantage. Thus, while transition wavelengths between adjacent Rydberg states within the same series scale as n^3 and quickly approach the millimeter range, the wavelength limit for interseries transitions is set by the energy gap between bands, which are typically in the near- to mid IR. Here, we investigate interseries dipole transitions between the yellow and green exciton series, while taking into account the complex structure of the valence band [35, 86] as well as central-cell corrections [11, 38, 60, 79, 80]. As our focus is not on optical transitions where the exciton is created from the crystal ground state, but rather on transitions between different exciton states, this requires extensive modifications of the scheme for calculating the oscillator strengths.

The chapter is organized as follows. First, we derive the dipole transition matrix elements in Sec. 9.1 using the calculated eigenvalues and eigenvectors, and then, in Sec. 9.3, we present and discuss our results on interseries dipole transitions and absorption spectra.

9.1 Dipole transitions between excitonic states

In the following, we investigate dipole transitions between different exciton states as illustrated in Fig. 9.1, which is in contrast to earlier work that focused mostly on transitions from the crystal ground state [35, 38, 146]. The central quantity describing the transition from an initial exciton state $|\Psi_i\rangle$ to the final exciton state $|\Psi_f\rangle$ is the transition matrix element

$$M_{\text{fi}} = \langle \Psi_f | \hat{\mathbf{e}}_A \cdot \boldsymbol{\pi} | \Psi_i \rangle \quad (9.1)$$

of the single-photon transition operator, with the polarization direction $\hat{\mathbf{e}}_A$ of the vector potential associated with the photon field

$$\mathbf{A}(\mathbf{x}) = \mathbf{A}_0 e^{i\boldsymbol{\kappa} \cdot \mathbf{x}} \approx \mathbf{A}_0 = A_0 \hat{\mathbf{e}}_A \quad (9.2)$$

in dipole approximation, where we assume that the momentum $\hbar\boldsymbol{\kappa}$ of the photon is much smaller than the relative momentum of exciton and hole. The operator

$$\boldsymbol{\pi} = m_0 \mathbf{v} = m_0 \frac{\partial \mathbf{x}}{\partial t} = \frac{im_0}{\hbar} [\mathcal{H}, \mathbf{x}] \quad (9.3)$$

denotes the kinetic momentum operator in a crystal with spin-orbit interaction, and appears during the minimal-substitution procedure. Note that it differs from the quasi-momentum \mathbf{p} associated with the Bloch eigenfunctions of the band Hamiltonian \mathcal{H} . The position operator \mathbf{x} also has to be distinguished from the coordinates \mathbf{r}_e and \mathbf{r}_h that arise from the lattice positions in the continuum description of the crystal.

For the interseries transitions discussed in this chapter, $|\Psi_i\rangle$ is mostly a bound yellow exciton state and $|\Psi_f\rangle$ is an unbound green exciton resonance. It is therefore sufficient to consider the matrix elements in a basis, e.g., with the basis states (2.29); the transition amplitudes for the eigenstates can then be obtained by forming appropriate superpositions,

$$M_{\text{fi}} = \sum_{\Pi', \Pi} c_{\Pi'}^f c_{\Pi}^i \langle \Pi' | \hat{\mathbf{e}}_A \cdot \boldsymbol{\pi} | \Pi \rangle. \quad (9.4)$$

Note that the coefficients for the left (bra vector) basis states are not complex conjugated, since they would be real valued without the complex-coordinate rotation.

9.1.1 Operator identity between kinetic momentum and derivatives of the band Hamiltonian

We will now derive an operator identity between the kinetic momentum $\boldsymbol{\pi}$ and the derivatives of the band Hamiltonian $H(\mathbf{p})$ with respect to the momenta. For that,

we consider arbitrary single exciton states, which are effective two-particle states of an electron with spin $\mathbf{S}_{e,z} = \sigma_e$ in the conduction band (c) and a hole with effective hole spin $\mathbf{J}_{h,z} = \sigma_h$ in the valence band (v). An excitonic state with center-of-mass momentum \mathbf{P} can then be written as

$$|\Psi_{\tau, \mathbf{P}}^{c,v}\rangle = \sum_{\mathbf{p}} \phi_{\tau, \mathbf{P}}(\mathbf{p}) a_{c, \sigma_e, \mathbf{p} + \alpha_e \mathbf{P}}^\dagger b_{v, \sigma_h, -\mathbf{p} + \alpha_h \mathbf{P}}^\dagger |\Psi_0\rangle \quad (9.5)$$

where we use the shorthand notation $\tau = \{N, L, M, \sigma_e, \sigma_h\}$ for the additional quantum numbers of the exciton. The operators $a_{c, \sigma_e, \mathbf{q}}^\dagger$ ($b_{v, \sigma_h, \mathbf{q}}^\dagger$) are electron (hole) creation operator and $|\Psi_0\rangle$ is the crystal ground state. The center-of-mass transformation leads to the coefficients α_e and α_h , with $\alpha_e + \alpha_h = 1$. We have chosen the same coefficients for all states.

Dipole approximation

Consequent to the dipole approximation, the center-of-mass momentum \mathbf{P} of the exciton vanishes and the exciton state can be written as

$$|\Psi_{\tau}^{c,v}\rangle = \sum_{\mathbf{p}} \phi_{\tau}(\mathbf{p}) a_{c, \sigma_e, \mathbf{p}}^\dagger b_{v, \sigma_h, -\mathbf{p}}^\dagger |\Psi_0\rangle. \quad (9.6)$$

In the one-exciton Hilbert space spanned by the states (9.6), we express the single-photon transition operator in second quantization. Using the dipole approximation, we obtain

$$\begin{aligned} \frac{e\mathbf{A}_0\boldsymbol{\pi}}{m_0} &= \frac{e\mathbf{A}_0}{m_0} \sum_{\nu, \nu'} \sum_{\sigma_e, \sigma'_e} \sum_{\mathbf{q}} \langle \nu, \sigma_e, \mathbf{q} | \boldsymbol{\pi} | \nu', \sigma'_e, \mathbf{q} \rangle a_{\nu, \sigma_e, \mathbf{q}}^\dagger a_{\nu', \sigma'_e, \mathbf{q}} \\ &+ \frac{e\mathbf{A}_0}{m_0} \sum_{\xi, \xi'} \sum_{\sigma_h, \sigma'_h} \sum_{\mathbf{q}} \langle \xi, \sigma_h, \mathbf{q} | \boldsymbol{\pi} | \xi', \sigma'_h, \mathbf{q} \rangle b_{\xi, \sigma_h, \mathbf{q}}^\dagger b_{\xi', \sigma'_h, \mathbf{q}} \end{aligned} \quad (9.7)$$

with the vector potential \mathbf{A}_0 according to Eq. (9.2), the conduction band indices ν, ν' , the valence band indices ξ, ξ' and the corresponding substates (spins) $\sigma_{e/h}$. We use the radiation gauge and ignore the diamagnetic term, as it only has an appreciable influence for very high field strengths of the incoming electromagnetic wave. Calculation of a matrix element like $e\mathbf{A}_0 \langle \Psi_{\tau}^{c,v} | \boldsymbol{\pi} | \Psi_{\tau'}^{c',v'} \rangle / m_0$, leads to four cases, which we consider in the following.

(i) Intraseres transitions: Here, we have $\{c, \sigma_e\} = \{c', \sigma'_e\}$ and $\{v, \sigma_h\} = \{v', \sigma'_h\}$. With the fermionic anti-commutation rules for the creation and annihilation operators, we obtain

$$\langle \Psi_{\tau}^{c,v} | \boldsymbol{\pi} | \Psi_{\tau'}^{c,v} \rangle = \sum_{\mathbf{p}} \phi_{\tau'}(\mathbf{p}) \phi_{\tau}^\dagger(\mathbf{p}) \times (\langle c, \sigma_e, \mathbf{p} | \boldsymbol{\pi} | c, \sigma_e, \mathbf{p} \rangle + \langle v, \sigma_h, -\mathbf{p} | \boldsymbol{\pi} | v, \sigma_h, -\mathbf{p} \rangle). \quad (9.8)$$

(ii) Hole-driven interseries transitions: In this case, we have $\{c, \sigma_e\} = \{c', \sigma'_e\}$ but $\{v, \sigma_h\} \neq \{v', \sigma'_h\}$. Here, we calculate

$$\left\langle \Psi_{\tau}^{c,v} | \boldsymbol{\pi} | \Psi_{\tau'}^{c',v'} \right\rangle = \sum_{\mathbf{p}} \phi_{\tau'}(\mathbf{p}) \phi_{\tau}^{\dagger}(\mathbf{p}) \langle v, \sigma_h, -\mathbf{p} | \boldsymbol{\pi} | v', \sigma'_h, -\mathbf{p} \rangle. \quad (9.9)$$

(iii) Electron-driven interseries transitions: Here, we have $\{c, \sigma_e\} \neq \{c', \sigma'_e\}$ but $\{v, \sigma_h\} = \{v', \sigma'_h\}$. In this case, we arrive at

$$\left\langle \Psi_{\tau}^{c,v} | \boldsymbol{\pi} | \Psi_{\tau'}^{c',v} \right\rangle = \sum_{\mathbf{p}} \phi_{\tau'}(\mathbf{p}) \phi_{\tau}^{\dagger}(\mathbf{p}) \langle c, \sigma_e, \mathbf{p} | \boldsymbol{\pi} | c', \sigma'_e, \mathbf{p} \rangle. \quad (9.10)$$

(iv) Two-particle transitions: In this case, one has $\{c, \sigma_e\} \neq \{c', \sigma'_e\}$ and $\{v, \sigma_h\} \neq \{v', \sigma'_h\}$. We will not discuss this case, since it is forbidden in single-photon transitions.

Transitions from the yellow to the green series in Cu_2O are predominantly driven by a transition of the hole from the Γ_7^+ to the Γ_8^+ valence band, that is, they are mostly hole-driven.

Bloch matrix elements

We can use the relation $|n, \sigma, \mathbf{p}\rangle = e^{i\mathbf{p}\mathbf{r}} |u_{n,\sigma}, \mathbf{p}\rangle$ between the Bloch states and the lattice periodic functions $|u_{n,\sigma}, \mathbf{p}\rangle$ to rewrite the interband matrix elements,

$$\langle n, \sigma, \mathbf{p} | \boldsymbol{\pi} | n', \sigma', \mathbf{p} \rangle = \langle u_{n,\sigma}, \mathbf{p} | \boldsymbol{\pi} | u_{n',\sigma'}, \mathbf{p} \rangle + \mathbf{p} \delta_{nn'} \delta_{\sigma\sigma'}. \quad (9.11)$$

We denote the bands by n, n' and the associated spins by σ, σ' .

The Hamiltonian acting in the space of the lattice periodic functions is the $\mathbf{p} \cdot \boldsymbol{\pi}$ -Hamiltonian (In the literature, it is often also known as the $\mathbf{k} \cdot \boldsymbol{\pi}$ -Hamiltonian with $\mathbf{k} = \mathbf{p}/\hbar$)

$$\mathcal{H}_{\mathbf{p} \cdot \boldsymbol{\pi}} = \mathcal{H}_0 + \mathcal{H}_{\mathbf{p}}, \quad (9.12)$$

with

$$\begin{aligned} \mathcal{H}_0 &= -\frac{\hbar^2 \nabla^2}{2m_0} + V(\mathbf{x}) - \frac{i\hbar^2}{4m_0^2 c^2} (\boldsymbol{\sigma} \times \nabla V(\mathbf{x})) \cdot \nabla, \\ \mathcal{H}_{\mathbf{p}} &= \frac{\mathbf{p}}{m_0} \cdot \boldsymbol{\pi} + \frac{\mathbf{p}^2}{2m_0}. \end{aligned} \quad (9.13)$$

Here, \mathcal{H}_0 denotes the Hamiltonian at the Γ -point, which is determined by the lattice periodic potential $V(\mathbf{x})$. $\boldsymbol{\sigma}$ is an abbreviation for the vector of Pauli matrices.

We obtain the relation

$$\boldsymbol{\pi} = m_0 \mathbf{v} = m_0 \frac{\partial \mathcal{H}_{\mathbf{p} \cdot \boldsymbol{\pi}}}{\partial \mathbf{p}} - \mathbf{p}, \quad (9.14)$$

and consequently arrive at

$$\langle n, \sigma, \mathbf{p} | \boldsymbol{\pi} | n', \sigma', \mathbf{p} \rangle = m_0 \left\langle u_{n, \sigma}, \mathbf{p} \left| \frac{\partial \mathcal{H}_{\mathbf{p} \cdot \boldsymbol{\pi}}}{\partial \mathbf{p}} \right| u_{n', \sigma'}, \mathbf{p} \right\rangle. \quad (9.15)$$

The perturbation theoretical analysis of Eq. (9.15) was performed in Ref. [66] up to first order in \mathbf{p} , resulting in

$$\langle n, \sigma, \mathbf{p} | \boldsymbol{\pi} | n', \sigma', \mathbf{p} \rangle = m_0 \left\langle u_{n, \sigma}, 0 \left| \frac{\partial \mathcal{H}_{\mathbf{p} \cdot \boldsymbol{\pi}}}{\partial \mathbf{p}} \right| u_{n', \sigma'}, 0 \right\rangle. \quad (9.16)$$

The $\mathbf{p} \cdot \boldsymbol{\pi}$ Hamiltonian $\mathcal{H}_{\mathbf{p} \cdot \boldsymbol{\pi}}$ describes the \mathbf{p} -dependent band dispersion in the crystal. In our system, this is identified with the kinetic energies of the electron in the conduction band H_c and hole in the valence band H_v respectively. Using the kinetic part of the Hamiltonian (2.2),

$$T(\mathbf{p}) = H_c(\mathbf{p}) - H_v(\mathbf{p}) = \frac{\gamma'_1}{2m_0} \mathbf{p}^2 + H_b(\mathbf{p}), \quad (9.17)$$

we can summarize all three cases in Eqs. (9.8)-(9.10) via

$$\begin{aligned} \langle \Psi_{\tau}^{c, v} | \boldsymbol{\pi} | \Psi_{\tau'}^{c, v'} \rangle &= m_0 \sum_{\mathbf{p}} \phi_{\tau}^{\dagger}(\mathbf{p}) \phi_{\tau'}(\mathbf{p}) \langle c, \sigma_e, v, \sigma_h | \partial_{\mathbf{p}} T(\mathbf{p}) | c, \sigma'_e, v', \sigma'_h \rangle \\ &= m_0 \int d^3 \mathbf{r} \psi_{\tau}^{\dagger}(\mathbf{r}) \underbrace{\langle c, \sigma_e, v, \sigma_h | \partial_{\mathbf{p}} T(\mathbf{p}) | c, \sigma'_e, v', \sigma'_h \rangle}_{\mathcal{O}(\mathbf{p})} \psi_{\tau'}(\mathbf{r}), \end{aligned} \quad (9.18)$$

where the matrix element is evaluated in the twelve-dimensional basis of electron-hole spin-states $|c, \sigma_e, v, \sigma_h\rangle$. In the second line, we use the real-space envelope function $\psi_{\tau}(\mathbf{r})$ of the state $|\Psi_{\tau'}^{c, v'}\rangle$ to express the integral in real space. These states span the same Hilbert space as the basis states (2.29).

Noting that only the kinetic energy terms in the Hamiltonian (2.2) contain the relative momentum operator $\boldsymbol{\pi}$, we obtain the identity

$$\boldsymbol{\pi} = m_0 \frac{\partial}{\partial \mathbf{p}} H(\mathbf{p}) \quad (9.19)$$

valid for the one-exciton states considered in this chapter. Equation (9.19) is an operator identity in the one-exciton Hilbert space spanned, e.g., by the basis (2.29), and is valid for vanishing center-of-mass momentum \mathbf{P} and relative momentum \mathbf{p} much smaller than the extent of the Brillouin zone.

9.1.2 Numerical evaluation of the matrix elements $\langle \Pi' | \pi_z | \Pi \rangle$

The computation of the dipole transition matrix elements M_{fi} in Eq. (9.4) requires one to evaluate the matrix elements $\langle \Pi' | \boldsymbol{\pi} | \Pi \rangle$ of the operator (9.19) in the basis (2.29).

From Eq. (9.19) we obtain

$$\frac{\boldsymbol{\pi}}{m_0} = \frac{\partial}{\partial \mathbf{p}} H(\mathbf{p}) = \frac{\gamma'_1 \mathbf{p}}{m_0} + \frac{\partial H_{\text{b}}(\mathbf{p})}{\partial \mathbf{p}}. \quad (9.20)$$

We focus on the component π_z for light polarized along the z -axis.

We first derive the matrix elements for p_z in the basis (2.29). In the formalism of irreducible tensors, p_z is given by

$$p_z = P_0^{(1)}. \quad (9.21)$$

In the supplemental material of Ref. [89], Eq. (14) provides the matrix elements for the operator

$$P_0^{(1)} \left(I^{(1)} \cdot S_{\text{h}}^{(1)} \right), \quad (9.22)$$

which we can use here. Using the identity

$$I^{(1)} \cdot S_{\text{h}}^{(1)} = \frac{1}{2} (\mathbf{J}^2 - \mathbf{I}^2 - \mathbf{S}_{\text{h}}^2) = \frac{2J(2J+2) - 11}{8}, \quad (9.23)$$

we can calculate the matrix element for p_z using

$$\langle \Pi' | P_0^{(1)} | \Pi \rangle = \frac{8}{2J(2J+2) - 11} \langle \Pi' | P_0^{(1)} \left(I^{(1)} \cdot S_{\text{h}}^{(1)} \right) | \Pi \rangle. \quad (9.24)$$

Here, $|\Pi\rangle$ and $|\Pi'\rangle$ denote basis states as given in Eq. (2.29).

The more difficult part is to evaluate the second term in Eq. (9.20). Instead of deriving the expression in detail here, we connect this problem to terms already calculated in Ref. [89]. They consider the Hamiltonian (2.2) in center-of-mass coordinates with a nonvanishing center-of-mass momentum $P = \hbar K$ parallel to a given axis. Here, we are interested in the case $\mathbf{P} \parallel [001]$ related to the derivative with respect to p_z . This means that we can set $\mathbf{P} = P \mathbf{e}_z$ in the following. Following Ref. [89], we expand the Hamiltonian in powers of P as

$$H(\mathbf{p}, \mathbf{P}) = H_0 + P H_1 + P^2 H_2. \quad (9.25)$$

The center-of-mass transformation (2.18) is chosen in such a way that terms linear in \mathbf{P} vanish without the corrections from the valence band. This means that the term H_1 arises solely from the kinetic energy H_{h} of the hole. More explicitly, we can write

$$H_{\text{h}}(\mathbf{p}_{\text{h}} = -\mathbf{p} + \alpha_{\text{h}} \mathbf{P}) = \frac{\mathbf{p}^2}{2m_{\text{h}}} + H_{\text{b}}(\mathbf{p}) - \frac{\alpha_{\text{h}} P}{m_{\text{h}}} p_z + P H_1 + \mathcal{O}(P^2), \quad (9.26)$$

where $\alpha_h = m_h/(m_h + m_e)$ is determined by the center-of-mass transformation. We first differentiate both sides with respect to $P = P_z$ and evaluate at $P = 0$,

$$\alpha_h \frac{\partial H_h}{\partial p_{h,z}}(\mathbf{p}_h = -\mathbf{p}) = -\alpha_h \frac{\partial H_h}{\partial p_z}(-\mathbf{p}) = -\frac{\alpha_h}{m_h} p_z + H_1. \quad (9.27)$$

On the other hand, first setting $P = 0$ and differentiating with respect to p_z leads to

$$\frac{\partial H_h}{\partial p_z}(-\mathbf{p}) = \frac{p_z}{m_h} + \frac{\partial H_b(\mathbf{p})}{\partial p_z}. \quad (9.28)$$

Comparing these results, we obtain the identity

$$\frac{\partial H_b}{\partial p_z}(\mathbf{p}) = -\frac{1}{\alpha_h} H_1 = -\frac{m_e \gamma'_1}{m_0} H_1. \quad (9.29)$$

Inserted into Eq. (9.20), we finally find

$$\pi_z = \gamma'_1 (p_z - m_e H_1), \quad (9.30)$$

with [89]

$$H_1 = -\frac{1}{2\hbar^2 m_e} \left\{ 2\sqrt{\frac{5}{3}} \mu' [P^{(1)} \times I^{(2)}]_0^{(1)} + 4\sqrt{\frac{2}{5}} \delta' [P^{(1)} \times I^{(2)}]_0^{(3)} \right\} \quad (9.31)$$

$$-\frac{3\eta_1}{\gamma'_1 \hbar^2 m_e} \left\{ \frac{2}{3} P_0^{(1)} (I^{(1)} \cdot S_h^{(1)}) + 2\sqrt{\frac{5}{3}} \nu [P^{(1)} \times D^{(2)}]_0^{(1)} + 4\sqrt{\frac{2}{5}} \tau [P^{(1)} \times D^{(2)}]_0^{(3)} \right\},$$

using the abbreviations

$$D_k^{(2)} = [I^{(1)} \times S_h^{(1)}]_k^{(2)} \quad (9.32)$$

and

$$\mu' = \frac{6\gamma_3 + 4\gamma_2}{5\gamma'_1}, \quad \delta' = \frac{\gamma_3 - \gamma_2}{\gamma'_1}, \quad \nu = \frac{6\eta_3 + 4\eta_2}{5\eta_1}, \quad \tau = \frac{\eta_3 - \eta_2}{\eta_1}. \quad (9.33)$$

All relevant matrix elements can be found in Ref. [89].

9.2 Non-Hermitian generalized eigenvalue problem

We first diagonalize the Hamiltonian (2.2) excluding the singular Dirac delta-terms V_d and H_{exch} of the central-cell corrections with the Haken potential (2.12). From the high-dimensional matrices, we are only interested in a small window of eigenstates. For this

aim an iterative method is implemented (e.g. in the ARPACK package [100]) that allows for the calculation of eigenvalues and eigenvectors near a controllable predetermined energy, which is numerically more efficient than a direct diagonalization.

After this, we set up a second eigenvalue problem where we include the delta-terms with only the converged eigenstates from the first diagonalization. For this, we diagonalize the entire resulting low-dimensional eigenvalue problem using a direct LAPACK method [99].

Having calculated the complex resonance energies and the associated eigenstates, we can use Eq. (9.19) and the corresponding matrix elements derived in Sec. 9.1 to simulate interseries dipole transition spectra.

9.3 Numerically calculated interseries transition strengths

In the following, we present our results for the dipole transition probabilities for two cases of interseries transitions. As parity is an exact quantum number, we separately discuss transitions first from odd parity to even parity states, and then from even parity to odd parity states. We choose a coordinate system where the x , y , and z axes are parallel to [100], [010], and [001] directions, respectively.

9.3.1 Interseries absorption spectra

The transition matrix elements $M_{\bar{f}i}$ can be used to calculate interseries absorption spectra. The photoabsorption cross section σ_i from the initial state $|\Psi_i\rangle$ at the spectral position $E = \hbar\omega_{\text{ph}}$ is given by [93, 144]

$$\sigma_i(\omega_{\text{ph}}) = \frac{4\pi\alpha\hbar}{m_0^2\omega_{\text{ph}}} \text{Im} \sum_f \frac{M_{\bar{f}i}M_{if}}{E_f - E_i - \hbar\omega_{\text{ph}}}, \quad (9.34)$$

with the fine-structure constant α and $\hbar\omega_{\text{ph}} \approx E_f - E_i$. Note that in general, $M_{\bar{f}i} \neq M_{if}^*$ for complex rotated states, and thus the numerator in Eq. (9.34) does not simplify to $|M_{\bar{f}i}|^2$.

To avoid extremely narrow peaks for certain states, we phenomenologically model an additional linewidth caused by the coupling to phonons in the crystal. In a simplified model, the phonon-induced linewidth has a power-law dependency on the principal quantum number n as [30, 70]

$$\gamma_{\text{phn}}(n) = \gamma_0^{\text{phn}} n^{-3}. \quad (9.35)$$

We estimate the parameter $\gamma_0^{\text{phn}} = 56.4 \text{ meV}$ and assign to each resonance an effective quantum number n_{eff} based on the real part of its energy as outlined in the following

Sec. 9.3.2. The resulting linewidth shifts the imaginary part of the complex energy according to $E_f \rightarrow E_f - i\gamma_{\text{phn}}/2$.

9.3.2 Phonon-induced linewidths

In order to use Eq. (9.35), we need to determine the constant γ_0^{phn} . According to Ref. [147], the FWHM of the green 2P-state at $T = 4$ K is $\gamma^{2\text{P}} = 17.7$ meV. In Ref. [146], the complex-coordinate-rotation method was used to calculate the complex energies of the odd-parity green excitons, and to determine the linewidths γ_{cont} caused by the coupling of the green excitons to the yellow continuum. Here, we update this calculation by adding the Haken potential to the Hamiltonian, and find $\gamma_{\text{cont}}^{2\text{P}} = 9.95$ meV for the green 2P state. We can thus estimate the phonon-induced linewidth of the 2P green exciton as

$$\gamma_{\text{phn}}(n = 2) = \gamma^{2\text{P}} - \gamma_{\text{cont}}^{2\text{P}} \approx 17.7 \text{ meV} - 9.95 \text{ meV} = 7.05 \text{ meV} \quad (9.36)$$

leading to

$$\gamma_0^{\text{phn}} = 8\gamma_{\text{phn}}(n = 2) = 8 \times 7.05 \text{ meV} = 56.4 \text{ meV}. \quad (9.37)$$

We associate to each resonance an effective quantum number n_{eff} as a function of the real part of the resonance energy E ,

$$n_{\text{eff}} = \sqrt{\frac{E_{\text{Ryd}}}{E_{\text{gap}} - E}} + \delta. \quad (9.38)$$

The values $E_{\text{Ryd}} = 142$ meV, $E_{\text{gap}} = 2.30292$ eV and $\delta = 0.1$ were obtained by a phenomenological fit to the odd-parity green excitons in an updated version of the calculation in Ref. [146], where we included the Haken potential. Note that these values should not be taken as the literal Rydberg energy and quantum defect, as the inclusion of the Haken potential distorts the Rydberg spectrum.

9.3.3 Dipole transitions from odd-parity yellow exciton states to even-parity green states

Experimentally, the most easily accessible yellow exciton states are the odd-parity Γ_4^- P states. As the interseries dipole transition flips the parity, the final states will be green even-parity states with S and D type envelopes. We now investigate two different scenarios. In the first, we select for the initial state the yellow P exciton transforming like the basis state z of the irreducible representation Γ_4^- [76]. In the second scenario, we investigate the yellow P exciton state transforming like the basis state y . In both cases, the photon polarization is along the z -direction. From the product of the representations

9.3. Numerically calculated interseries transition strengths

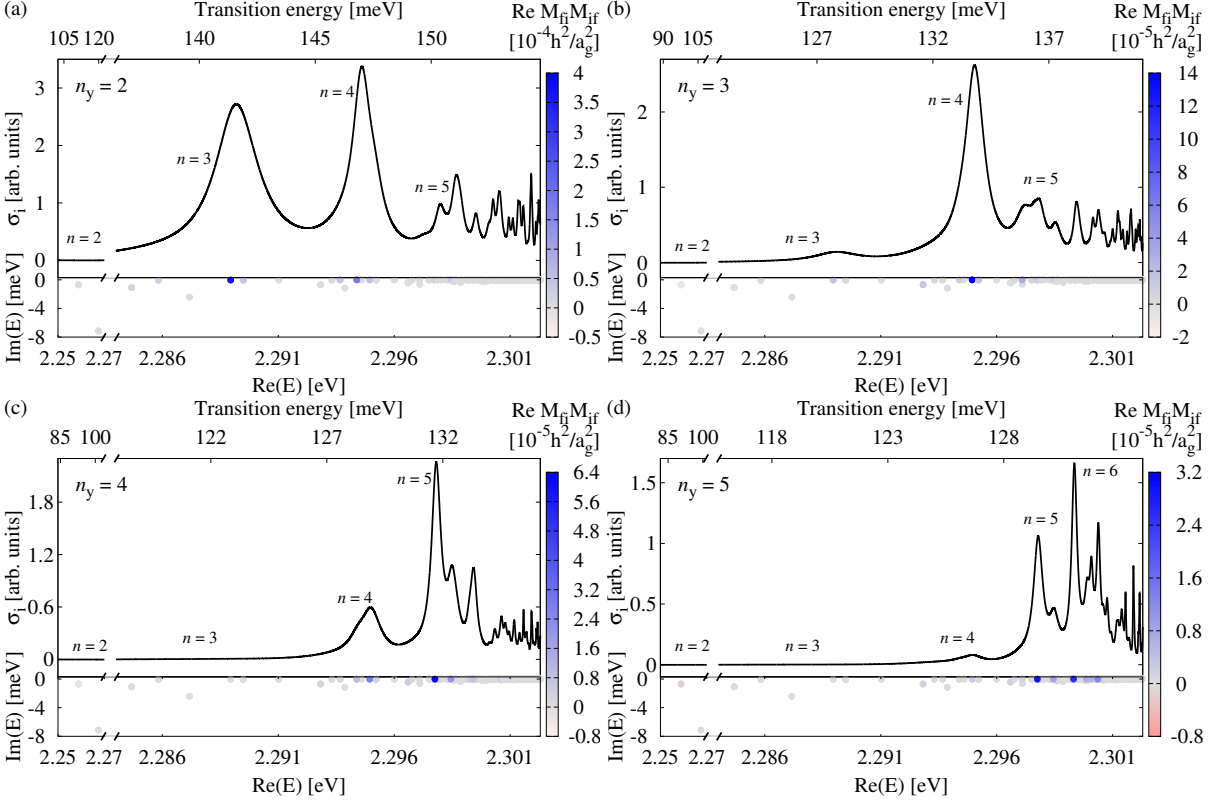


Figure 9.2.: Spectrum of transitions between odd parity yellow P excitons transforming like the function z and even parity green states. The transition is mediated by photons polarized in the z -direction. In the top part of the panels, we show the spectrum using the linewidths derived from the complex rotation corrected by Eq. (9.35) to incorporate the influence of the phonons. The uncorrected complex energy is presented in the bottom part of the panel. The color additionally shows the real part of the square $M_{fi}M_{if}$ of the interseries transition matrix element introduced in Eq. (9.1), which is proportional to the complex generalization of the oscillator strength.

$\Gamma_4^- \otimes \Gamma_4^- = \Gamma_1^+ \oplus \Gamma_3^+ \oplus \Gamma_4^+ \oplus \Gamma_5^+$ [76] we can determine which transitions to green states are allowed in principle.

We begin with the yellow P exciton and the photon both transforming according to the z -component of the Γ_4^- representation. This initial state can itself be excited using a one-photon absorption process with light polarized along the z -direction. Using the tables in Ref. [76], we can deduce that the corresponding green states transform according to Γ_1^+ and the ψ_1^{3+} -component of Γ_3^+ . In Fig. 9.2, we show interseries transition spectra in this configuration. We additionally list the results for a selection of states in Table 9.1.

Using the Rydberg energies of the yellow and green exciton series, we can estimate which green principal quantum number belongs to states with maximum overlap with a

9. Interseries dipole transitions from yellow to green excitons

yellow exciton state with given principal quantum number. In the following, we use the values $E_{\text{Ryd}}^y = 86.04 \text{ meV}$ [150] and $E_{\text{Ryd}}^g = 150.4 \text{ meV}$ [146]. The exciton Bohr radii a_0^y and a_0^g are related to the Rydberg energies by

$$\frac{a_0^g}{a_0^y} \approx \frac{E_{\text{Ryd}}^y}{E_{\text{Ryd}}^g}. \quad (9.39)$$

From a simple overlap argument, one would expect the transition strengths to be largest when initial and final state have comparable real-space extensions. As the linear extension of the excitons scales with the square of the principal quantum number n , we derive the estimate

$$n_g = \sqrt{\frac{E_{\text{Ryd}}^g}{E_{\text{Ryd}}^y}} n_y \approx 1.32 n_y, \quad (9.40)$$

to which the spectra in Figs. 9.2–9.5 fit approximately.

Table 9.1.: Real (R) and imaginary (I) parts of squared transition matrix elements $M^2 = M_{\text{if}} M_{\text{fi}}$ in units of $10^{-6} \text{ h}^2 \text{ a}_g^{-2}$ for certain selected green exciton states of energy $E = \text{Re } E_f$. The initial odd parity yellow P state of irreducible representation Γ_4^- transforms like z and the light is polarized along the z -direction.

E [eV]	2P		3P		4P		5P	
	R M^2	I M^2						
2.28468	14.69	-22.26	-1.95	1.03	-0.01	-1.90	0.25	-0.96
2.28583	22.59	-0.60	3.92	-0.12	0.66	-0.03	0.23	-0.01
2.28895	366.60	1.17	15.29	0.41	0.17	0.03	0.00	0.00
2.28949	40.96	0.99	2.17	0.15	0.02	0.01	0.00	0.00
2.29283	2.14	6.86	14.48	-10.68	2.40	-2.31	1.96	-1.02
2.29367	43.45	-0.66	1.61	-0.10	1.25	-0.05	0.47	-0.02
2.29439	181.16	0.69	8.79	0.95	9.52	0.27	0.83	0.05
2.29494	46.04	-0.51	139.46	0.42	26.58	0.50	3.05	0.15
2.29522	0.81	0.08	16.52	0.64	3.87	0.10	0.33	0.03
2.29710	9.92	-0.09	30.54	-0.14	0.02	0.02	1.31	0.06
2.29776	19.31	-0.29	12.41	-0.22	62.81	-0.05	29.01	0.28
2.29845	33.10	0.12	9.33	0.54	21.20	-0.74	8.41	0.56
2.29864	16.40	0.96	1.90	0.06	4.55	-0.42	0.18	0.13
2.29932	10.08	-0.18	6.92	-0.11	2.06	-0.08	25.78	-0.20

9.3. Numerically calculated interseries transition strengths

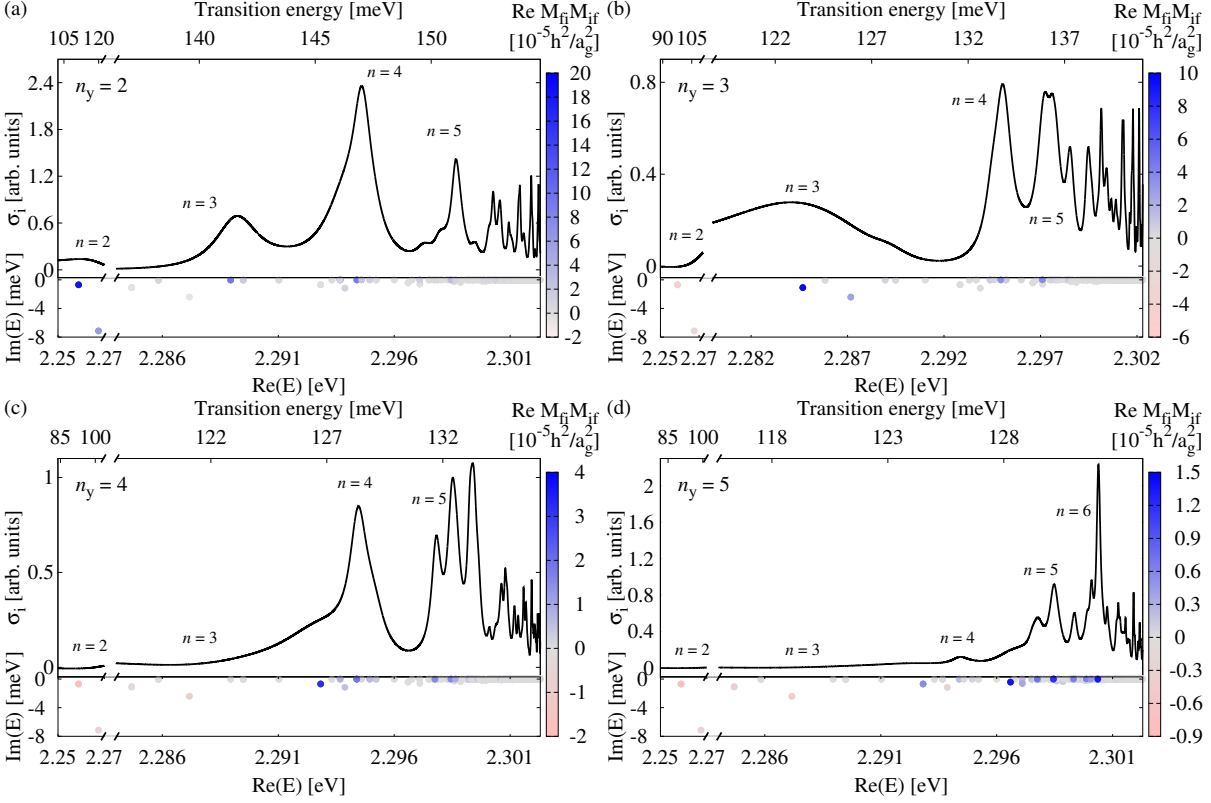


Figure 9.3.: Same as Fig. 9.2, but the initial odd parity yellow P states transform like the function y .

The resulting transition strengths are of the same order of magnitude as those found in Ref. [66]. The strongest transition in Table 9.1 is from the 2P yellow exciton to the exciton state with energy $E = 2.28895$ eV, which is a 3D state. The matrix elements become progressively weaker as the principal quantum number of the initial yellow state increases. At the same time, with increasing principal quantum number of the initial state, the green states with the highest transition strengths move to higher energies, in accordance with Eq. (9.40).

Here, as well as in the following discussions, it is also important to remember that the choice of initial state does not only influence the strength of the transition, but also the energy gap between the states. This is most evident in the configuration in Sec. 9.3.4, where the initial state is of even parity, leading to differences in the transition energies of up to 100 meV.

We now proceed to the scenario that the P exciton transforms according to the Γ_4^- function y , meaning that the initial state can be excited using a single-photon absorption process with light polarized along the y -direction. Here, the corresponding green excitons transform like the x -component of Γ_4^+ and the xz -component of Γ_5^+ [76]. In Fig. 9.3 we show a transition spectrum in this configuration. We additionally list the results for a

selection of states in Table 9.2.

The strongest transition in Table 9.2 is from the 2P yellow exciton to the exciton state with energy $E = 2.25655$ eV, which is the lowest lying 2S state. Nevertheless, it is hardly visible in our simulated spectrum in Fig. 9.3 because of its much larger width as compared to the other states.

As the principal quantum number of the initial yellow state increases, the matrix elements here also become progressively weaker. The region of green states with the strongest transition from a given yellow state does not obey Eq. (9.40) as accurately as in the previous case, lying slightly lower energetically as expected. This could be related to the different spatial extensions of the addressed green states, in addition to the generally approximate character of the overlap argument.

9.3.4 Dipole transitions from even-parity yellow states to odd-parity green states

We finally investigate transitions from yellow even-parity states to green odd-parity states. The former can be excited using two-photon absorption processes. For these transitions, we have to consider states with irreducible representations appearing in the tensor product $\Gamma_5^+ \otimes \Gamma_4^- = \Gamma_2^- \oplus \Gamma_3^- \oplus \Gamma_4^- \oplus \Gamma_5^-$. In Fig. 9.4, we show spectra for

Table 9.2.: Same as Table 9.1 but the initial odd parity yellow P states transform like y .

E [eV]	2P		3P		4P		5P	
	RM^2	IM^2	RM^2	IM^2	RM^2	IM^2	RM^2	IM^2
2.25888	183.94	286.70	-41.69	-8.86	-17.68	-13.36	-8.52	-8.79
2.26748	62.01	149.18	-24.39	-32.28	-5.90	-15.13	-2.25	-7.66
2.28468	-4.28	20.68	96.59	67.28	-2.27	13.87	-3.44	3.74
2.28717	-7.54	6.09	27.25	44.01	-9.00	1.45	-3.88	-1.10
2.28895	91.65	0.29	3.82	0.10	0.04	0.01	0.00	0.00
2.29283	-0.88	4.85	0.58	2.66	32.26	15.41	5.61	7.68
2.29367	116.27	0.92	1.11	-0.05	8.16	-0.20	1.67	-0.03
2.29439	9.88	-0.46	2.44	-0.02	18.64	-1.08	2.40	0.03
2.29439	89.79	2.81	7.50	0.55	19.35	-1.42	2.23	0.04
2.29494	11.51	-0.13	34.86	0.11	6.64	0.12	0.76	0.04
2.29660	-1.69	0.06	-0.61	0.09	0.00	0.02	13.84	-0.29
2.29710	13.48	0.29	38.10	0.36	0.24	0.01	2.25	0.16
2.29776	4.83	-0.07	3.10	-0.06	15.70	-0.01	7.25	0.07
2.29845	11.57	0.83	3.75	0.30	5.00	-0.08	9.90	0.73
2.29845	28.57	1.01	8.52	0.62	15.28	-0.50	11.81	0.46
2.30037	8.13	0.24	2.82	0.30	0.19	-0.13	13.42	-1.77

9.3. Numerically calculated interseries transition strengths

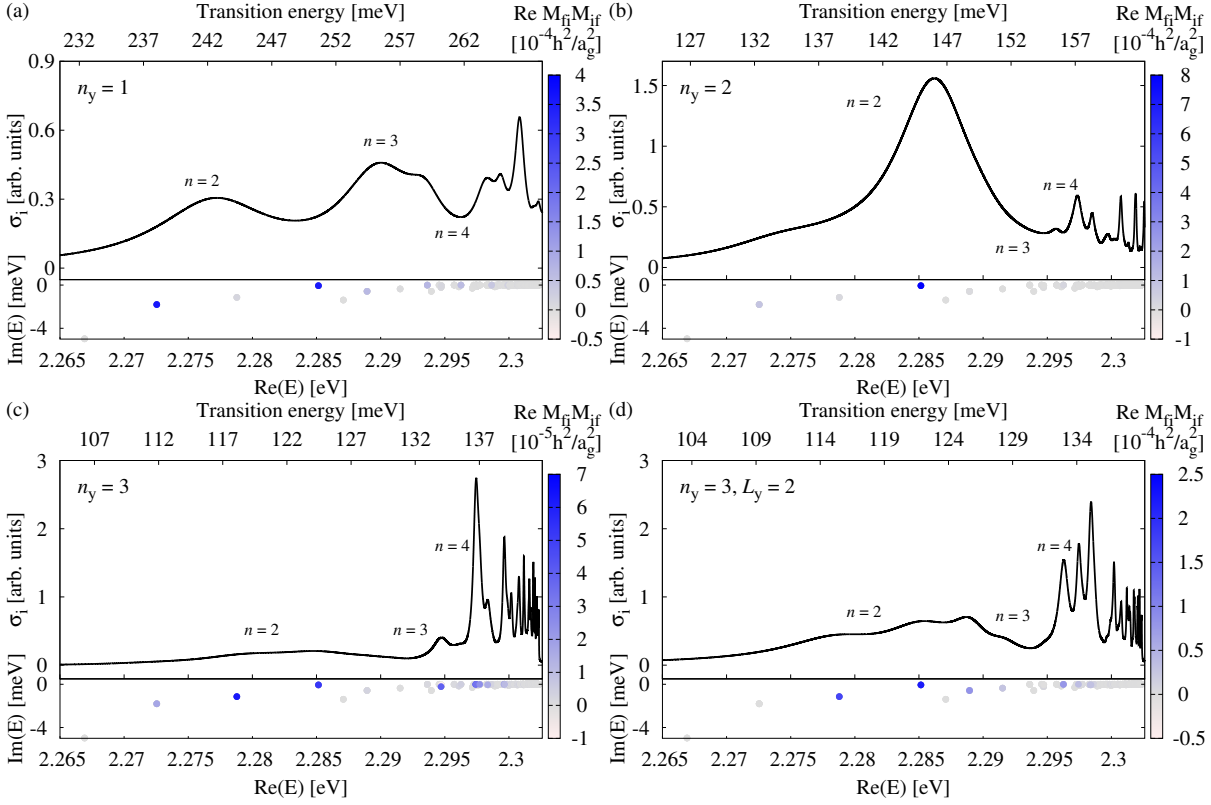


Figure 9.4.: Same as Fig. 9.2, but the initial even parity states are S ((a)-(c)) and D (d) states transforming like the function xy of the irreducible representation Γ_5^+ .

Table 9.3.: Same as Table 9.1 but the initial even parity yellow states transforms like xy of the irreducible representation Γ_5^+ . We present data for S states, but also for the yellow 3D exciton. In the last two columns we show the transition matrix elements for the initial *green* 1S exciton state.

E [eV]	1S		2S		3S		3D		1S _g	
	RM^2	IM^2	RM^2	IM^2	RM^2	IM^2	RM^2	IM^2	RM^2	IM^2
2.27254	357.68	27.39	91.35	-29.30	17.42	-1.10	0.05	-0.17	264.05	-39.87
2.27879	14.30	4.06	18.45	21.22	62.18	-30.71	171.62	55.63	-27.61	3.08
2.28515	353.85	-22.99	792.55	44.69	52.67	-0.53	219.46	3.91	329.77	27.61
2.28894	64.85	5.36	9.69	4.51	3.15	0.46	83.43	7.20	92.01	-15.48
2.29364	70.54	-3.20	1.52	0.29	1.91	-0.02	0.03	0.02	311.81	7.36
2.29626	60.26	-3.53	29.26	1.19	4.75	-0.22	79.93	0.78	80.30	2.60

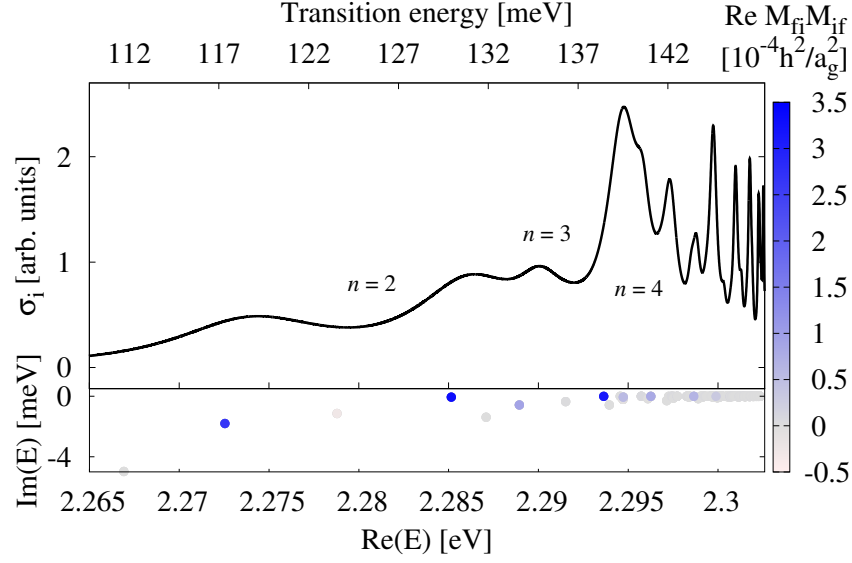


Figure 9.5.: Same as Fig. 9.4, but for the initial even parity green 1S Γ_5^+ exciton state transforming as xy .

transitions of this kind. As initial states, we chose excitons transforming according to the xy -component of the irreducible representation Γ_5^+ . In Table 9.3 we list the results for a selection of states. In Fig. 9.5, we additionally show the special case of the transitions where the initial state is the *green* 1S state, which is energetically placed among the yellow excitons.

The strongest transition in Table 9.3 is from the 2S yellow exciton to the green 2P exciton state with energy $E = 2.28515$ eV. This is also the strongest transition we found among all configurations. This has to be balanced against the fact that the initial state is of even parity, which makes it inaccessible in one-photon transitions; it can, however, be excited using two-photon absorption.

We also investigated transitions from the 3D state, see panel (d) in Fig. 9.4. These seem to be substantially stronger than the transitions from the 3S states, but still weaker than those from the 1S and 2S excitons. Finally, there are several strong transitions starting from the green 1S exciton, but they are weaker than those from yellow 1S and 2S states.

10 | Conclusion

After the experimental observation of excitons with principal quantum numbers up to $n = 25$ [30], the yellow series in cuprous oxide has been the subject of renewed scientific interest, with many proposals aiming to exploit the special properties of highly-excited Rydberg systems for a number of novel applications, such as usage in quantum information processing. For successful implementation of these ideas in excitonic Rydberg systems, a sound theoretical understanding of the exciton and its properties is required as a basis. This thesis seeks to contribute to this understanding. To that end, we analytically and numerically investigated the yellow and green exciton series in cuprous oxide.

Experimental investigations into the paraexciton series of yellow excitons in Cu_2O and corresponding exchange splittings reveal a number of ways in which a simple hydrogenlike model is insufficient. In Chapter 3, we numerically investigated spectra with modified material parameters and thus gained experimentally inaccessible insights. We used this to interpret the experimental findings in Ref. [63] and identified their roots in the properties of the system. We first investigated the reversal of the yellow 2S para- and orthoexcitons. Farenbruch *et al.* [63] identified the mixture with the 1S green orthoexciton as the origin of the reversal. We were able to corroborate this explanation with detailed calculations. We show that the orthoexciton is lifted above the paraexciton if the influence of the green excitons is removed in the simulation. Varying the spin-orbit coupling reveals an avoided crossing between the yellow 2S orthoexciton and the green 1S exciton which explains the placement of the orthoexciton below the paraexciton. We were thus able to show how the coupling of the yellow and green series leads to a behavior that qualitatively differs from the hydrogenlike approximation, underscoring its importance for the understanding of the yellow exciton series. Removing the influence of the green states, the expected order of states is restored. In this case, does the exchange splitting decrease with the third power of the principal quantum number n ? Our calculations show that this is not exactly the case. We identify two reasons for this. First of all, the Haken potential changes the dielectric constant for small radii, which

influences the wave function at the origin and therefore the splitting. A simplified treatment of the exchange splitting also overlooks the second factor, which is the coupling between S states of different principal quantum number by the exchange splitting itself. A systematic analysis shows that these two factors account for the discrepancy from the n^{-3} behavior. We conclude by studying the origin of the large difference between the exchange splittings of the yellow and green 1S states. Farenbruch *et al.* [63] confirmed the prediction by Schweiner *et al.* [38] that the splitting of the green 1S exciton is over 30 meV and therefore about two and a half times the splitting of about 12 meV for the yellow 1S state. We also identified two reasons to account for this. The first is the difference in the matrix elements of $\mathbf{S}_e \cdot \mathbf{S}_h \delta(\mathbf{r})$ for $J = 1/2$ and $J = 3/2$. Since the exchange splitting depends upon the relative orientation of the electron and hole spins, different values of the effective hole spin $\mathbf{J} = \mathbf{I} + \mathbf{S}_h$ lead to different strengths of the exchange splitting. The second is the difference in the reduced masses between the yellow and green 1S states. The reduced mass of the green 1S state is significantly higher than the reduced mass of the yellow 1S state as revealed by a detailed analysis of the Rydberg energy when correcting for the influence of short distance terms in the Hamiltonian. This leads to a higher value of the wave function at the origin and a corresponding increase of the exchange splitting.

In Chapter 4 we investigated how the band structure and especially the coupling between the yellow and green series leads to a lifting of the ordering of states according to increasing L in the case of the D state with angular momentum $F = 5/2$. The underlying mechanism is the level repulsion from the green 1S exciton state, which as our analysis shows, is strongest for yellow excitons with $L = 2$ and $F = 5/2$. This explains why the $D_{5/2}$ line, and especially the associated ortho exciton is shifted to higher energies. We show, using experimental data and numerical calculations, that it becomes the highest state in the $n = 3$, $n = 4$, and also the $n = 6$ multiplet. We present the n^{-3} scaling behavior of the energy split-off, which allows us to extrapolate to higher n and formulate the expectation that the ortho $D_{5/2}$ exciton is the highest state even in the high n regime. Our investigation can be useful for the better understanding and interpretation of impurity-dominated spectra, in particular close to the band gap, see recent studies by Krüger *et al.* [157] and Heckötter *et al.* [158]. The precise comprehension of the D exciton fine structure and the improved assignment of approximate quantum numbers is relevant for plasmon scattering rates between excitons of different angular momenta [159] and intraband transitions driven by microwaves [160].

In Chapter 5 we extended the previous work by Schweiner *et al.* [65] on the optical spectra of magnetoexcitons in cuprous oxide to the Voigt configuration and showed that the nonvanishing exciton momentum perpendicular to the magnetic field leads to the appearance of an effective magneto-Stark field. Including the valance band structure and taking into account central-cell corrections as well as the Haken potential allowed us to produce numerical results in good agreement with experimental absorption spectra. We observe a significant increase in the number of visible lines in both the experimental as well as our numerical data as compared to the Faraday configuration. Using group

theoretical methods, we show that this is related to the magneto-Stark field increasing the mixing between states. While their positions remain relatively unaffected, the mixing of states leads to finite oscillator strength of, at least in principle, all lines.

We extended the method developed by Schweiner *et al.* [35, 38, 65] for the calculation of absorption spectra of excitons in Cu_2O to the simulation of Second Harmonic Generation intensities in Chapter 6. In Cu_2O , SHG is forbidden along axes with a C_2 symmetry. The application of an external magnetic field makes SHG along those directions allowed. We mainly consider the case of SHG along forbidden axes. We identify two separate mechanisms by which a magnetic field can induce a SHG signal. First of all, the magnetic field itself reduces the symmetry and mixes the exciton states in an appropriate way to produce a nonvanishing SHG intensity. In this case, parity remains a good quantum number and the emitted photon can only be produced by a quadrupole process. In the Voigt configuration, the magnetic field induces an additional effective electric field. This breaks the inversion symmetry and also makes SHG with dipole emission processes possible. We study spectra where both quadrupole and dipole emission processes play a role. To this end, we estimate the relative strength of these processes by comparing suitable numerical and experimental spectra. We compare numerically calculated and experimental data for various choices of polarizations of the incoming and outgoing light, direction of the wave vector, and direction of the magnetic field. We find that for certain configurations, spectra are to leading order entirely induced by the magnetic or by the electric field. Good agreement between experiment and theory is observed for the most part, some weaknesses of the numerical method remain. First of all, the treatment of SHG in allowed directions requires a more careful approach towards the center-of-mass motion, since in this case, the nonvanishing \mathbf{K} vector by itself induces a SHG signal. To include this properly, the Hamiltonian has to be complemented by additional \mathbf{K} -dependent terms. The SHG intensities associated with specific exciton lines is dependent on their linewidths. The inclusion of this effect in our model is only rudimentary. A better treatment is difficult, since it would require the detailed knowledge of the lifetimes of the exciton states even in the regime of strong mixing. An additional weakness of the numerical method used here are the central-cell corrections. Due to their inaccuracy, the positions of the even exciton states are slightly too high energetically. This leads to a too strong mixing of the S and P states and thus to too strong intensities of these lines. An improved treatment of the central-cell corrections could solve this problem. In Ref. [138] it was shown that SHG is sensitive to strain down to levels of ppm. Therefore, also strain may influence the appearance of the spectra. Still, for the main application considered in this work, that is, for the investigation of magnetic-field induced SHG spectra in forbidden directions, we achieve satisfactory results. Improved treatments of the central-cell corrections and center-of-mass motion in allowed configurations are necessary in future work.

Starting from the numerical method for the calculation of yellow excitons in cuprous oxide developed by Schweiner *et al.* [35, 65], in Chapter 7 we calculated complex exciton resonances in electric and parallel electric and magnetic fields using the complex-

coordinate-rotation method. From the complex energies, we could determine the decay rates and simulate absorption spectra from circularly polarized light. In the case of the numerical calculation of magnetoexcitons, detailed comparisons with experimental data revealed excellent agreement [65]. A similar comparison including the electric field would thus be an interesting future task. Our calculations also open up the possibility of studying exceptional points in exciton spectra, which can only appear in non-Hermitian systems like the one investigated in this chapter. In contrast to the hydrogen atom, exceptional points in the spectra of excitons in cuprous oxide are expected to appear already at experimentally accessible field strengths [145], making the system an excellent candidate for the experimental observation of exceptional points in a Rydberg system. Nikitine [51] has investigated experimentally the green exciton series in Cu_2O and, recently, Krüger and Scheel [66] have focused on the interseries transitions, e.g., between yellow and green excitons. In this context, a better understanding of the green exciton series is desirable. Since the green series is located inside of the yellow continuum [147, 148, 151], and the different series couple, the green exciton states are actually resonances. The complex-coordinate-rotation method used in Chapter 7 thus is also an appropriate tool for the investigation of these resonance states.

In Chapter 8, we have computed the resonance positions, linewidths, and relative oscillator strengths of the green exciton series of cuprous oxide, thereby taking into account the valence band structure of the crystal and the coupling of the green excitons to the yellow continuum. For the computations we have used a complete basis set with Coulomb-Sturmian functions for the radial part of the wave function and the complex-coordinate-rotation method. For the dominant P states in the absorption spectrum we have confirmed their hydrogenlike behavior and extracted the Rydberg energy and quantum defect, which are in good agreement with literature [150]. The linewidths of the green P states decrease $\sim n^{-3}$ with increasing principal quantum number. In Sec. 8.2 we have compared some resonance positions to the experimental work of Gross [9]. In the meantime experimental techniques have made substantial progress. A comparison with new data would thus be desirable. The interesting question is whether giant Rydberg states of the green exciton series with quantum numbers up to $n \approx 25$ and the computed fine structure splitting can be experimentally observed similar as for the yellow series [30, 33]. We first focused on the odd states. The 1S state of the even green series is bound and has been computed, including the central-cell corrections, in Ref. [38]. We then additionally calculated and discussed the green even-parity exciton series. Interseries transitions are currently investigated [66]. Starting from the present studies, we then went on to calculate the interseries transition amplitudes between the yellow and green series in the next chapter, taking the valence band structure into account.

In Chapter 9, we have investigated interseries transitions between the yellow and green exciton series in the dipole approximation. We extended the calculations for the yellow-to-green interseries transitions performed in Ref. [66] by including the complex valence band structure. To properly take into account the associated coupling between the green exciton states and the yellow continuum, we used the complex-coordinate-

rotation method for the calculation of the green exciton resonances as described in Ref. [146]. We considered different choices for the initial state in the spectral range of the yellow series, concentrating mostly on the odd-parity P states, which are most easily accessible in one-photon absorption experiments. We distinguished the cases where the photon that excites the initial exciton is polarized parallel to the photon affecting the interseries transition from the scenario in which they are orthogonally polarized. Additionally, we also calculated the probabilities for the transition from the even-parity yellow states to the odd-parity green states, with the special case where the initial state is the *green* 1S exciton. The transition strengths are on the same order of magnitude in the different configurations, with those starting at an odd-parity yellow exciton being somewhat weaker than those starting at an even-parity yellow exciton. Of course, the experimental preparation of the latter is more difficult, as a two-photon excitation is required. In all cases, increasing the principal quantum number of the initial state shifts the range of excited green states to higher energies, with an overall weakening of the transition strengths in most cases. In this work, we use the dipole approximation, which is valid if the wavelength of the light affecting the interseries transition is much larger than the extension of the involved excitons. As shown in Ref. [66], this condition breaks down for transitions between the yellow and green series starting at $n \gtrsim 15$ for counter-propagating pump and probe beams. Extending our investigations to this parameter range thus requires going beyond the dipole approximation. Furthermore, an extension of our method to cover transitions between states of the yellow and blue series is relatively straightforward, but requires the implementation of the conduction band Hamiltonian including the Γ_8^- band. Another possible route is to investigate the influence of an additional external field to fine tune the properties of the transitions. Finally, one of the aims of our study was to provide theoretical predictions which can help guide experimental investigations into the interseries transitions. While there has been some experimental work with respect to intraseries transitions within the yellow series [161, 162] and with respect to interseries transitions between the yellow and blue series [163], to the best of our knowledge, there have been no experimental studies into the yellow-to-green interseries transitions investigated in this chapter yet. A comparison of our results with future experimental data is thus highly desirable.

A

Material constants

In Table A.1 we list the material parameters of cuprous oxide.

Table A.1.: Material parameters of Cu_2O used in the calculations.

Energy gap	$E_g = 2.17208 \text{ eV}$	[30]
Spin-orbit coupling	$\Delta = 0.131 \text{ eV}$	[34]
Effective electron mass	$m_e = 0.99m_0$	[164]
Effective hole mass	$m_h = 0.58m_0$	[164]
Valence band parameters	$\gamma_1 = 1.76$	[34]
	$\gamma_2 = 0.7532$	[34]
	$\gamma_3 = -0.3668$	[34]
	$\eta_1 = -0.020$	[34]
	$\eta_2 = -0.0037$	[34]
	$\eta_3 = -0.0337$	[34]
Exchange interaction	$J_0 = 0.792 \text{ eV}$	[38]
Short distance correction	$V_0 = 0.539 \text{ eV}$	[38]
Lattice constant	$a_g = 0.42696 \text{ nm}$	[68]
Dielectric constants	$\varepsilon_{s1} = 7.5$	[125]
	$\varepsilon_{b1} = \varepsilon_{s2} = 7.11$	[125]
	$\varepsilon_{b2} = 6.46$	[125]
Energy of Γ_4^- -LO phonons	$\hbar\omega_{\text{LO1}} = 18.7 \text{ meV}$	[80]
	$\hbar\omega_{\text{LO2}} = 87 \text{ meV}$	[80]

B

Assignment of quantum numbers for the green series

In this appendix, we present additional numerical data for the green exciton series, including an assignment of approximate quantum numbers, group theoretical representations and degeneracies of states. The assignment of approximate quantum numbers is a nontrivial task, due to the strong overlap of n and L manifolds. To this end, starting with the hydrogenlike exciton model, we slowly switch on the band structure and follow the resonance positions. We also apply projection operators to the eigenstates $|\psi\rangle$ to help with the assignment of quantum numbers.

The Hamiltonian describing odd-parity excitons in cuprous oxide in relative coordinates can be separated into the form (see Refs. [35, 86])

$$H = E_g + H_0 + H_{\text{SO}} + \lambda H_{\text{vb}}, \quad (\text{B.1})$$

with the hydrogenlike part

$$H_0 = \frac{\gamma'_1 \mathbf{p}^2}{2m_0} - \frac{e^2}{4\pi\epsilon_0\epsilon|\mathbf{r}|}, \quad (\text{B.2})$$

using $\gamma'_1 = \gamma_1 + m_0/m_e$, the spin-orbit coupling term

$$H_{\text{SO}} = \frac{2}{3}\Delta \left(1 + \frac{1}{\hbar^2} \mathbf{I} \cdot \mathbf{S}_h \right), \quad (\text{B.3})$$

and additional terms stemming from the complex valence band structure H_{vb} ,

$$H_{\text{vb}} = \frac{1}{2\hbar^2 m_0} \{ 4\hbar^2 \gamma_2 \mathbf{p}^2 + 2(\eta_1 + 2\eta_2) \mathbf{p}^2 (\mathbf{I} \cdot \mathbf{S}_h) - 6\gamma_2 (p_1^2 \mathbf{I}_1^2 + \text{c.p.}) - 12\eta_2 (p_1^2 \mathbf{I}_1 \mathbf{S}_{h1} + \text{c.p.}) \\ - 12\gamma_3 (\{p_1, p_2\} \{ \mathbf{I}_1, \mathbf{I}_2 \} + \text{c.p.}) - 12\eta_3 (\{p_1, p_2\} (\mathbf{I}_1 \mathbf{S}_{h2} + \mathbf{I}_2 \mathbf{S}_{h1}) + \text{c.p.}) \}.$$

B. Assignment of quantum numbers for the green series

To make the assignment of states possible, we introduce the parameter λ in Eq. (B.1) controlling the strength of the band structure. For $\lambda = 0$, the excitons are described in the hydrogen-like model and with $\lambda = 1$ the full band structure is switched on. We now diagonalize the Hamiltonian, while varying λ between zero and one. Following the resonance states in the resulting E - λ -diagram then allows for the assignment of the principal quantum number as shown in Figs. B.1 and B.2. Still, the assignment remains ambiguous due to the existence of various avoided crossings. We additionally calculate the P state component

$$p_{\text{P}} = |\langle L = 1 | \psi \rangle|^2 = \langle \psi | P_{L=1} | \psi \rangle \quad (\text{B.4})$$

and the F state component

$$p_{\text{F}} = |\langle L = 3 | \psi \rangle|^2 = \langle \psi | P_{L=3} | \psi \rangle \quad (\text{B.5})$$

with the corresponding projection operators $P_{L=1}$ and $P_{L=3}$, respectively.

In Table B.1 we present the numerical data for all odd parity green resonance states with energies up to $E = 2.299$ eV and dominant P states up to $n = 15$. The table includes the assignment of the approximate principal quantum number n , orbital angular momentum L , irreducible representation, degeneracy g , complex resonance energy E , and the complex relative oscillator strength f_{rel} . Furthermore, we provide the values for p_{P} and p_{F} computed according to Eqs. (B.4) and (B.5) and the yellow admixture

$$p_{\text{y}} = |\langle J = 1/2 | \psi \rangle|^2 = \langle \psi | P_{J=1/2} | \psi \rangle. \quad (\text{B.6})$$

In Table B.2 we present analogous data for the even series including the central-cell corrections, listing all even parity states of the green series up to the 6S state and determine the irreducible representation in the O_{h} group, additionally listing the admixtures of various J and L quantum numbers. To assign the principal quantum and angular quantum number we follow the states from turned off to fully turned on band structure terms, see Fig. B.2. The assignment is difficult because of various avoided crossings. Note that, similarly to the oscillator strengths, the admixtures are no longer positive real numbers.

The assignments of quantum numbers in Tables B.1 and B.2 shows that, in contrast to the yellow series, the fine structure related by the band structure terms is strong enough to cause multiplets belonging to different principal quantum numbers to overlap for the green series. This underlines the discussion in Sec. 4.3, where we used the associated matrix elements to conclude, that the cubic band structure terms affect the green excitons much more strongly than the yellow excitons.

Table B.1.: Numerical data for all odd parity green resonance states with energies up to $E = 2.299$ eV and dominant P states up to $n = 15$. Assignment of the approximate principal quantum number n , orbital angular momentum L , irreducible representation, degeneracy g , complex resonance energy E , and the complex relative oscillator strength f_{rel} . Furthermore, we provide the values for p_P and p_F computed according to Eqs. (B.4) and (B.5) and the yellow admixture p_Y according to Eq. (B.6).

State	Irrep.	g	Re E [eV]	Im E [meV]	Re f_{rel}	Im f_{rel}	p_P	p_F	p_Y
2P	Γ_6^-	4	2.26887	-3.01965	4.2998	5.8604	0.955	0.043	0.018
2P	Γ_8^-	8	2.27404	-1.19593	0.7471	1.4121	0.879	0.117	0.010
2P	Γ_7^-	4	2.27948	-0.81870	0.0000	0.0000	0.856	0.136	0.017
2P	Γ_8^-	8	2.28559	-0.04207	-0.0177	0.0146	0.857	0.141	0.004
3P	Γ_6^-	4	2.28765	-0.90691	1.1603	1.8982	0.966	0.030	0.009
3P	Γ_8^-	8	2.28944	-0.39764	0.2350	0.4813	0.895	0.099	0.004
3P	Γ_7^-	4	2.29178	-0.26468	0.0000	0.0000	0.875	0.118	0.007
3P	Γ_8^-	8	2.29384	-0.00734	-0.0052	0.0083	0.611	0.379	0.001
4P	Γ_6^-	4	2.29423	-0.38575	0.5028	0.8270	0.941	0.050	0.004
4F	Γ_6^-	4	2.29474	-0.00149	0.0039	-0.0007	0.030	0.833	0.001
4F	Γ_8^-	8	2.29486	-0.04633	-0.0475	0.0259	0.030	0.842	0.002
4P	Γ_8^-	8	2.29502	-0.13785	0.1574	0.1803	0.885	0.110	0.001
4F	Γ_8^-	8	2.29587	-0.00089	-0.0001	0.0001	0.012	0.824	0.001
4P	Γ_7^-	4	2.29625	-0.12115	0.0000	0.0000	0.769	0.222	0.003
4F	Γ_8^-	8	2.29639	-0.00593	-0.0024	0.0131	0.072	0.905	0.001
5P	Γ_6^-	4	2.29731	-0.19095	0.2571	0.4496	0.905	0.091	0.002
4F	Γ_6^-	4	2.29737	-0.00676	0.0004	-0.0169	~ 0	0.565	0.000
4P	Γ_8^-	8	2.29751	-0.00784	-0.0061	0.0080	0.461	0.476	0.001
4F	Γ_8^-	8	2.29754	-0.00193	-0.0003	0.0025	0.058	0.550	0.000
5F	Γ_6^-	4	2.29766	-0.00303	0.0092	0.0002	0.095	0.788	0.001
5P	Γ_8^-	8	2.29769	-0.08012	0.0503	0.0934	0.748	0.239	0.001
4F	Γ_7^-	4	2.29782	-0.00014	0.0000	0.0000	0.035	0.622	0.000
5F	Γ_8^-	8	2.29783	-0.01073	0.0158	0.0061	0.313	0.596	0.000
5F	Γ_8^-	8	2.29835	-0.00059	-0.0001	0.0000	0.013	0.835	0.001
4F	Γ_7^-	4	2.29841	-0.01880	0.0000	0.0000	0.035	0.896	0.001
4F	Γ_8^-	8	2.29848	-0.00070	0.0006	0.0009	0.097	0.846	0.000
5P	Γ_7^-	4	2.29851	-0.04862	0.0000	0.0000	0.791	0.175	0.001
5F	Γ_8^-	8	2.29875	-0.00545	-0.0017	0.0127	0.090	0.897	0.001
6P	Γ_6^-	4	2.29901	-0.10700	0.1337	0.2630	0.812	0.164	0.001
7P	Γ_6^-	4	2.30005	-0.06821	0.1416	0.1579	0.671	0.275	0.001
8P	Γ_6^-	4	2.30072	-0.04328	0.0519	0.1085	0.648	0.290	0.001
9P	Γ_6^-	4	2.30120	-0.03314	0.0438	0.0730	0.510	0.368	0.000
10P	Γ_6^-	4	2.30154	-0.02334	0.0302	0.0550	0.509	0.383	0.000
11P	Γ_6^-	4	2.30180	-0.01733	0.0268	0.0387	0.455	0.429	0.000
12P	Γ_6^-	4	2.30199	-0.01459	0.0198	0.0322	0.363	0.418	0.000
13P	Γ_6^-	4	2.30215	-0.01012	0.0168	0.0223	0.404	0.462	0.000
14P	Γ_6^-	4	2.30227	-0.00903	0.0118	0.0212	0.327	0.408	0.000
15P	Γ_6^-	4	2.30237	-0.00742	0.0105	0.0165	0.321	0.474	0.000

B. Assignment of quantum numbers for the green series

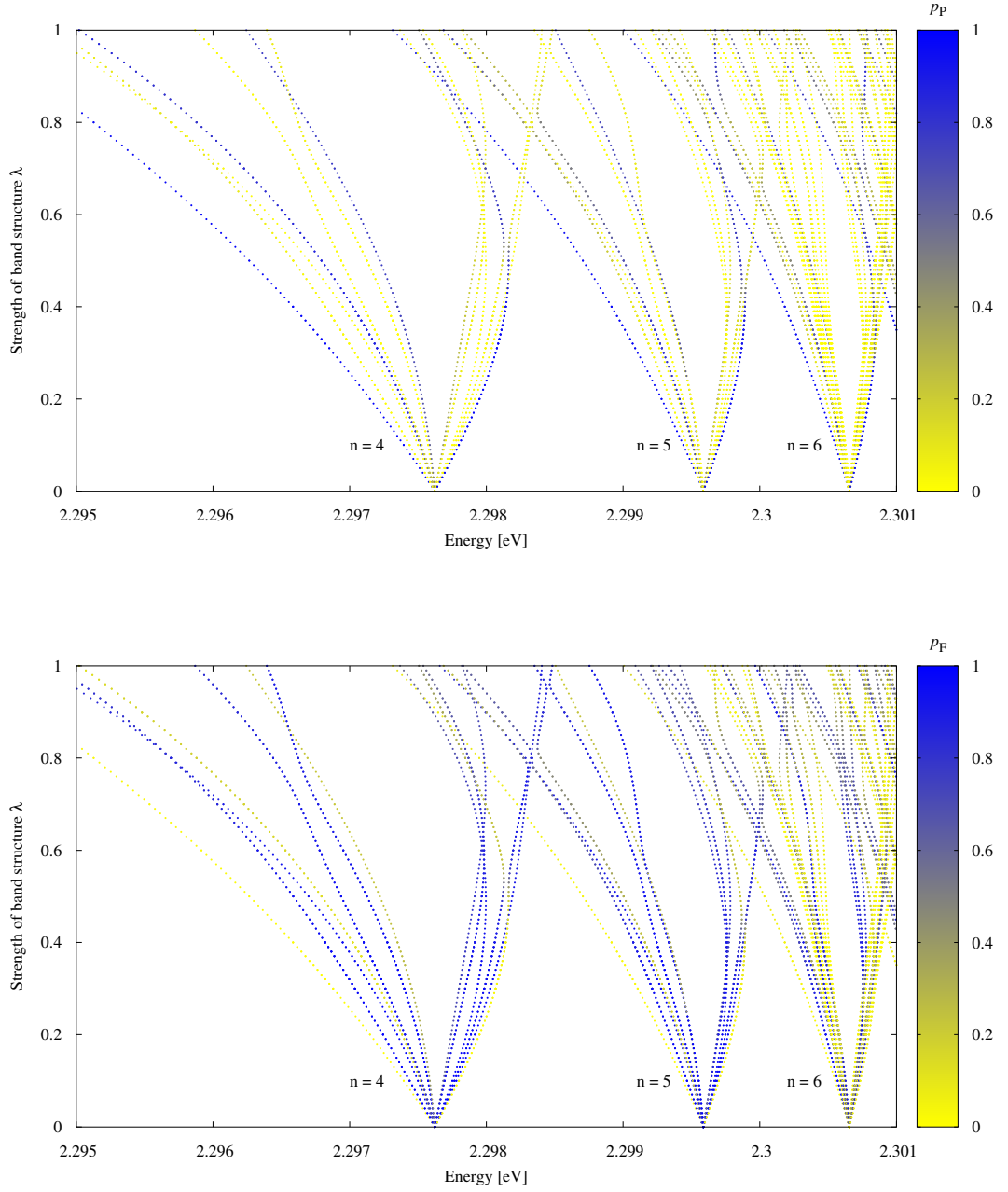


Figure B.1.: Energies of odd parity green states as a function of the strength of the band structure. A value of $\lambda = 0$ means that the band structure is completely switched off, whereas a value of $\lambda = 1$ signifies that the band structure is completely switched on. The color palette shows the P state component p_P (top) and F state component p_F (bottom) given in Eqs. (B.4) and (B.5), respectively.

Table B.2.: Numerical data for the even parity green excitons up to the 6S state. We list the energy E , degeneracy g , the admixtures of $J = 1/2$ (p_y), $J = 3/2$ (p_g), $L = 0$ (p_S), $L = 2$ (p_D) and $L = 4$ (p_G). We assign a principal and angular quantum number by following the states as the band structure changes from fully turned off to fully turned on, see Fig. B.2. For almost all states, this assignment agrees with the dominant admixture.

g	Irreps	Re E [eV]	Im E [eV]	Re p_y	Im p_y	Re p_g	Im p_g	Re p_S	Im p_S	Re p_D	Im p_D	Re p_G	Im p_G
2S	5 $\Gamma_3^+ + \Gamma_4^+$	2.2565503	-0.0055253	-0.09796	0.11345	1.09796	-0.11345	0.99265	-0.02880	0.04223	-0.05869	-0.03610	0.08601
2S	3 Γ_5^+	2.2674550	-0.0072101	-0.07434	0.07290	1.07434	-0.07290	1.00460	-0.03371	0.02083	-0.02301	-0.02586	0.05568
3S	5 $\Gamma_3^+ + \Gamma_4^+$	2.2845550	-0.0020239	-0.02134	0.01079	1.02134	-0.01079	0.83711	0.05120	0.16842	-0.05820	-0.00639	0.00653
3D	4 $\Gamma_1^+ + \Gamma_4^+$	2.2858329	-0.0000665	0.00198	-0.00117	0.99802	0.00117	0.00000	0.00000	0.95916	0.00097	0.03700	0.00002
3S	3 Γ_5^+	2.2871567	-0.0024291	-0.02634	0.02377	1.02634	-0.02377	0.82189	0.06197	0.18435	-0.07990	-0.00693	0.01721
3D	4 $\Gamma_1^+ + \Gamma_4^+$	2.2889469	-0.0000346	0.00422	-0.00049	0.99578	0.00049	0.00000	0.00000	0.90231	-0.00006	0.09503	0.00036
3D	5 $\Gamma_3^+ + \Gamma_4^+$	2.2894876	-0.0000476	0.00328	-0.00082	0.99672	0.00082	0.01039	-0.00209	0.85835	0.00196	0.12761	0.00070
3D	3 Γ_5^+	2.2894901	-0.0000471	0.00333	-0.00077	0.99667	0.00077	0.01412	-0.00384	0.85530	0.00338	0.12693	0.00102
3D	4 $\Gamma_2^+ + \Gamma_5^+$	2.2910256	-0.0000302	0.00320	-0.00053	0.99680	0.00053	0.00004	0.00000	0.83429	0.00002	0.16250	0.00033
4S	5 $\Gamma_3^+ + \Gamma_4^+$	2.2928264	-0.0009940	-0.00752	0.00237	1.00752	-0.00237	0.54893	0.06816	0.43766	-0.06625	0.01218	-0.00182
4D	4 $\Gamma_1^+ + \Gamma_4^+$	2.2933128	-0.0000369	0.00108	-0.00064	0.99892	0.00064	0.00000	0.00000	0.95631	0.00052	0.03971	0.00011
3D	5 $\Gamma_3^+ + \Gamma_4^+$	2.2936683	-0.0000027	0.00087	-0.00004	0.99913	0.00004	0.04179	-0.00130	0.65558	0.00162	0.29874	-0.00030
3D	3 Γ_5^+	2.2936683	-0.0000027	0.00087	-0.00004	0.99913	0.00004	0.04180	-0.00148	0.65556	0.00179	0.29874	-0.00029
4S	3 Γ_5^+	2.2938698	-0.0011702	-0.01327	0.01189	1.01327	-0.01189	0.53521	0.08417	0.45686	-0.09225	0.00701	0.00766
3D	5 $\Gamma_3^+ + \Gamma_4^+$	2.2943870	-0.0000079	0.00094	-0.00004	0.99906	0.00004	0.25760	-0.00283	0.69263	0.02868	0.04576	-0.00022
3D	3 Γ_5^+	2.2943889	-0.0000105	0.00103	-0.00005	0.99897	0.00005	0.26439	-0.05087	0.68544	0.05168	0.04612	-0.00066
3D	4 $\Gamma_2^+ + \Gamma_5^+$	2.2945926	-0.0000032	0.00092	-0.00004	0.99908	0.00004	0.00087	-0.00003	0.70486	-0.00006	0.29231	0.00010
4D	4 $\Gamma_1^+ + \Gamma_4^+$	2.2949444	-0.0000181	0.00223	-0.00024	0.99777	0.00024	0.00000	0.00000	0.91836	0.00011	0.07851	0.00004
4D	5 $\Gamma_3^+ + \Gamma_4^+$	2.2952197	-0.0000273	0.00186	-0.00043	0.99814	0.00043	0.03483	-0.00696	0.85141	0.00612	0.10978	0.00118
4D	3 Γ_5^+	2.2952220	-0.0000268	0.00189	-0.00037	0.99811	0.00037	0.04309	-0.00903	0.84421	0.00785	0.10872	0.00150
4D	4 $\Gamma_2^+ + \Gamma_5^+$	2.2960014	-0.0000166	0.00174	-0.00028	0.99826	0.00028	0.00002	0.00000	0.84723	0.00024	0.14880	-0.00003
5S	5 $\Gamma_3^+ + \Gamma_4^+$	2.2966105	-0.0005480	-0.00307	0.00067	1.00307	-0.00067	0.54011	0.00824	0.42295	0.00716	0.03296	-0.01350
5D	4 $\Gamma_1^+ + \Gamma_4^+$	2.2967678	-0.0000212	0.00060	-0.00036	0.99940	0.00036	0.00000	0.00000	0.94555	0.00033	0.04909	0.00006
4D	3 Γ_5^+	2.2971010	-0.0000013	0.00035	-0.00001	0.99965	0.00001	0.02587	0.00672	0.68057	-0.00465	0.28556	-0.00200
4D	5 $\Gamma_3^+ + \Gamma_4^+$	2.2971012	-0.0000010	0.00034	-0.00001	0.99966	0.00001	0.02393	0.00405	0.68199	-0.00279	0.28606	-0.00120
5S	3 Γ_5^+	2.2971032	-0.0006206	-0.00703	0.00633	1.00703	-0.00633	0.55164	0.00667	0.41295	0.01536	0.03159	-0.01919
4D	4 $\Gamma_2^+ + \Gamma_5^+$	2.2974907	-0.0000005	0.00023	-0.00001	0.99977	0.00001	0.00012	0.00000	0.20836	0.00163	0.69848	-0.00129
5G	5 $\Gamma_3^+ + \Gamma_4^+$	2.2975237	-0.0000014	0.00028	0.00000	0.99972	0.00000	0.06692	-0.01114	0.05181	0.00244	0.74714	0.00751
5G	3 Γ_5^+	2.2975242	-0.0000020	0.00030	0.00001	0.99970	-0.00001	0.06987	-0.01835	0.05027	0.00321	0.74588	0.01308
5G	4 $\Gamma_2^+ + \Gamma_5^+$	2.2976842	-0.0000012	0.00045	-0.00001	0.99955	0.00001	0.00033	-0.00001	0.49797	-0.00144	0.44615	0.00113
5D	4 $\Gamma_1^+ + \Gamma_4^+$	2.2977590	-0.0000101	0.00131	-0.00012	0.99869	0.00012	0.00000	0.00000	0.90534	0.00034	0.08852	-0.00023
5D	5 $\Gamma_3^+ + \Gamma_4^+$	2.2978851	-0.0000178	0.00103	-0.00023	0.99897	0.00023	0.01053	-0.00955	0.81777	0.00908	0.15858	0.00127
5D	3 Γ_5^+	2.2978882	-0.0000179	0.00106	-0.00015	0.99894	0.00015	0.01827	-0.01447	0.81374	0.01206	0.15508	0.00301
5G	5 $\Gamma_3^+ + \Gamma_4^+$	2.2980369	-0.0000006	0.00022	-0.00001	0.99978	0.00001	0.00217	0.00111	0.05378	-0.00381	0.78691	0.00238
5G	3 Γ_5^+	2.2980369	-0.0000006	0.00022	-0.00001	0.99978	0.00001	0.00165	0.00103	0.05315	-0.00377	0.78779	0.00242
5G	4 $\Gamma_1^+ + \Gamma_4^+$	2.2982667	0.0000000	0.00021	0.00000	0.99979	0.00000	0.00000	0.00000	0.01565	-0.00015	0.79725	0.00012
5D	4 $\Gamma_2^+ + \Gamma_5^+$	2.2983496	-0.0000094	0.00099	-0.00015	0.99901	0.00015	0.00000	0.00001	0.80522	0.00090	0.18938	-0.00075
4D	5 $\Gamma_3^+ + \Gamma_4^+$	2.2984497	-0.0000049	0.00051	-0.00007	0.99949	0.00007	0.17852	0.03192	0.62609	-0.04748	0.16574	0.01405
4D	3 Γ_5^+	2.2984499	-0.0000045	0.00049	-0.00006	0.99951	0.00006	0.17716	0.02271	0.62896	-0.03418	0.16443	0.01037
6S	5 $\Gamma_3^+ + \Gamma_4^+$	2.2985926	-0.0003231	-0.00152	0.00030	1.00152	-0.00030	0.56706	0.02343	0.35907	0.04724	0.06531	-0.06493
5G	3 Γ_5^+	2.2986376	-0.0000024	0.00020	-0.00002	0.99980	0.00002	0.02689	-0.01521	0.25372	0.00619	0.69051	0.00887
5G	5 $\Gamma_3^+ + \Gamma_4^+$	2.2986385	-0.0000033	0.00023	-0.00001	0.99977	0.00001	0.03236	-0.02517	0.25036	0.00760	0.68836	0.01727
6D	4 $\Gamma_1^+ + \Gamma_4^+$	2.2986532	-0.0000130	0.00036	-0.00023	0.99964	0.00023	0.00000	0.00000	0.92978	0.00033	0.06210	0.00001
6S	3 Γ_5^+	2.2988580	-0.0003660	-0.00417	0.00390	1.00417	-0.00390	0.56238	0.06132	0.35659	0.01778	0.07233	-0.07171

B. Assignment of quantum numbers for the green series

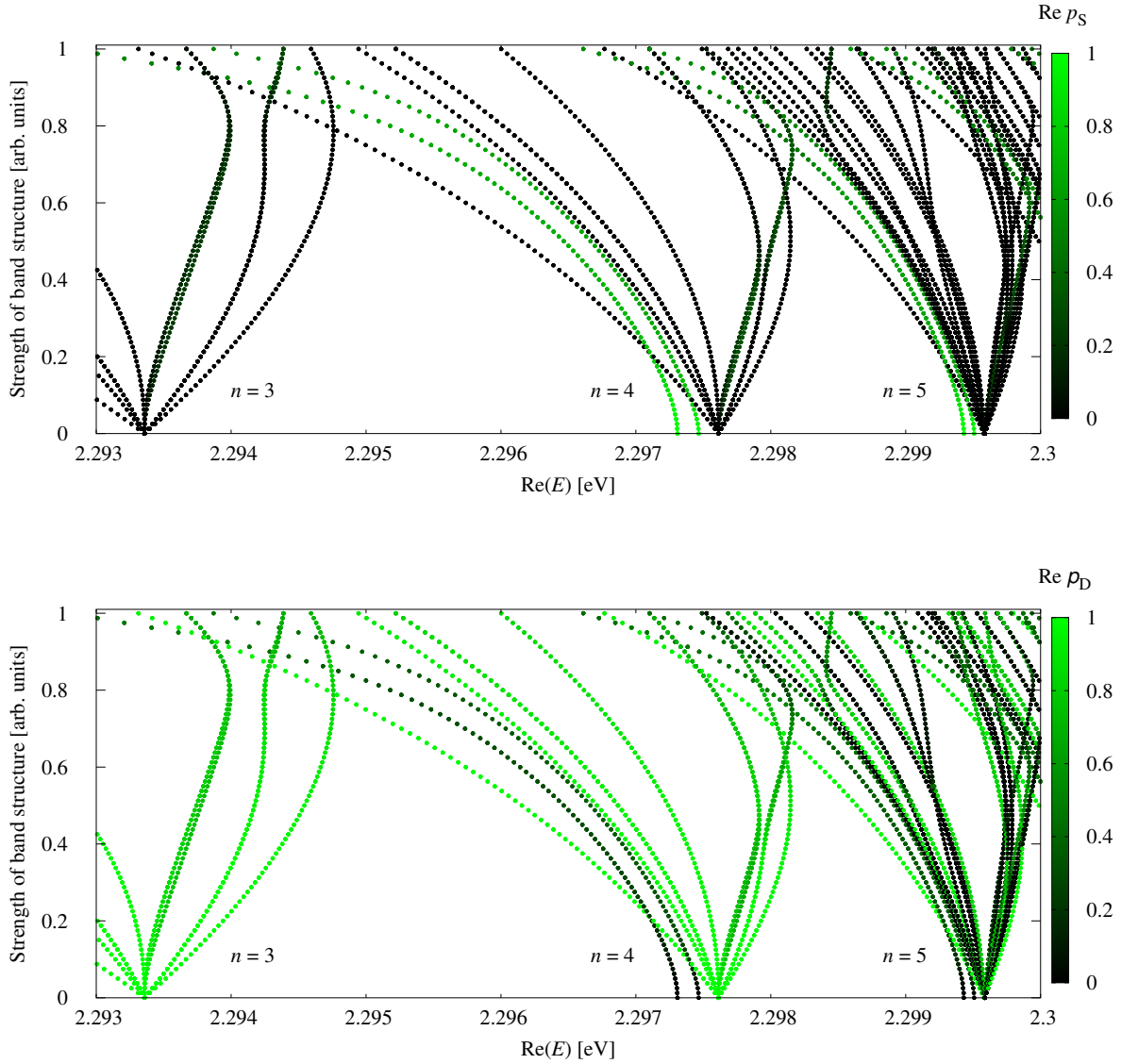


Figure B.2.: Energy positions of even parity green states as a function of the strength of the band structure, allowing for the assignment of n and L quantum numbers. The color in the top panel shows the real part of the S admixture, and in the bottom panel it shows the real part of the D admixture. The admixtures were calculated analogously to the admixtures in Fig. B.1. The strength of the band structure λ plotted on the vertical axis linearly parametrizes the band structure parameters μ' , δ' , η_1 , ν and τ analogously to Eq. (B.1), only with the additional inclusion of the central-cell corrections.



Bibliography

- [1] J. Frenkel. On the transformation of light into heat in solids. I. *Phys. Rev.* 37, 17–44 (1931).
- [2] J. Frenkel. On the transformation of light into heat in solids. II. *Phys. Rev.* 37, 1276–1294 (1931).
- [3] J. Frenkel. On the absorption of light and the trapping of electrons and positive holes in crystalline dielectrics. *Phys. Z. Sowjetunion* 9, 533 (1936).
- [4] R. Peierls. Zur Theorie der Absorptionsspektren fester Körper. *Annalen der Physik* 405, 905–952 (1932).
- [5] Gregory H. Wannier. The Structure of Electronic Excitation Levels in Insulating Crystals. *Phys. Rev.* 52, 191–197 (1937).
- [6] Masakazu Hayashi and Kiichiro Katsuki. Absorption spectrum of cuprous oxide. *Journal of the Physical Society of Japan* 5, 380B–381 (1950).
- [7] Masakazu Hayashi and Kiichirô Katsuki. Hydrogen-like absorption spectrum of cuprous oxide. *Journal of the Physical Society of Japan* 7, 599–603 (1952).
- [8] E. F. Gross and N. A. Karryev. Opticheskii spektr eksitona. *Doklady Akademii Nauk SSSR* 84, 471–474 (1952).
- [9] E. F. Gross. Optical spectrum of excitons in the crystal lattice. *Il Nuovo Cimento (1955-1965)* 3, 672–701 (1956).
- [10] N. F. Mott. Conduction in polar crystals. II. The conduction band and ultra-violet absorption of alkali-halide crystals. *Trans. Faraday Soc.* 34, 500–506 (1938).

- [11] R. S. Knox. *Theory of excitons*. Solid state physics: Supplement. Academic Press (1963).
- [12] Bernd Hönerlage, R. Levy, J. B. Grun, C. Klingshirn, and K. Bohnert. The dispersion of excitons, polaritons and biexcitons in direct-gap semiconductors. *Physics Reports* 124, 161–253 (1985).
- [13] Murray A. Lampert. Mobile and Immobile Effective-Mass-Particle Complexes in Nonmetallic Solids. *Phys. Rev. Lett.* 1, 450–453 (1958).
- [14] S. A. Moskalenko. The theory of Mott exciton in AlkaliGallium cristalls. *Optika i Spektroskopiia* 5, 147–155 (1958).
- [15] C. Klingshirn and H. Haug. Optical properties of highly excited direct gap semiconductors. *Physics Reports* 70, 315–398 (1981).
- [16] E. I. Rashba and M. D. Sturge. Excitons North-Holland. *Amsterdam* (1982).
- [17] Kin Fai Mak, Keliang He, Changgu Lee, Gwan Hyoung Lee, James Hone, Tony F. Heinz, and Jie Shan. Tightly bound trions in monolayer MoS₂. *Nature Materials* 12, 207–211 (2013).
- [18] A. G. Steele, W. G. McMullan, and M. L. W. Thewalt. Discovery of Polyexcitons. *Phys. Rev. Lett.* 59, 2899–2902 (1987).
- [19] Claus F. Klingshirn, Andreas Waag, Axel Hoffmann, and Jean Geurts. *Zinc oxide: from fundamental properties towards novel applications*. Springer Berlin, Heidelberg (2010).
- [20] A. Imamoğlu, R. J. Ram, S. Pau, and Y. Yamamoto. Nonequilibrium condensates and lasers without inversion: Exciton-polariton lasers. *Phys. Rev. A* 53, 4250–4253 (1996).
- [21] Alexey Kavokin and Guillaume Malpuech. *Cavity polaritons*, volume 32. Academic Press (2003).
- [22] Leonid V. Butov. A polariton laser. *Nature* 447, 540–541 (2007).
- [23] Christian Schneider, Arash Rahimi-Iman, Na Young Kim, Julian Fischer, Ivan G. Savenko, Matthias Amthor, Matthias Lermer, Adriana Wolf, Lukas Worschech, Vladimir D. Kulakovskii, Ivan A. Shelykh, Martin Kamp, Stephan Reitzenstein, Alfred Forchel, Yoshihisa Yamamoto, and Sven Höfling. An electrically pumped polariton laser. *Nature* 497, 348–352 (2013).
- [24] C. F. Klingshirn. *Semiconductor Optics*. Advanced texts in physics. Springer Berlin Heidelberg (2007).

-
- [25] Heinrich Stolz, Rico Schwartz, Frank Kieseling, Sunipa Som, Maria Kaupsch, Siegfried Sobkowiak, Dirk Semkat, Nobuko Naka, Thomas Koch, and Holger Fehske. Condensation of excitons in Cu_2O at ultracold temperatures: experiment and theory. *New Journal of Physics* 14, 105007 (2012).
- [26] John M. Blatt, K. W. Böer, and Werner Brandt. Bose-Einstein Condensation of Excitons. *Phys. Rev.* 126, 1691–1692 (1962).
- [27] S. A. Moskalenko. Reversible optico-hydrodynamic phenomena in a nonideal exciton gas. *Soviet Physics-Solid State* 4, 199–204 (1962).
- [28] L. V. Keldysh and A. N. Kozlov. Collective properties of excitons in semiconductors. *Sov. Phys. JETP* 27, 521 (1968).
- [29] Johannes D. Plumhof, Thilo Stöferle, Lijian Mai, Ullrich Scherf, and Rainer F. Mahrt. Room-temperature Bose–Einstein condensation of cavity exciton–polaritons in a polymer. *Nature materials* 13, 247–252 (2014).
- [30] T. Kazimierczuk, D. Fröhlich, S. Scheel, H. Stolz, and M. Bayer. Giant Rydberg excitons in the copper oxide Cu_2O . *Nature* 514, 343–347 (2014).
- [31] Marc Aßmann, Johannes Thewes, Dietmar Fröhlich, and Manfred Bayer. Quantum chaos and breaking of all anti-unitary symmetries in Rydberg excitons. *Nature Materials* 15, 741–745 (2016).
- [32] P. Grünwald, M. Aßmann, J. Heckötter, D. Fröhlich, M. Bayer, H. Stolz, and S. Scheel. Signatures of Quantum Coherences in Rydberg Excitons. *Phys. Rev. Lett.* 117, 133003 (2016).
- [33] J. Thewes, J. Heckötter, T. Kazimierczuk, M. Aßmann, D. Fröhlich, M. Bayer, M. A. Semina, and M. M. Glazov. Observation of High Angular Momentum Excitons in Cuprous Oxide. *Phys. Rev. Lett.* 115, 027402 (2015).
- [34] F. Schöne, S.-O. Krüger, P. Grünwald, H. Stolz, S. Scheel, M. Aßmann, J. Heckötter, J. Thewes, D. Fröhlich, and M. Bayer. Deviations of the exciton level spectrum in Cu_2O from the hydrogen series. *Phys. Rev. B* 93, 075203 (2016).
- [35] Frank Schweiner, Jörg Main, Matthias Feldmaier, Günter Wunner, and Christoph Uihlein. Impact of the valence band structure of Cu_2O on excitonic spectra. *Phys. Rev. B* 93, 195203 (2016).
- [36] Frank Schweiner, Jörg Main, and Günter Wunner. Magnetoexcitons Break Anti-unitary Symmetries. *Phys. Rev. Lett.* 118, 046401 (2017).
- [37] Sylwia Zielińska-Raczyńska, David Ziemkiewicz, and Gerard Czajkowski. Electro-optical properties of Rydberg excitons. *Phys. Rev. B* 94, 045205 (2016).

- [38] Frank Schweiner, Jörg Main, Günter Wunner, and Christoph Uihlein. Even exciton series in Cu_2O . *Phys. Rev. B* 95, 195201 (2017).
- [39] Florian Schöne, Heinrich Stolz, and Nobuko Naka. Phonon-assisted absorption of excitons in Cu_2O . *Phys. Rev. B* 96, 115207 (2017).
- [40] Sjard Ole Krüger and Stefan Scheel. Waveguides for Rydberg excitons in Cu_2O from strain traps. *Phys. Rev. B* 97, 205208 (2018).
- [41] Thomas F. Gallagher and Pierre Pillet. Dipole–dipole interactions of Rydberg atoms. *Advances in Atomic, Molecular, and Optical Physics* 56, 161–218 (2008).
- [42] Antoine Browaeys, Daniel Barredo, and Thierry Lahaye. Experimental investigations of dipole–dipole interactions between a few Rydberg atoms. *Journal of Physics B: Atomic, Molecular and Optical Physics* 49, 152001 (2016).
- [43] D. Jaksch, J. I. Cirac, P. Zoller, S. L. Rolston, R. Côté, and M. D. Lukin. Fast Quantum Gates for Neutral Atoms. *Phys. Rev. Lett.* 85, 2208–2211 (2000).
- [44] M. D. Lukin, M. Fleischhauer, R. Cote, L. M. Duan, D. Jaksch, J. I. Cirac, and P. Zoller. Dipole Blockade and Quantum Information Processing in Mesoscopic Atomic Ensembles. *Phys. Rev. Lett.* 87, 037901 (2001).
- [45] M. Saffman and T. G. Walker. Analysis of a quantum logic device based on dipole–dipole interactions of optically trapped Rydberg atoms. *Phys. Rev. A* 72, 022347 (2005).
- [46] M. Saffman, T. G. Walker, and K. Mølmer. Quantum information with Rydberg atoms. *Rev. Mod. Phys.* 82, 2313–2363 (2010).
- [47] Sylwia Zielińska-Raczyńska, David Ziemkiewicz, and Gerard Czajkowski. Electromagnetically induced transparency and slow light in media with Rydberg excitons. *arXiv:1612.09170* (2016).
- [48] Valentin Walther, Robert Johnes, and Thomas Pohl. Giant optical nonlinearities from Rydberg excitons in semiconductor microcavities. *Nature communications* 9, 1–6 (2018).
- [49] Sven Höfling and Alexey Kavokin. A historic experiment redesigned. *Nature* 514, 313–314 (2014).
- [50] Mohammadsadegh Khazali, Khabat Heshami, and Christoph Simon. Single-photon source based on Rydberg exciton blockade. *Journal of Physics B: Atomic, Molecular and Optical Physics* 50, 215301 (2017).

-
- [51] S. Nikitine. Experimental investigations of exciton spectra in ionic crystals. *The Philosophical Magazine: A Journal of Theoretical Experimental and Applied Physics* 4, 1–31 (1959).
- [52] S. Nikitine. Exciton spectra in semiconductors and ionic compounds. *Progress in semiconductors* 6, 269 (1962).
- [53] E. F. Gross. Spektr возбужденія экситонов в твердом теле. *Izv. Akad. Nauk. SSSR, Ser. Fiz* 20, 89 (1956).
- [54] E. F. Gross. Excitons and their motion in crystal lattices. *Soviet Physics Uspekhi* 5, 195–218 (1962).
- [55] Masayasu Ueta. Survey of Experiments on the Exciton. *Progress of Theoretical Physics Supplement* 12, 40–74 (1959).
- [56] T. P. McLean. The absorption edge spectrum of semiconductors. *Progress in semiconductors* 5, i960 (1960).
- [57] R. J. Elliott. Intensity of Optical Absorption by Excitons. *Phys. Rev.* 108, 1384–1389 (1957).
- [58] G. Dresselhaus. Effective mass approximation for excitons. *Journal of Physics and Chemistry of Solids* 1, 14–22 (1956).
- [59] V. T. Agekyan. Spectroscopic properties of semiconductor crystals with direct forbidden energy gap. *physica status solidi (a)* 43, 11–42 (1977).
- [60] Ch. Uihlein, D. Fröhlich, and R. Kenklies. Investigation of exciton fine structure in Cu_2O . *Phys. Rev. B* 23, 2731–2740 (1981).
- [61] J. M. Luttinger and W. Kohn. Motion of Electrons and Holes in Perturbed Periodic Fields. *Phys. Rev.* 97, 869–883 (1955).
- [62] K. Suzuki and J. C. Hensel. Quantum resonances in the valence bands of germanium. I. Theoretical considerations. *Phys. Rev. B* 9, 4184–4218 (1974).
- [63] A. Farenbruch, D. Fröhlich, D. R. Yakovlev, and M. Bayer. Rydberg Series of Dark Excitons in Cu_2O . *Phys. Rev. Lett.* 125, 207402 (2020).
- [64] Johannes Mund, Dietmar Fröhlich, Dmitri R. Yakovlev, and Manfred Bayer. High-resolution second harmonic generation spectroscopy with femtosecond laser pulses on excitons in Cu_2O . *Phys. Rev. B* 98, 085203 (2018).
- [65] Frank Schweiner, Jörg Main, Günter Wunner, Marcel Freitag, Julian Heckötter, Christoph Uihlein, Marc Aßmann, Dietmar Fröhlich, and Manfred Bayer. Magnetoexcitons in cuprous oxide. *Phys. Rev. B* 95, 035202 (2017).

- [66] Sjärd Ole Krüger and Stefan Scheel. Interseries transitions between Rydberg excitons in Cu_2O . *Phys. Rev. B* 100, 085201 (2019).
- [67] Julian Heckötter. *Strongly interacting Rydberg excitons in Cu_2O* . Ph.D. thesis, TU Dortmund University (2020).
- [68] H. E. Swanson and R. K. Fuyat. Standard X-ray diffraction powder patterns. *NBS Circular* 539 II, 23 (1953).
- [69] Frank Schweiner. *Theory of excitons in cuprous oxide*. Ph.D. thesis, Universität Stuttgart (2017).
- [70] Y. Toyozawa. Theory of Line-Shapes of the Exciton Absorption Bands. *Progress of Theoretical Physics* 20, 53–81 (1958).
- [71] Y. Toyozawa. Interband effect of lattice vibrations in the exciton absorption spectra. *J. Phys. Chem. Solids* Vol. 25, 59–71 (1964).
- [72] Yutaka Toyozawa. Further contribution to the theory of the line-shape of the exciton absorption band. *Progress of Theoretical Physics* 27, 89–104 (1962).
- [73] Frank Schweiner, Jörg Main, and Günter Wunner. Linewidths in excitonic absorption spectra of cuprous oxide. *Phys. Rev. B* 93, 085203 (2016).
- [74] Heinrich Stolz, Florian Schöne, and Dirk Semkat. Interaction of Rydberg excitons in cuprous oxide with phonons and photons: optical linewidth and polariton effect. *New Journal of Physics* 20, 023019 (2018).
- [75] A. R. Edmonds. *Angular Momentum in Quantum Mechanics*. Investigations in physics. Princeton University Press (1996).
- [76] G. F. Koster, J. O. Dimmock, R. G. Wheeler, and H. Statz. *Properties of the thirty-two point groups*. Massachusetts institute of technology press research monograph. M.I.T. Press, Cambridge (1963).
- [77] Holger Cartarius. Gruppentheoretische Methoden der Physik. <https://www.henrimecke.de/skripte/Gruppentheorie.pdf> (2016). Lecture notes (german).
- [78] M. French, R. Schwartz, H. Stolz, and R. Redmer. Electronic band structure of Cu_2O by spin density functional theory 21, 015502 (2008).
- [79] D. Fröhlich, R. Kenklies, Ch. Uihlein, and C. Schwab. Assignment of the Even-Parity Excitons in Cu_2O . *Phys. Rev. Lett.* 43, 1260–1263 (1979).
- [80] G. M. Kavoulakis, Yia-Chung Chang, and Gordon Baym. Fine structure of excitons in Cu_2O . *Phys. Rev. B* 55, 7593–7599 (1997).

-
- [81] H. Haken. Kopplung nichtrelativistischer teilchen mit einem quantisierten feld. *II Nuovo Cimento (1955-1965)* 3, 1230–1253 (1956).
- [82] H. Haken and W. Schottky. Die Behandlung des Exzitons nach der Vielelektronentheorie. *Zeitschrift für Physikalische Chemie* 16, 218–244 (1958).
- [83] H. Haken. Die Theorie des Exzitons im festen Körper. *Fortschritte der Physik* 6, 271–334 (1958).
- [84] J. Pollmann and H. Büttner. Effective Hamiltonians and bindings energies of Wannier excitons in polar semiconductors. *Phys. Rev. B* 16, 4480–4490 (1977).
- [85] G. M. Kavoulakis, Yia-Chung Chang, and Gordon Baym. Fine structure of excitons in Cu_2O . *Phys. Rev. B* 55, 7593–7599 (1997).
- [86] J. M. Luttinger. Quantum Theory of Cyclotron Resonance in Semiconductors: General Theory. *Phys. Rev.* 102, 1030–1041 (1956).
- [87] P. Schmelcher and L. S. Cederbaum. Regularity and chaos in the center of mass motion of the hydrogen atom in a magnetic field. *Zeitschrift für Physik D Atoms, Molecules and Clusters* 24, 311–323 (1992).
- [88] J. E. Avron, I. W. Herbst, and B. Simon. Separation of center of mass in homogeneous magnetic fields. *Annals of Physics* 114, 431 – 451 (1978).
- [89] Frank Schweiner, Jan Ertl, Jörg Main, Günter Wunner, and Christoph Uihlein. Exciton-polaritons in cuprous oxide: Theory and comparison with experiment. *Phys. Rev. B* 96, 245202 (2017).
- [90] G. Dasbach, D. Fröhlich, H. Stolz, R. Klieber, D. Suter, and M. Bayer. Wave-Vector-Dependent Exciton Exchange Interaction. *Phys. Rev. Lett.* 91, 107401 (2003).
- [91] G. Dasbach, D. Fröhlich, H. Stolz, R. Klieber, D. Suter, and M. Bayer. Anisotropic effective exciton mass in Cu_2O . *physica status solidi (c)* 2, 886–889 (2005).
- [92] G. Dasbach, D. Fröhlich, R. Klieber, D. Suter, M. Bayer, and H. Stolz. Wave-vector-dependent exchange interaction and its relevance for the effective exciton mass in Cu_2O . *Phys. Rev. B* 70, 045206 (2004).
- [93] Patrik Zielinski, Patric Rommel, Frank Schweiner, and Jörg Main. Rydberg excitons in electric and magnetic fields obtained with the complex-coordinate-rotation method. *J. Phys. B* 53, 054004 (2020).
- [94] Nimrod Moiseyev. Quantum theory of resonances: calculating energies, widths and cross-sections by complex scaling. *Physics Reports* 302, 212 – 293 (1998).

- [95] W. P. Reinhardt. Complex Coordinates in the Theory of Atomic and Molecular Structure and Dynamics. *Annual Review of Physical Chemistry* 33, 223–255 (1982).
- [96] Y. K. Ho. The method of complex coordinate rotation and its applications to atomic collision processes. *Phys. Rep.* 99, 1–68 (1983).
- [97] J. Zamastil, F. Vinette, and M. Šimánek. Calculation of atomic integrals using commutation relations. *pra* 75, 022506 (2007).
- [98] M. A. Caprio, P. Maris, and J. P. Vary. Coulomb-Sturmian basis for the nuclear many-body problem. *Phys. Rev. C* 86, 034312 (2012).
- [99] E. Anderson, Z. Bai, C. Bischof, S. Blackford, J. Demmel, J. Dongarra, J. D. Croz, A. Greenbaum, S. Hammarling, and A. McKenney. *LAPACK Users' Guide, Third edition*. Society for Industrial and Applied Mathematics, Philadelphia (1999).
- [100] R. B. Lehoucq, D. C. Sorensen, and C. Yang. *ARPACK Users' Guide*. Society for Industrial and Applied Mathematics (1998).
- [101] Patric Rommel, Jörg Main, Andreas Farenbruch, Dmitri R. Yakovlev, and Manfred Bayer. Exchange interaction in the yellow exciton series of cuprous oxide. *Phys. Rev. B* 103, 075202 (2021).
- [102] Marc Aßmann, Johannes Thewes, Dietmar Fröhlich, and Manfred Bayer. Quantum chaos and breaking of all anti-unitary symmetries in Rydberg excitons. *Nat. Mater.* 15, 741–745 (2016).
- [103] E. Poem, Y. Kodriano, C. Tradonsky, N. H. Lindner, B. D. Gerardot, P. M. Petroff, and D. Gershoni. Accessing the dark exciton with light. *Nature Physics* 6, 993 (2010).
- [104] D. Snoke and G. M. Kavoulakis. Bose–Einstein condensation of excitons in Cu_2O : progress over 30 years. *Reports on Progress in Physics* 77, 116501 (2014).
- [105] M. Beian, M. Alloing, R. Anankine, E. Cambril, C. Gomez Carbonell, A. Lemaître, and F. Dubin. Spectroscopic signatures for the dark Bose-Einstein condensation of spatially indirect excitons. *EPL (Europhysics Letters)* 119, 37004 (2017).
- [106] G. Kuwabara, M. Tanaka, and H. Fukutani. Optical absorption due to paraexciton of Cu_2O . *Solid State Communications* 21, 599 (1977).
- [107] J. Brandt, D. Fröhlich, C. Sandfort, M. Bayer, H. Stolz, and N. Naka. Ultranarrow Optical Absorption and Two-Phonon Excitation Spectroscopy of Cu_2O Paraexcitons in a High Magnetic Field. *Phys. Rev. Lett.* 99, 217403 (2007).

-
- [108] A. Mysyrowicz, D. P. Trauernicht, J. P. Wolfe, and H. R. Trebin. Stress dependence of the paraexciton in Cu_2O . *Phys. Rev. B* 27, 2562 (1983).
- [109] A. Farenbruch, J. Mund, D. Fröhlich, D. R. Yakovlev, M. Bayer, M. A. Semina, and M. M. Glazov. Magneto-Stark and Zeeman effect as origin of second harmonic generation of excitons in Cu_2O . *Phys. Rev. B* 101, 115201 (2020).
- [110] Patric Rommel, Frank Schweiner, Jörg Main, Julian Heckötter, Marcel Freitag, Dietmar Fröhlich, Kevin Lehninger, Marc Aßmann, and Manfred Bayer. Magneto-Stark effect of yellow excitons in cuprous oxide. *Phys. Rev. B* 98, 085206 (2018).
- [111] P. Rommel, J. Main, A. Farenbruch, J. Mund, D. Fröhlich, D. R. Yakovlev, M. Bayer, and Ch. Uihlein. Second harmonic generation of cuprous oxide in magnetic fields. *Phys. Rev. B* 101, 115202 (2020).
- [112] A. Farenbruch, D. Fröhlich, D. R. Yakovlev, and M. Bayer. Two-photon absorption and second harmonic generation of $1S$ para- and orthoexcitons in Cu_2O coupled by a magnetic field. *Phys. Rev. B* 102, 115203 (2020).
- [113] Julian Heckötter, Patric Rommel, Jörg Main, Marc Aßmann, and Manfred Bayer. Analysis of the Fine Structure of the D-Exciton Shell in Cuprous Oxide. *physica status solidi (RRL) – Rapid Research Letters* 15, 2100335 (2021).
- [114] E. F. Gross, B. P. Zakharchenko, and O. V. Konstantinov. *Sov. Phys. Solid State* 3, 221 (1961).
- [115] D. G. Thomas and J. J. Hopfield. A Magneto-Stark Effect and Exciton Motion in CdS . *Phys. Rev.* 124, 657–665 (1961).
- [116] H. Friedrich and D. Wintgen. The hydrogen atom in a uniform magnetic field — An example of chaos. *Phys. Rep.* 183, 37 (1989).
- [117] H. Hasegawa, M. Robnik, and G. Wunner. Classical and Quantal Chaos in the Diamagnetic Kepler Problem. *Prog. Theor. Phys. Suppl.* 98, 198 (1989).
- [118] H. Ruder, G. Wunner, H. Herold, and F. Geyer. *Atoms in strong magnetic fields: quantum mechanical treatment and applications in astrophysics and quantum chaos*. Astronomy and astrophysics library. Springer-Verlag, Berlin Heidelberg (1994).
- [119] Gregory H. Wannier. The Structure of Electronic Excitation Levels in Insulating Crystals. *Phys. Rev.* 52, 191–197 (1937).
- [120] J. Heckötter, M. Freitag, D. Fröhlich, M. Aßmann, M. Bayer, M. A. Semina, and M. M. Glazov. High-resolution study of the yellow excitons in Cu_2O subject to an electric field. *Phys. Rev. B* 95, 035210 (2017).

- [121] Gerrit E. W. Bauer and Tsuneya Ando. Exciton mixing in quantum wells. *Phys. Rev. B* 38, 6015–6030 (1988).
- [122] J. J. Hopfield and D. G. Thomas. Fine Structure and Magneto-Optic Effects in the Exciton Spectrum of Cadmium Sulfide. *Phys. Rev.* 122, 35–52 (1961).
- [123] A. G. Zhilich, John Halpern, and B. P. Zakharchenya. Magnetoabsorption Oscillations and the Zeeman Effect of Excitons for Forbidden Interband Transitions in Cu_2O Crystals. *Phys. Rev.* 188, 1294–1302 (1969).
- [124] M. Lafrentz, D. Brunne, A. V. Rodina, V. V. Pavlov, R. V. Pisarev, D. R. Yakovlev, A. Bakin, and M. Bayer. Second-harmonic generation spectroscopy of excitons in ZnO . *Phys. Rev. B* 88, 235207 (2013).
- [125] O. Madelung, U. Rössler, and M. Schulz (editors). *Landolt-Börnstein - Group III Condensed Matter*. Springer-Verlag, Berlin Heidelberg (1998).
- [126] A. Alvermann and H. Fehske. Exciton mass and exciton spectrum in the cuprous oxide. *Journal of Physics B: Atomic, Molecular and Optical Physics* 51, 044001 (2018).
- [127] A. Abragam and B. Bleaney. *Electron Paramagnetic Resonance of Transition Ions*. Oxford Classic Texts in the Physical Sciences. Oxford University Press, Oxford (2012).
- [128] Maria Göppert-Mayer. Über Elementarakte mit zwei Quantensprüngen. *Annalen der Physik* 401, 273–294 (1931).
- [129] J. J. Hopfield, J. M. Worlock, and Kwangjai Park. Two-Quantum Absorption Spectrum of KI . *Phys. Rev. Lett.* 11, 414–417 (1963).
- [130] Y. R. Shen. *The Principle of Nonlinear Optics*. Wiley-Interscience, New York (1984).
- [131] Dietmar Fröhlich. *Two- and Three-Photon Spectroscopy of Solids*, pp. 289–326. Springer US, Boston, MA (1994).
- [132] Masaharu Inoue and Yutaka Toyozawa. Two-Photon Absorption and Energy Band Structure. *Journal of the Physical Society of Japan* 20, 363–374 (1965).
- [133] I. Sängler, D. R. Yakovlev, B. Kaminski, R. V. Pisarev, V. V. Pavlov, and M. Bayer. Orbital quantization of electronic states in a magnetic field as the origin of second-harmonic generation in diamagnetic semiconductors. *Phys. Rev. B* 74, 165208 (2006).

-
- [134] I. Sanger, B. Kaminski, D. R. Yakovlev, R. V. Pisarev, M. Bayer, G. Karczewski, T. Wojtowicz, and J. Kossut. Magnetic-field-induced second-harmonic generation in the diluted magnetic semiconductors $\text{Cd}_{1-x}\text{Mn}_x\text{Te}$. *Phys. Rev. B* 74, 235217 (2006).
- [135] M. Lafrentz, D. Brunne, B. Kaminski, V. V. Pavlov, A. V. Rodina, R. V. Pisarev, D. R. Yakovlev, A. Bakin, and M. Bayer. Magneto-Stark Effect of Excitons as the Origin of Second Harmonic Generation in ZnO. *Phys. Rev. Lett.* 110, 116402 (2013).
- [136] M. Lafrentz, D. Brunne, A. V. Rodina, V. V. Pavlov, R. V. Pisarev, D. R. Yakovlev, A. Bakin, and M. Bayer. Second-harmonic generation spectroscopy of excitons in ZnO. *Phys. Rev. B* 88, 235207 (2013).
- [137] D. Brunne, M. Lafrentz, V. V. Pavlov, R. V. Pisarev, A. V. Rodina, D. R. Yakovlev, and M. Bayer. Electric field effect on optical harmonic generation at the exciton resonances in GaAs. *Phys. Rev. B* 92, 085202 (2015).
- [138] Johannes Mund, Christoph Uihlein, Dietmar Fröhlich, Dmitri R. Yakovlev, and Manfred Bayer. Second harmonic generation on the yellow $1S$ exciton in Cu_2O in symmetry-forbidden geometries. *Phys. Rev. B* 99, 195204 (2019).
- [139] J. Heckötter, M. Freitag, D. Fröhlich, M. Aßmann, M. Bayer, M. A. Semina, and M. M. Glazov. Dissociation of excitons in Cu_2O by an electric field. *Phys. Rev. B* 98, 035150 (2018).
- [140] Jörg Main and Günter Wunner. Ericson fluctuations in the chaotic ionization of the hydrogen atom in crossed magnetic and electric fields. *Phys. Rev. Lett.* 69, 586–589 (1992).
- [141] J. Main and G. Wunner. Rydberg atoms in external fields as an example of open quantum systems with classical chaos. *Journal of Physics B: Atomic, Molecular and Optical Physics* 27, 2835–2848 (1994).
- [142] Holger Cartarius, Jörg Main, and Günter Wunner. Exceptional Points in Atomic Spectra. *Phys. Rev. Lett.* 99, 173003 (2007).
- [143] Holger Cartarius, Jörg Main, and Günter Wunner. Exceptional points in the spectra of atoms in external fields. *Phys. Rev. A* 79, 053408 (2009).
- [144] Thomas N. Rescigno and Vincent McKoy. Rigorous method for computing photoabsorption cross sections from a basis-set expansion. *Phys. Rev. A* 12, 522–525 (1975).

- [145] Matthias Feldmaier, Jörg Main, Frank Schweiner, Holger Cartarius, and Günter Wunner. Rydberg systems in parallel electric and magnetic fields: an improved method for finding exceptional points. *Journal of Physics B: Atomic, Molecular and Optical Physics* 49, 144002 (2016).
- [146] Patric Rommel, Patrik Zielinski, and Jörg Main. Green exciton series in cuprous oxide. *Phys. Rev. B* 101, 075208 (2020).
- [147] J. B. Grun, M. Sieskind, and S. Nikitine. Détermination de l'intensité d'oscillateur des raies de la série verte de Cu_2O aux basses températures. *J. Phys. Radium* 22, 176–178 (1961).
- [148] J. B. Grun and S. Nikitine. Étude de la forme des raies des séries jaune et verte de la cuprite. *Journal de Physique* 24, 355 (1963).
- [149] Roger G. Newton. Optical theorem and beyond. *American Journal of Physics* 44, 639–642 (1976).
- [150] Florian Schöne, Sjard-Ole Krüger, Peter Grünwald, Marc Aßmann, Julian Heckötter, Johannes Thewes, Heinrich Stolz, Dietmar Fröhlich, Manfred Bayer, and Stefan Scheel. Coupled valence band dispersions and the quantum defect of excitons in Cu_2O . *Journal of Physics B: Atomic, Molecular and Optical Physics* 49, 134003 (2016).
- [151] Claudia Malerba, Francesco Biccari, Cristy Azanza Ricardo, Mirco D'Incau, P. Scardi, and Alberto Mittiga. Absorption coefficient of bulk and thin film Cu_2O . *Solar Energy Materials and Solar Cells* 95, 2848 (2011).
- [152] Patric Rommel, Jörg Main, Sjard Ole Krüger, and Stefan Scheel. Interseries dipole transitions from yellow to green excitons in cuprous oxide. *Phys. Rev. B* 104, 085204 (2021).
- [153] R. J. Elliott. Symmetry of excitons in Cu_2O . *Phys. Rev.* 124, 340–345 (1961).
- [154] P. Grünwald, M. Aßmann, J. Heckötter, D. Fröhlich, M. Bayer, H. Stolz, and S. Scheel. Signatures of Quantum Coherences in Rydberg Excitons. *Phys. Rev. Lett.* 117, 133003 (2016).
- [155] Mohammadsadegh Khazali, Khabat Heshami, and Christoph Simon. Single-photon source based on Rydberg exciton blockade. *Journal of Physics B: Atomic, Molecular and Optical Physics* 50, 215301 (2017).
- [156] Valentin Walther, Robert Johnne, and Thomas Pohl. Giant optical nonlinearities from Rydberg excitons in semiconductor microcavities. *Nature Communications* 9, 1309 (2018).

- [157] Sjord Ole Krüger, Heinrich Stolz, and Stefan Scheel. Interaction of charged impurities and Rydberg excitons in cuprous oxide. *Phys. Rev. B* 101, 235204 (2020).
- [158] J. Heckötter, D. Janas, R. Schwartz, M. Aßmann, and M. Bayer. Experimental limitation in extending the exciton series in Cu₂O towards higher principal quantum numbers. *Phys. Rev. B* 101, 235207 (2020).
- [159] Heinrich Stolz and Dirk Semkat. Scattering of Rydberg excitons by phonon-plasmon modes. *Journal of Physics: Condensed Matter* 33, 425701 (2021).
- [160] Liam A. P. Gallagher, Joshua P. Rogers, Jon D. Pritchett, Rajan A. Mistry, Danielle Pizzey, Charles S. Adams, Matthew P. A. Jones, Peter Grünwald, Valentin Walther, Chris Hodges, Wolfgang Langbein, and Stephen A. Lynch. Microwave-optical coupling via Rydberg excitons in cuprous oxide. *Phys. Rev. Research* 4, 013031 (2022).
- [161] D. Fröhlich, A. Nöthe, and K. Reimann. Observation of the Resonant Optical Stark Effect in a Semiconductor. *Phys. Rev. Lett.* 55, 1335–1337 (1985).
- [162] M. Jörger, E. Tsitsishvili, T. Fleck, and C. Klingshirn. Infrared absorption by excitons in Cu₂O. *physica status solidi (b)* 238, 470–473 (2003).
- [163] Johannes Schmutzler, Dietmar Fröhlich, and Manfred Bayer. Signatures of coherent propagation of blue polaritons in Cu₂O. *Phys. Rev. B* 87, 245202 (2013).
- [164] J. W. Hodby, T. E. Jenkins, C. Schwab, H. Tamura, and D. Trivich. Cyclotron resonance of electrons and of holes in cuprous oxide, Cu₂O. *Journal of Physics C: Solid State Physics* 9, 1429 (1976).



Zusammenfassung in deutscher Sprache

Nach der experimentellen Beobachtung von Exzitonen mit Hauptquantenzahlen bis $n = 25$ [30], ist die gelbe Serie in Kupferoxydul das Objekt von erneutem wissenschaftlichem Interesse geworden, mit vielen Vorhaben, die darauf abzielen die besonderen Eigenschaften hochangeregter Rydbergssysteme für neuartige Anwendungen zu benutzen, zum Beispiel in der Quanteninformationsverarbeitung. Ein gründliches theoretisches Verständnis des Exzitons und seiner Eigenschaften ist Grundlage für eine erfolgreiche Verwirklichung dieser Ideen in exzitonischen Rydbergssystemen. Die vorliegende Arbeit soll dazu beitragen dieses Verständnis zu erweitern. Zu diesem Zweck untersuchten wir analytisch und numerisch die gelbe und grüne Exzitonenserie in Kupferoxydul.

Experimentelle Untersuchungen der Paraexzitonenserie der gelben Exzitonen in Cu_2O und der zugehörigen Austauschspaltungen zeigen, dass ein einfaches wasserstoffartiges Modell in vielerlei Hinsicht unzureichend ist. In Kapitel 3 haben wir Spektren mit modifizierten Materialparametern numerisch untersucht und so experimentell unzugängliche Erkenntnisse gewonnen. Wir haben dies zur Interpretation der experimentellen Befunde in Ref. [63] benutzt und identifizierten ihre Wurzeln in den Eigenschaften des Systems. Wir untersuchten zunächst die Vertauschung des gelben 2S Para- und Orthoexzitons. Farenbruch *et al.* [63] identifizierten die Mischung mit dem grünen 1S-Orthoexziton als den Ursprung der Vertauschung. Wir konnten diese Erklärung mit detaillierten Berechnungen bestätigen. Wir zeigen, dass das Orthoexziton über das Paraexziton gehoben wird, wenn der Einfluss der grünen Exzitonen in der Simulation entfernt wird. Die Variation der Spin-Orbit-Kopplung zeigt eine vermiedene Kreuzung zwischen dem gelben 2S-Orthoexziton und dem grünen 1S-Exziton, was die Platzierung des Orthoexzitons unterhalb des Paraexzitons erklärt. Wir konnten somit zeigen, wie die Kopplung der gelben und grünen Reihe zu einem Verhalten führt, das sich qualitativ von der wasserstoffartigen Näherung unterscheidet, was ihre Bedeutung für das Verständnis der gelben Exzitonenserie unterstreicht. Entfernt man den Einfluss der grünen Zustände, wird die erwartete Reihenfolge der Zustände wiederhergestellt. Nimmt in diesem Fall die Austauschspaltung mit der dritten Potenz der Hauptquantenzahl n ab? Unsere Berechnungen

zeigen, dass dies nicht exakt der Fall ist. Wir identifizieren zwei Gründe dafür. Erstens ändert das Haken-Potential die Dielektrizitätskonstante für kleine Radien, was die Wellenfunktion am Ursprung und damit die Aufspaltung beeinflusst. Bei einer vereinfachten Behandlung der Austauschspaltung wird auch der zweite Faktor übersehen, nämlich die Kopplung zwischen S-Zuständen unterschiedlicher Hauptquantenzahl durch die Austauschspaltung selbst. Eine systematische Analyse zeigt, dass diese beiden Faktoren für die Diskrepanz zum n^{-3} -Verhalten verantwortlich sind. Abschließend untersuchen wir den Ursprung des großen Unterschieds zwischen den Austauschspaltungen der gelben und grünen 1S Zustände. Farenbruch *et al.* [63] bestätigten die Vorhersage von Schweiner *et al.* [38], dass die Aufspaltung des grünen 1S-Exzitons über 30 meV liegt und damit etwa das Zweieinhalbfache der Spaltung von etwa 12 meV für den gelben 1S-Zustand ist. Wir haben auch zwei Gründe für diesen Umstand gefunden. Der erste ist der Unterschied in den Matrixelementen von $\mathbf{S}_e \cdot \mathbf{S}_h \delta(\mathbf{r})$ für $J = 1/2$ und $J = 3/2$. Da die Austauschspaltung von der relativen Orientierung der Elektronen- und Lochspins abhängt, führen unterschiedliche Werte des effektiven Lochspins $\mathbf{J} = \mathbf{I} + \mathbf{S}_h$ zu unterschiedlichen Stärken der Austauschspaltung. Der zweite Grund ist der Unterschied in den reduzierten Massen zwischen dem gelben und dem grünen 1S-Zustand. Die reduzierte Masse des grünen 1S-Zustands ist deutlich höher als die reduzierte Masse des gelben 1S-Zustands, wie eine detaillierte Analyse der Rydberg-Energie zeigt, wenn man den Einfluss der Terme, die nur bei kleinen Abständen wichtig sind herausrechnet. Dies führt zu einem höheren Wert der Wellenfunktion am Ursprung und zu einer entsprechenden Erhöhung der Austauschspaltung.

In Kapitel 4 haben wir untersucht, wie die Bandstruktur und insbesondere die Kopplung zwischen der gelben und grünen Serie im Falle des D-Zustandes mit Drehimpuls $F = 5/2$ zu einer Aufhebung der Ordnung der Zustände nach zunehmendem L führt. Der zugrundeliegende Mechanismus ist die Niveauabstoßung vom grünen 1S-Exzitonenzustand, die, wie unsere Analyse zeigt, für gelbe Exzitonen mit $L = 2$ und $F = 5/2$ am stärksten ist. Dies erklärt, warum die $D_{5/2}$ -Linie, und insbesondere das zugehörige Orthoexziton zu höheren Energien verschoben ist. Wir zeigen anhand von experimentellen Daten und numerischen Berechnungen, dass diese Linie der höchste Zustand im $n = 3$, $n = 4$ und auch im $n = 6$ Multiplett ist. Wir präsentieren das n^{-3} -Skalierungsverhalten der Energieabspaltung, das es uns erlaubt, zu höheren n zu extrapolieren und formulieren die Erwartung, dass das Ortho- $D_{5/2}$ -Exziton auch im hohen n -Regime der höchste Zustand ist. Unsere Untersuchung kann für das bessere Verständnis und die Interpretation von Fehlstellen-dominierten Spektren nützlich sein, insbesondere in der Nähe der Bandlücke, siehe die jüngsten Studien von Krüger *et al.* [157] und Heckötter *et al.* [158]. Das genaue Verständnis der D-Exzitoneneinstruktur und die verbesserte Zuordnung der approximativen Quantenzahlen ist relevant für die Plasmonenstreueraten zwischen Exzitonen mit unterschiedlichen Drehimpulsen [159] und durch Mikrowellen getriebene Intradbandübergänge [160].

In Kapitel 5 haben wir die früheren Arbeiten von Schweiner *et al.* [65] über die optischen Spektren von Magnetoexzitonen in Kupferoxid auf die Voigt-Konfiguration ausge-

weitete und zeigten, dass der nicht verschwindende Exzitonimpuls senkrecht zum Magnetfeld zum Auftreten eines effektiven Magneto-Stark Feldes führt. Unter Einbeziehung der Valanzbandstruktur und unter Berücksichtigung der Zentralzellen-Korrekturen, sowie des Haken-Potentials konnten wir numerische Ergebnisse in guter Übereinstimmung mit experimentellen Absorptionsspektren berechnen. Wir beobachten eine signifikante Zunahme der Anzahl der sichtbaren Linien im Vergleich zur Faraday-Konfiguration sowohl in den experimentellen als auch in unseren numerischen Daten. Mit gruppentheoretischen Methoden zeigen wir, dass dies damit zusammenhängt, dass das Magneto-Stark-Feld die Vermischung zwischen den Zuständen erhöht. Während ihre Positionen relativ unbeeinflusst bleiben, führt die Mischung von Zustände zu einer endlichen Oszillatorstärke, zumindest im Prinzip, aller Linien.

Wir haben die von Schweiner *et al.* entwickelte Methode zur Berechnung von Exziton-Absorptionsspektren in Cu_2O [35, 38, 65] in Kapitel 6 auf die Simulation von Intensitäten der Frequenzverdoppelung (SHG, von engl. second harmonic generation) erweitert. In Cu_2O ist SHG entlang von Achsen mit einer C_2 -Symmetrie verboten. Durch das Anlegen eines externen Magnetfeldes wird SHG entlang dieser Richtungen erlaubt. Wir betrachten hauptsächlich den Fall von SHG entlang verbotener Achsen. Wir identifizieren zwei verschiedene Mechanismen, durch die ein Magnetfeld ein SHG-Signal induzieren kann. Erstens reduziert das Magnetfeld selbst die Symmetrie und mischt die Exzitonenzustände in geeigneter Weise, um eine nicht verschwindende SHG-Intensität zu erzeugen. In diesem Fall bleibt die Parität eine gute Quantenzahl und das emittierte Photon kann nur durch einen Quadrupolprozess erzeugt werden. In der Voigt-Konfiguration induziert das Magnetfeld ein zusätzliches effektives elektrisches Feld. Dies bricht die Inversions-symmetrie und ermöglicht auch SHG mit Dipol-Emissionsprozessen. Wir untersuchen Spektren, bei denen sowohl Quadrupol- als auch Dipol-Emissionsprozesse eine Rolle spielen. Zu diesem Zweck schätzen wir die relative Stärke dieser Prozesse durch den Vergleich geeigneter numerischer und experimenteller Spektren ab. Wir vergleichen numerisch berechnete und experimentelle Daten für verschiedene Polarisierungen des ein- und ausgehenden Lichts, Richtungen des Wellenvektors und Richtungen des Magnetfeldes. Wir stellen fest, dass für bestimmte Konfigurationen die Spektren in führender Ordnung vollständig durch das Magnetfeld oder durch das elektrische Feld induziert werden. Im Großen und Ganzen ist eine gute Übereinstimmung zwischen Experiment und Theorie zu beobachten, wobei einige Schwächen der numerischen Methode bestehen bleiben. Zunächst einmal erfordert die Behandlung von SHG in erlaubten Richtungen eine umsichtiger Herangehensweise an die Bewegung des Massenschwerpunkts, da in diesem Fall der nicht verschwindende \mathbf{K} -Vektor selbst ein SHG-Signal hervorruft. Um dies richtig zu berücksichtigen, muss der Hamiltonian durch zusätzliche \mathbf{K} -abhängige Terme ergänzt werden. Die SHG-Intensitäten, die mit bestimmten Exzitonlinien verbunden sind, hängen von deren Linienbreiten ab. Die Einbeziehung dieses Effekts in unser Modell ist nur rudimentär. Eine bessere Behandlung ist schwierig, denn sie würde die detaillierte Kenntnis der Lebensdauern der Exzitonenzustände auch im Regime der starken Durchmischung erfordern. Eine weitere Schwäche der hier verwendeten numeri-

schen Methode sind die Zentralzellen-Korrekturen. Aufgrund ihrer Ungenauigkeit sind die Positionen der geraden Exziton-Zustände energetisch etwas zu hoch. Dies führt zu einer zu starken Vermischung der S- und P-Zustände und damit zu zu starken Intensitäten dieser Linien. Für die in dieser Arbeit betrachtete Hauptanwendung, d.h. für die Untersuchung von magnetfeldinduzierten SHG-Spektren in verbotenen Richtungen, erzielen wir dennoch zufriedenstellende Ergebnisse. Verbesserte Behandlungen der Zentralzellen-Korrekturen und der Bewegung des Massenschwerpunkts in erlaubten Konfigurationen sind in zukünftigen Arbeiten erforderlich.

Ausgehend von der von Schweiner *et al.* [35, 65] entwickelten numerischen Methode zur Berechnung von gelben Exzitonen in Kupferoxid, haben wir in Kapitel 7 komplexe Exzitonenresonanzen in elektrischen und parallelen elektrischen und magnetischen Feldern unter Verwendung der komplexen Koordinatenrotationsmethode berechnet. Aus den komplexen Energien konnten wir die Zerfallsraten bestimmen und die Absorptionsspektren von zirkular polarisiertem Licht simulieren. Im Falle der numerischen Berechnung von Magnetoexzitonen ergaben detaillierte Vergleiche mit experimentellen Daten eine ausgezeichnete Übereinstimmung. Ein ähnlicher Vergleich unter Einbeziehung des elektrischen Feldes wäre daher eine interessante zukünftige Aufgabe. Unsere Berechnungen eröffnen auch die Möglichkeit exzeptionelle Punkte in Exzitonenpektren zu untersuchen, die nur in nicht-hermitschen Systemen wie dem hier untersuchten auftreten können. Im Gegensatz zum Wasserstoffatom sind die exzeptionelle Punkte in den Spektren von Exzitonen in Kupferoxid bereits bei experimentell erreichbaren Feldstärken [145] zugänglich, was das System zu einem hervorragenden Kandidaten für die experimentelle Beobachtung von exzeptionellen Punkten in einem Rydberg-System macht. Nikitine [51] hat experimentell die grüne Exzitonenreihe in Cu_2O experimentell untersucht, und vor Kurzem haben Krüger und Scheel [66] Intererienübergänge, z.B. zwischen gelben und grünen Exzitonen, studiert. In diesem Zusammenhang ist ein besseres Verständnis der grünen Exzitonenreihe wünschenswert. Da sich die grüne Serie innerhalb des gelben Kontinuums befindet [147, 148, 151], und die verschiedenen Serien koppeln, sind die grünen Exziton-Zustände eigentlich Resonanzen. Die in Kapitel 7 verwendete Methode der komplexen Koordinatenrotation ist daher auch ein geeignetes Werkzeug für die Untersuchung dieser Resonanzzustände.

In Kapitel 8 haben wir die Resonanzpositionen, Linienbreiten und relativen Oszillatorstärken der grünen Exzitonenreihe von Kupferoxid berechnet. Dabei haben wir die Valenzbandstruktur des Kristalls und die Kopplung der grünen Exzitonen mit dem gelben Kontinuum berücksichtigt. Für die Berechnungen haben wir einen vollständigen Basissatz mit Coulomb-Sturmschen Funktionen für den radialen Teil der Wellenfunktion und die Methode der komplexen Koordinatenrotation verwendet. Für die dominanten P-Zustände im Absorptionsspektrum haben wir ihr wasserstoffartiges Verhalten bestätigt und die Rydberg-Energie und den Quantendefekt extrahiert, welche in guter Übereinstimmung mit Literaturwerten [150] sind. Die Linienbreiten der grünen P-Zustände verringern sich gemäß $\sim n^{-3}$ mit steigender Hauptquantenzahl. In Abschnitt 8.2 haben wir einige Resonanzpositionen mit der experimentellen Arbeit von Gross [9] verglichen. In

der Zwischenzeit haben die experimentellen Techniken erhebliche Fortschritte gemacht. Ein Vergleich mit neuen Daten wäre daher wünschenswert. Die interessante Frage ist, ob stark ausgedehnte Rydberg-Zustände der grünen Exzitonenserie mit Quantenzahlen bis zu $n \approx 25$ und die berechnete Feinstrukturaufspaltung ähnlich wie bei der gelben Serie [30, 33] experimentell beobachtet werden können. Wir haben uns zunächst auf die ungeraden Zustände konzentriert. Der 1S-Zustand der geraden grünen Serie ist gebunden und wurde einschließlich der Zentralzellen-Korrekturen in Ref. [38] berechnet. Anschließend haben wir zusätzlich die grüne Exzitonenserie mit gerader Parität berechnet und diskutiert. Intererienübergänge werden derzeit untersucht [66]. Ausgehend von den bisherigen Studien konnten wir dann im nächsten Kapitel die Übergangsamplituden zwischen der gelben und der grünen Serie berechnen, wobei die Valenzbandstruktur berücksichtigt wurde.

In Kapitel 9 haben wir die Intererienübergänge zwischen der gelben und grünen Exzitonenserie in der Dipolnäherung untersucht. Wir erweiterten die Berechnungen für die gelb-grünen Intererienübergänge, die in Ref. [66] durchgeführt wurden, durch Einbeziehung der komplexen Valenzbandstruktur. Um die damit verbundene Kopplung zwischen den grünen Exzitonenzuständen und dem gelben Kontinuum zu berücksichtigen, haben wir die komplexe Koordinatenrotationsmethode für die Berechnung der grünen Exzitonresonanzen wie in Kapitel 8 verwendet. Wir haben verschiedene Möglichkeiten für den Ausgangszustand im Spektralbereich der gelben Serie, wobei wir uns hauptsächlich auf die P-Zustände mit ungerader Parität konzentrierten, welche in Ein-Photonen-Absorptionsexperimenten am leichtesten zugänglich sind. Wir unterscheiden den Fall, in dem das Photon, das das ursprüngliche Exziton anregt, und das Photon, welches den Intererienübergang bewirkt, parallel zueinander polarisiert sind, von dem Szenario in dem die beiden orthogonal polarisiert sind. Zusätzlich haben wir auch die Übergangswahrscheinlichkeiten von den gelben Zuständen mit gerader Parität zu den ungeraden grünen Zuständen berechnet, mit dem zusätzlichen Sonderfall, dass der Anfangszustand das *grüne* 1S-Exziton ist. Die Übergangsstärken liegen in den verschiedenen Konfigurationen in der gleichen Größenordnung, wobei die Übergänge, die mit einem gelben Exziton ungerader Parität beginnen etwas schwächer sind als diejenigen, die von einem gelben Exziton mit gerader Parität ausgehen. Natürlich ist die experimentelle Präparation des gelben Exzitons mit gerader Parität schwieriger, da eine Zwei-Photonen-Anregung erforderlich ist. In allen Fällen führt die Erhöhung der Hauptquantenzahl des Ausgangszustands dazu, dass der Bereich der angeregten grünen Zustände zu höheren Energien verschoben wird, was in den meisten Fällen mit einer Abschwächung der Übergangsstärken einhergeht. Wir verwenden die Dipolnäherung, die gültig ist, wenn die Wellenlänge des Lichts, das den Intererienübergang bewirkt, viel größer ist als die Ausdehnung der beteiligten Exzitonen. Wie in Ref. [66] gezeigt, bricht diese Bedingung für Übergänge zwischen der gelben und grünen Serie ab $n \gtrsim 15$ für gegenläufige Pump- und Probe-Strahlen zusammen. Für die Ausweitung unserer Untersuchungen auf diesen Parameterbereich muss man also über die Dipolnäherung hinausgehen. Weiterhin ist eine Erweiterung unserer Methode auf Übergänge zwischen Zuständen der gelben und der blauen Reihe relativ

einfach, erfordert aber die Implementierung des Leitungsband-Hamiltonians einschließlich der Γ_8^- -Bänder. Eine weitere mögliche Route ist die Untersuchung des Einflusses eines zusätzlichen externen Feldes, mit dem Ziel die Eigenschaften der Übergänge fein abzustimmen. Eines der Ziele unserer Studie war es schließlich, theoretische Vorhersagen zu treffen, die bei der experimentellen Untersuchungen der Intererienübergänge helfen können. Es gibt zwar einige experimentelle Arbeiten zu Intraserien-Übergängen innerhalb der der gelben Serie [161, 162] und in Bezug auf Übergänge zwischen der gelben und der blauen Serie [163], aber es gibt unseres Wissens nach noch keine experimentellen Studien zu den untersuchten Übergängen von Gelb nach Grün. Ein Vergleich unserer Ergebnisse mit zukünftigen experimentellen Daten ist daher sehr wünschenswert.

Patric Sebastian Rommel

Persönliche Daten

Geburtsdatum 05.08.1994
Geburtsort Kirchheim unter Teck

Sprachen

Deutsch Muttersprache
Englisch fließend
Französisch mittlere Kenntnisse

Schulausbildung

09/00 - 07/04 **Grundschule**, Schlierbach.
09/04 - 06/12 **Raichberg Gymnasium Ebersbach**, Ebersbach an der Fils, Allgemeinbildendes Abitur.
Abschluss Abitur 2012, Note: 1.2

Studium

10/12 - 10/15 **Bachelorstudiengang Physik**, Universität Stuttgart.
Abschluss Bachelor of Science 2012, Note: 1.3
04/15 - 08/15 **Bachelorarbeit**, *SUSY-Partner des zweidimensionalen \mathcal{PT} -symmetrischen Doppelmuldenpotentials*, unter der Betreuung von Prof. Dr. Günter Wunner, 1. Institut für Theoretische Physik, Universität Stuttgart.
10/15 - 11/17 **Masterstudiengang Physik**, Universität Stuttgart.
Abschluss Master of Science 2014, Note: 1.1 mit Auszeichnung
10/16 - 10/17 **Masterarbeit**, *Modell mit Mastergleichung zur Beschreibung der Exziton-Phonon-Wechselwirkung in Kupferoxydul*, unter der Betreuung von Prof. Dr. Jörg Main, 1. Institut für Theoretische Physik, Universität Stuttgart.
12/17 - 7/22 **Promotion**, *Theory of yellow and green excitons in cuprous oxide with emphasis on correction terms and external fields*, unter der Betreuung von Prof. Dr. Jörg Main, 1. Institut für Theoretische Physik, Universität Stuttgart.

Berufliche und wissenschaftliche Tätigkeiten

- 11/14 - 02/15 **Studentische Hilfskraft**, *Experimentalphysik, Universität Stuttgart*, Betreuung Übungsgruppe zur Experimentalphysik.
- 12/17 - 7/22 **Wissenschaftlicher Mitarbeiter**, *1. Institut für Theoretische Physik, Universität Stuttgart*, Betreuung diverser Übungsgruppen zur Astrophysik. Betreuung von Bachelor- und Masterarbeiten.

Stipendien und Preise

- 2012 **Ferry Porsche Preis**, für herausragende Leistungen in den Fächern Mathematik und Physik/Technik.
- 2012 **DPG-Buchpreis**, als Anerkennung für hervorragende Leistungen im Fach Physik.
- 2012 **GDCh-Abiturientenpreis**, als Anerkennung für hervorragende Leistungen im Fach Chemie.
- 2012 **Abiturientenpreis des Lions-Club Göppingen**, für hervorragende Leistungen in den Naturwissenschaften.
- 2012 - heute **Online-Stipendium von e-fellows.net**, aufgrund hervorragender Leistungen im Abitur.
- 2014 **Vorschlag für ein Stipendium der Studienstiftung des Deutschen Volkes**, durch das Prüfungsamt der Universität Stuttgart.
- 2014 und 2015 **Teilnahme an der Ferienakademie**, für besonders begabte und interessierte Studierende.

Wissenschaftliche Präsentationen und Fachvorträge

- **GiRyd Status Workshop 2022**, *Vortrag*, Mainz, Deutschland.
- **GiRyd Status Workshop 2021**, *Vortrag*, Online.
- **4th International Workshop on Rydberg Excitons in Semiconductors**, *Vortrag*, Online.
- **GiRyd Status Workshop 2020**, *Vortrag*, Mainz, Deutschland (Online).
- **3rd International Workshop on Rydberg Excitons in Semiconductors 2019**, *Vortrag und Poster*, Durham, UK.
- **GiRyd Status Workshop 2019**, *Vortrag und Poster*, Kaiserslautern, Deutschland.
- **Spring meeting 2019 of the German Physical Society**, *Vortrag*, Regensburg, Deutschland.
- **GiRyd Status Workshop 2018**, *Poster*, Hamburg, Deutschland.
- **Spring meeting 2018 of the German Physical Society**, *Poster*, Berlin, Deutschland.
- **2nd International Workshop on Rydberg Excitons in Semiconductors 2018**, *Poster*, Aarhus, Dänemark.

- **Advanced SRitp und GiRyd School on Giant Interactions in Rydberg Systems 2018**, *Poster*, Tel Aviv, Israel.
- **GiRyd Status Workshop 2017**, *Poster*, Dresden, Deutschland.

Wissenschaftliche Veröffentlichungen

- **Analysis of the fine structure of the D-exciton shell in cuprous oxide**, J. Heckötter, P. Rommel, J. Main, M. Aßmann, M. Bayer, *Phys. Status Solidi RRL* **15**, 2100335 (2021).
- **Interseries dipole transitions from yellow to green excitons in cuprous oxide**, P. Rommel, J. Main, S. O. Krüger, S. Scheel, *Phys. Rev. B* **104**, 085204 (2021).
- **Exchange interaction in the yellow exciton series of cuprous oxide**, P. Rommel, J. Main, A. Farenbruch, D. R. Yakovlev, M. Bayer, *Phys. Rev. B* **103**, 075202 (2021).
- **Classical and semiclassical description of Rydberg excitons in cuprous oxide**, J. Ertl, P. Rommel, M. Mom, J. Main, M. Bayer, *Phys. Rev. B* **101**, 241201(R) (2020).
- **Second harmonic generation of cuprous oxide in magnetic fields**, P. Rommel, J. Main, A. Farenbruch, J. Mund, D. Fröhlich, D. R. Yakovlev, M. Bayer, Ch. Uihlein, *Phys. Rev. B* **101**, 115202 (2020).
- **Green exciton series in cuprous oxide**, P. Rommel, P. Zielinski, J. Main, *Phys. Rev. B* **101**, 075208 (2020).
- **Rydberg excitons in electric and magnetic fields obtained with the complex-coordinate-rotation method**, P. Zielinski, P. Rommel, F. Schweiner, J. Main, *J. Phys. B* **53**, 054004 (2020).
- **Magneto-Stark-effect of yellow excitons in cuprous oxide**, P. Rommel, F. Schweiner, J. Main, J. Heckötter, M. Freitag, D. Fröhlich, K. Lehninger, M. Aßmann, M. Bayer, *Phys. Rev. B* **98**, 085206 (2018).
- **Exciton-phonon interaction breaking all antiunitary symmetries in external magnetic fields**, F. Schweiner, P. Rommel, J. Main, G. Wunner, *Phys. Rev. B* **96**, 035207 (2017).



Danksagung

Ich möchte mich bei all denjenigen bedanken, die mir bei der Umsetzung dieser Doktorarbeit geholfen haben

- Mein hauptsächlicher Dank gilt Jörg Main, der mir die Möglichkeit gegeben hat, dieses Thema am ITP1 in Angriff zu nehmen und den Hauptbericht übernommen hat
- Ich bedanke mich bei Maria Daghofer für die Übernahme des Mitberichts
- Vielen Dank an Jan Ertl, für die gute Zusammenarbeit, das Bouldern, unsere Buchbesprechung und eine gute Zeit
- Vielen Dank an Sascha Böhrkircher für die tolle Zusammenarbeit während des gesamten Studiums
- Ich bedanke mich bei Frank Schweiner für die Zusammenarbeit, insbesondere am Beginn der Arbeit und das Beantworten der ein oder anderen Frage
- Bei Günter Wunner für die Zusammenarbeit bei den Astrophysik-Übungen
- Bei Monika Bund für die Unterstützung bei allen Dingen die die Verwaltung und das Organisatorische betreffen
- Bei Johannes Reiff für die viele Hilfe bei IT-Problemen
- Und bei allen anderen Mitgliedern des ITP1 für das gute Arbeitsklima und die lustigen Kaffeerunden
- Bei Christoph Uihlein für die interessanten Gespräche, die mir sehr dabei geholfen haben mein Verständnis der Exzitonen zu vertiefen
- Bei Sjord-Ole Krüger und Stefan Scheel für die gute Zusammenarbeit
- Bei Julian Heckötter, Andreas Farenbruch, Johannes Mund, Dietmar Fröhlich, Marc Aßmann, Dmitri Yakovlev und Manfred Bayer für die gute Zusammenarbeit
- Bei Pavel Belov für die gute Zusammenarbeit

Danksagung

- Bei meiner Mutter, meinem Vater, meinem Bruder und meiner gesamten Familie für die Unterstützung während des Studiums. Und Maxi, dich hab' ich auch nicht vergessen ;)

Ehrenwörtliche Erklärung

Ich erkläre, dass ich diese Dissertation, abgesehen von den ausdrücklich bezeichneten Hilfsmitteln, selbständig verfasst habe.

Stuttgart, den 6. Mai 2022

Patric Sebastian Rommel